Jet Physics at High Energy Colliders

Jet Physics at High Energy Colliders

A dissertation presented

by

Yang-Ting Chien

to

The Physics Department

in partial fulfillment of the requirements

for the degree of

Doctor of Philosophy

in the subject of

Physics

Harvard University

Cambridge, Massachusetts

May 2013

Dissertation Advisor: Professor Matthew Schwartz Yang-Ting Chien

Jet Physics at High Energy Colliders

Abstract

The future of new physics searches at the LHC will be to look for hadronic signals with jets. In order to distinguish a hadronic signal from its background, it is important to develop advanced collider physics techniques that make accurate theoretical predictions. This work centers on phenomenological and formal studies of Quantum Chromodynamics (QCD), including resummation of hadronic observables using Soft Collinear Effective Theory (SCET), calculating anomalous dimensions of multi-Wilson line operators in AdS, and improving jet physics analysis using multiple event interpretations.

Hadronic observables usually involve physics at different energy scales, and the calculations depend on large logarithms of the energy ratios. We can prove factorization theorems of observables and resum large logarithms using renormalization-group techniques. The heavy jet mass distribution for e^+e^- collisions is calculated at next-to-next-to-next-to leading logarithmic order ($\mathrm{N^3LL}$), and we measure the strong coupling constant at 0.3% accuracy. We also calculate the jet-mass distribution at partial $\mathrm{N^2LL}$ in γ + jet events at the LHC. The effect of non-global logarithms in resummation estimated, and it is significant only at the peak region.

Soft QCD interactions among jets can be described by multi-Wilson line operators, with each Wilson line pointing along one of the jet directions. The anomalous dimensions of these operators are key for higher-order resummation. We study these operators using radial quantization and conformal gauge, which leads to a drastic simplification of the two-loop anomalous dimension calculation. We also find that the anomalous dimension calculation is closely related to a corresponding Witten diagram calculation.

Jets are complicated objects to identify in high energy collider experiments. A single interpretation of each event can only extract a limited amount of information. We propose telescoping jet algorithms which give multiple event interpretations by varying the parameter R in the jet definition. We can redefine the weight of each event in a counting experiment to be the fraction of interpretations passing the experimental cuts, and we get a 46% improvement in the statistical significance for the Higgs search with an associated Z boson at the 8 TeV LHC.

Contents

List of Figures

To my father who I wish I could share my life with more.

Acknowledgments

It has been a great experience to work at Harvard under the supervision of Professor Matthew Schwartz. I would like to thank him for his patience, support and all the advice he has given me through out these years. The work in this thesis was done in collaboration with numerous people. To Professor Iain Stewart at MIT, I would like to thank him for teaching SCET in an effective field theory course at MIT. To Randall Kelly, I would like to thank him for clarifying many concepts in SCET for me. To David Simmons-Duffin and Gim Seng Ng, I would like to thank them for many great conversations. I had a good time sharing the office with them, and we did a good job maintaining the chocolate supply. I have benefited much from being part of the high energy theory group, and the students and postdocs here are extremely helpful. Special thanks to David Krohn for many discussions about Qjets and collider physics techniques in general. I always understand more and learn a lot about high energy physics from talking to Ilya Feige, David Farhi, Jason Gallicchio, Marat Freytsis and Professor Matthew Reece. Through conversations with Chi-Ming Chang, Ying-Hsuan Lin, Clay Cordova, Loganayagam Ramalingam and Tatsuo Azeyanagi, I learn many fascinating hep-th ideas.

I am very grateful for the support of my family and friends. They have been part of my life. Special thanks to Sheila Ferguson who retired from the department office in 2012. She helped me through my family emergency, and I will always appreciate the warmth she gave me. I would also like to thank my girlfriend Hiroko. She tolerated me when I was occupied by research and postdoc applications, and we shared all the joy in life. Boston has become my second home, and I am very grateful to be able to live in this great city for six years.

This work is supported by the U.S. Department of Energy, under the grant DE-SC003916. Most of the computations were performed on the Odyssey cluster at Harvard University. The main body of the thesis consists of the following four papers I wrote with collaborators: Y. -T. Chien and M. D. Schwartz, "Resummation of heavy jet mass and comparison to LEP data," JHEP **1008**, 058 (2010), Y. -T. Chien, M. D. Schwartz, D. Simmons-Duffin and I. W. Stewart, "Jet Physics from Static Charges in AdS," Phys. Rev. D **85**, 045010 (2012), Y. -T. Chien, R. Kelley, M. D. Schwartz and H. X. Zhu, "Resummation of Jet Mass at Hadron Colliders," Phys. Rev. D **87**, 014010 (2013) and Y. -T. Chien, "Telescoping Jets: Multiple Event Interpretations with Multiple R's," arXiv:1304.5240 [hep-ph].

All truths are easy to understand once they are discovered; the point is to discover them.

Galileo Galilei

1 Introduction

The recent discovery of a Higgs-like particle at the LHC was a great accomplishment in particle physics. The non-hadronic decays of this Higgs candidate – as well as those of various new particles in models of physics beyond the Standard Model – have clean signals but the cross sections are very small. The future of the LHC will be to search for hadronic signals which have huge backgrounds. In order to distinguish a hadronic signal from its background it is important to develop advanced collider physics techniques that make accurate theoretical predictions.

Quantum chromodynamics complicates the study of physics at high energy scales, and most physics signals are buried in events with jets. Jets are a manifestation of the underlying colored partons in hard scattering processes. Colored partons emit soft and collinear hadrons around their directions of motion. We have complicated hadronic events with a huge number of particles in the final states. Reconstructing the information about hard collisions requires a precise understanding of the hadronic sector. Therefore precision jet physics becomes very important

as we ask detailed questions about hard processes.

It is crucial to develop observables that are both sensitive to new physics and are theoretically calculable with high precision. Among useful hadronic observables, jet mass is one of the simplest and most important examples. New physics particles may show up as peaks on top of background jet mass distributions. Therefore jet mass is a good starting point to look into issues in hadronic precision calculations. Observables like jet mass usually involve physics at different energy scales such as energies Q and masses m of jets. The calculation depends on large logarithms of the ratios of these energy scales $\log \frac{m}{Q}$. This causes a break-down of fixed-order perturbative calculations and the logarithms need to be resummed in order to make reliable theoretical predictions. In addition, experimental cuts introduce more scales and further complicate the comparison between theory and experiment.

An extremely important concept in high energy physics is the idea of factorization, which allows us to study physics at different scales separately. Hadronic cross sections of events at the LHC can be factorized as a convolution between Parton Distribution Functions (PDFs) of protons and partonic cross sections, up to corrections suppressed by $\frac{\Lambda_{\rm QCD}}{Q}$. Schematically,

$$d\sigma(pp \to X + \text{remnant}) = \sum_{ab} \text{PDF}_a(x_1) \otimes \text{PDF}_b(x_2) \otimes d\hat{\sigma}(ab \to X)(x_1, x_2) + \mathcal{O}(\frac{\Lambda_{\rm QCD}}{Q}) \ , \quad (1.1)$$

where the sum is over all possible partonic channels with the final state X ($X = l^+l^-$ for the Drell-Yan process), and x is the fraction of the proton momentum carried by the parton. PDFs encode the structure of proton and are governed by QCD at a low energy scale $\Lambda_{\rm QCD}$. On the other hand, partonic cross sections describe collisions at a high energy scale Q where QCD is perturbative. PDFs and partonic cross sections have different characteristic scales and are insensitive to each other. This allows the universality of PDFs for different processes to be possible. For deep inelastic scattering, the same set of PDFs enter into cross section calculations,

$$d\sigma(e^- p \to e^- X + \text{remnant}) = \sum_{a} \text{PDF}_a(x) \otimes d\hat{\sigma}(e^- a \to e^- X)(x) + \mathcal{O}(\frac{\Lambda_{\rm QCD}}{Q}) \ . \quad (1.2)$$

At high energy colliders, jet masses m can be much lower than jet energies Q. This leads to another level of factorization, which is the factorization of QCD interactions among colored

partons into hard, collinear and soft sectors. Their characteristic scales are Q and m, as well as the seesaw scale $\frac{m^2}{Q}$, respectively. The separation of scales makes effective field theories powerful techniques to resum large logarithms. Soft Collinear Effective Theory was constructed to organize the calculation in the full theory systematically in power counting. We can prove factorization theorems of observables, and partonic cross sections can be further factorized as a convolution between hard, jet and soft functions, up to corrections suppressed by λ,

$$\frac{d\hat{\sigma}}{dZ}(ab \to N \text{ jets}) = H(Q) \prod_i^N J_i \otimes S_{ab1\ldots N} \otimes \delta(Z - Z(p_c, p_s)) + \mathcal{O}(\lambda) \ , \tag{1.3}$$

where Z is some hadronic observable defined as a function of collinear and soft momenta of jet constituents. For jet mass, $Z = (p_c + p_s)^2$, and $\lambda = \frac{m}{Q}$ is the power counting parameter. In SCET, the hard function captures QCD interactions among partons at the hard scale Q, and it is independent of the definition of the jet observable Z. On the other hand, collinear and soft interactions are described by Wilson lines. The jet and soft functions give the contributions from collinear and soft radiation to the jet observable. The hard, jet and soft functions can be calculated perturbatively at their characteristic scales. Large logarithms can then be resummed by renormalization-group evolutions of hard, jet and soft functions between different scales.

For e^+e^- collisions, we don't have the complication of QCD interactions from initial states. So it is a clean starting point to study resummation of jet mass. In section 2.1, we calculate the distribution of heavy jet mass – which is the larger of the two hemisphere masses – at next-to-next-to-next-to leading logarithmic order (N^3LL). Using the LEP data we measure the strong coupling constant at 0.3% accuracy. Together with the thrust calculation by Becher and Schwartz, these are the most precise SCET calculations of hadronic observables to date. We also investigate the form of the multi-scale hemisphere soft function and reveal issues in resummation that are not present in the thrust calculation. By comparing with the perturbative QCD calculation in the literature, we cross-check the logarithmic terms and extract the power corrections at $\mathcal{O}(\alpha_s^3)$. This demonstrates the power of SCET for large-log resummation.

The heavy jet mass calculation prepares us for jet-mass resummation at the LHC. There are complications from proton beams and we are forced to consider exclusive jet observables. Here non-global logarithms cause extra complications in resummation. They come from phase

space separation in defining exclusive observables, and it is not clear how to resum non-global logarithms systematically. In section 2.2, we calculate the jet-mass distribution in γ + jet events at partial next-to-next-to leading logarithmic order ($\mathrm{N^2LL_p}$), neglecting non-global logarithms at $\mathcal{O}(\alpha_s^2)$. This is the first and most precise jet-mass distribution calculation at the LHC. We estimate the effect of non-global logarithms and we find that it is significant only at the peak region. However, we refactorize the soft sector and it might be possible to resum non-global logarithms using renormalization-group techniques. There is no data yet, so we compare our results with the results from PYTHIA and they agree very well away from the peak region. Our work can help calibrate hadronic event generators and it sets firm-theoretical ground for understanding the $\gamma/W/Z$ + jet background of all new physics signals, including the associated production of boosted Higgs bosons.

Jet functions are universal – process independent – like PDFs. Collinear sectors of different jets decouple from one another, and each collinear sector is only sensitive to the charge of the underlying parton. On the other hand, soft functions encode the color coherence information, and their calculations get much more complicated as the number of colored partons increases. Soft QCD interactions among colored partons can be described by multi-Wilson line operators, with each Wilson line pointing along one of the parton directions. These operators are important in the calculation of any hadronic observable, and their anomalous dimensions are key for higher-order resummation. New ways of studying anomalous dimensions of multi-Wilson line operators are therefore phenomenologically important. There was an interesting study by Maldacena on high spin operators in the context of the AdS/CFT correspondence. The work was based on the symmetry of the corresponding Wilson line configurations, and the scaling of the anomalous dimensions was determined purely by a symmetry argument. This suggested that, by using coordinates which manifest the symmetry of the problem, the structure of multi-Wilson line operators could be revealed in a simpler way.

In chapter 3, we show that it is most natural to study multi-Wilson line operators using radial quantization. Soft Wilson lines are mapped to static charges in Euclidean AdS space, and the anomalous dimension becomes the energy in the charge system. Furthermore, we introduce a new gauge – conformal gauge – which diagonalizes the gluon propagator in Euclidean AdS space. This eliminates the temporal and spatial mixing in many of the Feynman diagram calculations,

which leads to a drastic simplification of the two loop anomalous dimension calculation. We also find that the anomalous dimension calculation is closely related to a corresponding Witten diagram calculation. It would be interesting to apply Mellin representation techniques developed in Witten diagram calculations to study three loop anomalous dimensions, which are conjectured to have a simple structure depending linearly on the pairwise angles between Wilson lines.

In the previous jet-mass calculations, a jet is defined as the set of particles within a hemisphere or a cone of size R around the thrust or jet axis. A more standard way to identify jets is to use clustering algorithms with a parameter R. The idea is to merge the pair of particles with the shortest distance at each step until particles are far away from one another than R. The distance between a pair of particles is defined by a metric, and the three most popular ones are those of the anti-k_T, Cambridge/Aachen and k_T algorithms. The constituents of each reconstructed jet are those particles within an angular scale R away from the jet direction. Although we can choose an R to optimize an analysis, jets are conventionally reconstructed using the same R for all events. However, for each event we can extract more information if we probe each jet using multiple R's. This idea is referred to as telescoping jet algorithms. Each event reconstruction with a specific R is called an interpretation of the event.

In chapter 4, we use telescoping anti-k_T and cone algorithms in the Higgs search with an associated Z boson at the 8 TeV LHC. We study the $H \to b\overline{b}$ channel, with Z decaying leptonically. The background is $Z + b\overline{b}$ from $g \to b\overline{b}$, and we haven't looked into the b-tagging issue. We reconstruct the invariant mass of the b-jet pair and perform a counting experiment in the signal mass window between 110 and 140 GeV. The statistical significance $S/\delta B$ – the expected size of the signal divided by the size of the background fluctuation – is a good indicator of the possibility of seeing a Higgs mass peak standing out of the background mass distribution.

With multiple event interpretations we can redefine the weight of each event in the counting experiment to be the fraction of interpretations passing the experimental cuts, instead of 0 or 1 in a conventional analysis. With simulations we can weight each event using likelihood ratio method. The approach of using multiple interpretations increases the statistical stabilities of observables so that backbround fluctuations shrink considerably. This leads to a dramatic increase of the statistical power of the analysis. In particular, we can have a 46% improvement in the significance of the Higgs search.

I haven't encountered large logarithms which can not be resummed using renormalization-group techniques.

Iain W. Stewart, MIT

2

Precision Jet Physics using Effective Field Theory

2.1 **Resummation of Heavy Jet Mass and Comparison to LEP Data**

Event shapes in e^+e^- collisions provide some of the best ways to test QCD and the standard model. At high energies, where QCD is perturbative, event shapes lead to some of the world's most precise measurements of the strong coupling constant α_s. Recently, a number of theoretical advances have led to renewed interest in event shapes and the α_s measurements. First, the NNLO fixed order Feynman diagrams were calculated [1–4]. This allowed the prediction of all event shapes to order α_s^3. Second, advances [5–7] in Soft-Collinear Effective Theory (SCET) [8–10] have allowed resummation of the large logarithmic corrections to thrust to $\mathrm{N^3LL}$ accuracy [11]. Previous calculations were at NLO [12] and NLL [13]. Very recently, a full effective field theory analysis of a single event shape, thrust, has been completed [14], including additionally non-perturbative considerations. The resulting α_s extraction is competitive with the PDG world

average [15], however it differs significantly from measurements using lattice QCD and τ decays (see [16] for a review).

Although the α_s measurement with thrust is extremely precise, there are many reasons to study additional event shapes as well. The main advantage is that there may be systematic effects in a single event shape pulling α_s in a certain direction, which are not universal. In fact, as observed in [17] from an NLL+NNLO analysis, there seem to be two classes of event shapes, the first including thrust, the C-parameter and total jet broadening, while the second includes heavy jet mass, wide jet broadening and the two-to-three jet transition parameter y_3. The values of α_s extracted from the two classes at NLL+NNLO tend to have around a 5% systematic difference which the authors attribute to missing higher order corrections. In a recent world average of α_s [16], the thrust measurement using SCET was not included because of a concern over precisely this kind of systematic uncertainty. In this paper, we correct that concern with a $\mathrm{N^3LL}$ calculation of an event shape from the second class, heavy jet mass.

In addition to being useful for measuring α_s, the heavy jet mass distribution allows us to explore other aspects of resummation. Indeed, there are few hadronic observables which have been calculated this accurately and for which there is data. Heavy jet mass involves a soft function which cannot be written in terms of only a single scale. These types of soft functions promise to play an important role in resummation at hadron colliders and only beginning to be explored [18–20]. We will discuss constraints on the soft function, and perform a numerical study of the parts that are not known, similar to what was done in [11] and [21].

Hadronization is another issue which having a second event shape may help understand. In the fit to α_s with the thrust distribution [11], it was observed that a decrease in α_s could be compensated for with a single non-perturbative parameter with only a small effect on the χ^2 of the fit. Having another observable for which the same non-perturbative parameters can be fit can possibly remove this flat direction. The hadronization issue is also important for Monte Carlo simulations. With a more accurate theoretical calculations, we can explore whether the approximations in PYTHIA [22] allow for an adequate description of thrust and heavy jet mass simultaneously.

As a brief outline of our findings, we begin in Section 2.1.1 with an overview of the SCET distributions. The hemisphere soft function is studied and singular terms in the heavy jet

mass distribution are compared to the fixed order calculation in Section 2.1.2. We found a mild inconsistency with the analytic results from SCET and the numerical calculations of the NLO and NNLO distributions. After completing the original study, we were able to resolve this inconsistency, which was due to Monte Carlo convergence problems, by taking a very low numerical infrared cutoff, as discussed in a note added at the end of this paper. In Section 2.1.3 we fit for α_s. The fit for heavy jet mass to the LEP data from ALEPH [23] leads to $\alpha_s(m_Z) = 0.1220 \pm 0.0031$. This value is higher than the value from thrust using exactly the same technique, $\alpha_s(m_Z) = 0.1175 \pm 0.0026$. Assuming 100% correlation gives an average value of $\alpha_s(m_Z) = 0.1193 \pm 0.0027$ which is very close to the recent average in [16]. We also find that convergence of the perturbation series for heavy jet mass with resummation is, like for thrust, significantly better than the convergence of the fixed order calculation. In Section 2.1.4, a comparison of the data to PYTHIA shows that while PYTHIA agrees with the thrust data almost perfectly, it has trouble matching the heavy jet mass distribution. Moreover, the hadronization corrections in PYTHIA move the curve in the wrong direction for heavy jet mass. Concluding that the Monte Carlo hadronization model is incompatible with the high precision theoretical calculation, we explore non-perturbative corrections in SCET with a simple shape function. We find that to the order we are working, this simple shape function cannot simultaneously describe the thrust and heavy jet mass distributions. We provide an expanded summary, discussion and comparison to previous results in Section 2.1.5.

2.1.1 Thrust and Heavy Jet Mass in SCET

Thrust and heavy jet mass are defined as follows. One first finds the thrust axis, through

$$T = \max_{\mathbf{n}} \frac{\sum_i |\mathbf{p}_i \cdot \mathbf{n}|}{\sum_i |\mathbf{p}_i|}, \tag{2.1}$$

where the sum is over all momentum 3-vectors $\mathbf{p}_i$ in the event, and the maximum is over all unit 3-vectors $\mathbf{n}$. We use $\tau = 1 - T$ to measure thrust. Once the thrust axis is known, it can be used to split the event into two hemispheres. We define P_L^μ and P_R^μ to be the four momenta of the sum of all the radiation going into each hemisphere, and $M_L = \sqrt{P_L^2}$ and $M_R = \sqrt{P_R^2}$ to be the hemisphere masses. Heavy jet mass ρ is defined as the larger of the two hemisphere masses

squared, normalized to the the center of mass energy Q,

$$\rho \equiv \frac{1}{Q^2} \max(M_L^2, M_R^2)\,. \tag{2.2}$$

When ρ is small, τ is also small, both hemisphere masses are small, and the event appears to have two back-to-back pencil-like jets. In this threshold limit, the thrust axis aligns with the jet axis and $Q^2\tau$ approaches the sum of the two hemisphere masses squared $M_L^2 + M_R^2 = Q^2\tau + \mathcal{O}(\tau^2)$.

It follows that both thrust, up to power corrections, and heavy jet mass can be written as integrals over the doubly differential hemisphere mass distribution:

$$\frac{\mathrm{d}\sigma}{\mathrm{d}\tau} = Q^2 \int \frac{\mathrm{d}^2\sigma}{\mathrm{d}M_L^2 \mathrm{d}M_R^2} \delta(Q^2\tau - M_L^2 - M_R^2)\,, \tag{2.3}$$

$$\frac{\mathrm{d}\sigma}{\mathrm{d}\rho} = Q^2 \int \frac{\mathrm{d}^2\sigma}{\mathrm{d}M_L^2 \mathrm{d}M_R^2} \left[\delta(Q^2\rho - M_L^2)\theta(M_L^2 - M_R^2) + \delta(Q^2\rho - M_R^2)\theta(M_R^2 - M_L^2)\right]\,. \tag{2.4}$$

In SCET, the doubly differential hemisphere mass distribution is calculable in the threshold limit. The appropriate factorization theorem in SCET was first derived in [5] for the related process of $t\bar{t}$ production. This theorem was then shown to allow for the calculation of event shapes in [6], where matched and resummed thrust and heavy jet mass distributions in SCET were first presented. Previously, resummation of heavy jet mass was only possible at NLL accuracy [13]. The first event shape resummed to N^{3}LL was thrust, in [11]. Monte Carlo based hadronization corrections were included in [24] to produce a strong model-independent gluino mass bound. Recently, power corrections for thrust were studied within the effective field theory approach in [14].

The factorization theorem allows us to write the hemisphere mass distribution as

$$\frac{1}{\sigma_0} \frac{\mathrm{d}^2\sigma_2}{\mathrm{d}M_L^2 \mathrm{d}M_R^2} = H(Q^2, \mu) \int \mathrm{d}k_L \mathrm{d}k_R\, J(M_L^2 - Qk_L, \mu)\, J(M_R^2 - Qk_R, \mu)\, S(k_L, k_R, \mu)\,. \tag{2.5}$$

The subscript on σ_2 is a reminder that this expression holds in the two-jet region. Here, $H(Q^2, \mu)$ is the hard function. It is calculated in matching SCET to QCD and contains information about the modes of QCD that are not in SCET. $J(p^2, \mu)$ is a jet function. It is derived in a matching calculation from a theory with soft and collinear modes to a theory with just soft modes. The

hard function was calculated in [25] and the jet functions in [7]. Finally, $S(k_L, k_R, \mu)$ is the hemisphere soft function which is derived from integrating out the remaining soft modes.

The doubly differential hemisphere mass distribution, Eq. (2.5), is observable, and therefore must be independent of renormalization group scale μ. Demanding μ-independence leads to a renormalization group equation which is easiest to express in Laplace space, where the convolutions turn into products. The Laplace transform is defined by

$$\widetilde{f}(\nu_L, \nu_R) = \int \mathrm{d}M_L^2 \mathrm{d}M_R^2 e^{-\nu_L M_L^2} e^{-\nu_R M_R^2} f(M_L^2, M_R^2) \tag{2.6}$$

which can be applied to the differential cross section and to the jet and soft functions separately. We generally express the Laplace transformed distributions as functions of $L_1 = \ln(\mu \nu_L e^{\gamma_E})$ and $L_2 = \ln(\mu \nu_R e^{\gamma_E})$. Since the entire μ-dependence of the hard and jet functions is known, the μ-dependence of the soft function is completely fixed by renormalization group invariance (see [11] for more details). The result is that the hemisphere soft function itself factorizes into the form [5, 6, 21, 26]

$$\widetilde{s}(L_1, L_2, \mu) = \widetilde{s}_\mu(L_1, \mu)\widetilde{s}_\mu(L_2, \mu)\widetilde{s}_f(L_1 - L_2)\,, \tag{2.7}$$

where all the μ-dependence is contained in the function $\widetilde{s}_\mu(L, \mu)$ which is known to N^{3}LL accuracy. Since $L_1 - L_2 = \ln(\nu_L/\nu_R)$, the function $\widetilde{s}_f(L_1 - L_2)$ is μ-independent. We discuss the soft function more in the next section.

Putting together the hard and jet functions with the soft function written in this way produces an analytic expression for the doubly differential jet mass distribution. For thrust, the result is [11]

$$\begin{aligned}
\frac{1}{\sigma_0} R_2^\tau(\tau) &= \frac{1}{\sigma_0} \int_0^\tau \mathrm{d}\tau' \frac{\mathrm{d}\sigma_2}{\mathrm{d}\tau'} \\
&= \exp\left[4S(\mu_h, \mu_j) + 4S(\mu_s, \mu_j) - 2A_H(\mu_h, \mu_s) + 4A_J(\mu_j, \mu_s)\right] \left(\frac{Q^2}{\mu_h^2}\right)^{-2A_\Gamma(\mu_h, \mu_j)} \\
&\quad \times H(Q^2, \mu_h) \left[\widetilde{j}\Big(\ln\frac{\mu_s Q}{\mu_j^2} + \partial_\eta, \mu_j\Big)\right]^2 \widetilde{s}_T(\partial_\eta, \mu_s) \left[\left(\frac{\tau Q}{\mu_s}\right)^\eta \frac{e^{-\gamma_E \eta}}{\Gamma(\eta + 1)}\right],
\end{aligned} \tag{2.8}$$

with $\eta = 4A_\Gamma(\mu_j, \mu_s)$ and the thrust soft function $\widetilde{s}_T(L, \mu)$ is defined by

$$\widetilde{s}_T(L, \mu) = \widetilde{s}(L, L, \mu) = [\widetilde{s}_\mu(L, \mu)]^2 \widetilde{s}_f(0)\,. \tag{2.9}$$

The definitions of the RG kernels $A_\Gamma(\nu, \mu)$ and $S(\nu, \mu)$ as well as the fixed order hard and jet functions, $H(Q^2, \mu)$ and $\widetilde{j}(L, \mu)$ and their anomalous dimensions can be found in [11]. Note that only one value of the unknown function $\widetilde{s}_f(L)$ is required for thrust.

For heavy jet mass, the distribution is similar

$$\begin{aligned}
\frac{1}{\sigma_0} R_2^\rho(\rho) &= \frac{1}{\sigma_0} \int_0^\rho \mathrm{d}\rho' \frac{\mathrm{d}\sigma_2}{\mathrm{d}\rho'} \\
&= \exp\left[4S(\mu_h, \mu_j) + 4S(\mu_s, \mu_j) - 2A_H(\mu_h, \mu_s) + 4A_J(\mu_j, \mu_s)\right] \left(\frac{Q^2}{\mu_h^2}\right)^{-2A_\Gamma(\mu_h, \mu_j)} \\
&\times H(Q^2, \mu_h) \widetilde{j}\Big(\ln\frac{\mu_s Q}{\mu_j^2} + \partial_{\eta_1}, \mu_j\Big) \widetilde{j}\Big(\ln\frac{\mu_s Q}{\mu_j^2} + \partial_{\eta_2}, \mu_j\Big) \widetilde{s}_\mu(\partial_{\eta_1}, \mu_s) \widetilde{s}_\mu(\partial_{\eta_2}, \mu_s) \left(\frac{\rho Q}{\mu_s}\right)^{\eta_1+\eta_2} \\
&\times \widetilde{s}_f(\partial_{\eta_1} - \partial_{\eta_2}) \frac{e^{-\gamma_E \eta_1}}{\Gamma(\eta_1 + 1)} \frac{e^{-\gamma_E \eta_2}}{\Gamma(\eta_2 + 1)}\,,
\end{aligned} \tag{2.10}$$

where $\eta_1 = \eta_2 = 2A_\Gamma(\mu_j, \mu_s)$. In contrast to thrust, for heavy jet mass the full functional form of $\widetilde{s}_f(L)$ is needed. For N^{3}LL precision, we need to know the hemisphere soft function, and hence $\widetilde{s}_f(L)$ to two-loop order (NLO). Actually, to this order, we only need one projection of the hemisphere soft function. For three-loop matching (NNLO), we need an additional projection. These projections will be discussed in the next section.

One interesting feature of the hemisphere mass distribution is that the soft interference effects in $\widetilde{s}_f(L)$ are only relevant at α_s^2, which is appropriate for N^{3}LL resummation. Up to NNLL accuracy, the doubly differential distribution is simply the product of the mass distributions in the two hemispheres. Explicitly,

$$R(M_L^2, M_R^2) = \int_0^{M_L^2} \mathrm{d}M_L^{2\prime} \int_0^{M_R^2} \mathrm{d}M_R^{2\prime} \frac{\mathrm{d}^2\sigma}{\mathrm{d}M_L^{2\prime}\mathrm{d}M_R^{2\prime}} = K(M_L^2) K(M_R^2)\,, \tag{2.11}$$

where

$$K(M^2) = \exp\left[2S(\mu_h, \mu_j) + 2S(\mu_s, \mu_j) - A_H(\mu_h, \mu_s) + 2A_J(\mu_j, \mu_s)\right] \left(\frac{Q^2}{\mu_h^2}\right)^{-A_\Gamma(\mu_h, \mu_j)}$$

$$\times \sqrt{H(Q^2,\mu_h)\widetilde{s}_f(0)}\,\widetilde{j}\Big(\ln\frac{\mu_s Q}{\mu_j^2}+\partial_\eta,\mu_j\Big)\,\widetilde{s}_\mu(\partial_\eta,\mu_s)\left(\frac{M^2}{\mu_s Q}\right)^{\eta}\frac{e^{-\gamma_E\eta}}{\Gamma(\eta+1)}\,, \quad (2.12)$$

and $\eta = 2A_\Gamma(\mu_j,\mu_s)$. Since, for NNLL resummation, the hard and jet functions are only needed to $\mathcal{O}(\alpha_s)$, the square-roots above simply mean take one half of the α_s pieces. The fact that the distribution splits up in this way was observed at NLL level in [6], and is essential to the traditional NLL resummation [13]. This simplified factorization suggests that it may be possible to calculate observables involving many more jets with NNLL resummation without having to disentangle soft interference effects. Note that this factorization does not guarantee that large logs of M_L^2/M_R^2 can be resummed. However, it is possible that the calculation of observables with only one scale, such as the sum of many jet masses, or a maximal jet mass, will simplify with SCET.

2.1.2 Hemisphere Soft Function and Comparison to Fixed Order

The hemisphere soft function has been studied briefly in [5, 6, 26] and more thoroughly in [21]. It is a function of two scales, k_L and k_R as well as the renormalization group scale μ. If n_L^μ is the direction of the left hemisphere and k_L^μ is the sum of the momenta of all the soft radiation entering this hemisphere, then k_L is the component of k_L^μ backwards to n_L^μ. That is $k_L = (k_L{\cdot}n_L)$. k_R is defined analogously. The soft function can be factorized into a perturbative, partonic part, and non-perturbative contribution which has support of order $\Lambda_{\rm QCD}$. For now we deal only with the perturbative part, discussing non-perturbative effects in Section 2.1.4.

As we have noted, the soft function itself factorizes.

$$\widetilde{s}(L_1,L_2,\mu) = \widetilde{s}_\mu(L_1,\mu)\widetilde{s}_\mu(L_2,\mu)\widetilde{s}_f(L_1-L_2) \quad (2.13)$$

where $\widetilde{s}(L_1,L_2,\mu)$ is the Laplace transform of $S(k_L,k_R,\mu)$, as in Eq. (2.6), and $L_1 = \ln(\mu\nu_L e^{\gamma_E})$, $L_2 = \ln(\mu\nu_R e^{\gamma_E})$. The function $\widetilde{s}_\mu(L,\mu)$ is completely fixed by RG invariance in terms of the hard and jet anomalous dimensions. It can be calculated in perturbation theory by demanding Eq. (2.10) be independent of μ. This gives

$$\widetilde{s}_\mu(L,\mu) = \exp\Big[\left(\frac{\alpha_s}{4\pi}\right)\left(-L^2\Gamma_0 + L\gamma_0^S\right) + \left(\frac{\alpha_s}{4\pi}\right)^2\left(\frac{2}{3}L^3\beta_0\Gamma_0 + L^2(-\Gamma_1-\beta_0\gamma_0^S) + L(\gamma_1^S)\right)$$

$$+\left(\frac{\alpha_s}{4\pi}\right)^3\left(-\frac{2}{3}L^4\beta_0^2\Gamma_0+\frac{2}{3}L^3(\beta_1\Gamma_0+2\beta_0\Gamma_1+2\beta_0^2\gamma_0^S)+L^2(-\Gamma_2-\beta_1\gamma_0^S-2\beta_0\gamma_1^S)+L(\gamma_2^S)\right)$$
$$+\cdots\Big]\,. \quad (2.14)$$

The μ-independent part $\widetilde{s}_f(L)$ must satisfy a number of constraints, as discussed in [21].

First of all, since the soft function is symmetric in the two hemispheres, $\widetilde{s}_f(L)$ must be an even function of L. Second of all, we know the function to order α_s by explicit calculation. Writing

$$\widetilde{s}_f(L)=1+\left(\frac{\alpha_s}{4\pi}\right)\widetilde{s}_{f1}(L)+\left(\frac{\alpha_s}{4\pi}\right)^2\widetilde{s}_{f2}(L)+\cdots\,, \quad (2.15)$$

the one-loop result is that

$$\widetilde{s}_{f1}(L)=-C_F\pi^2\,. \quad (2.16)$$

The authors of [21] also observed that $\widetilde{s}_f(L)$ is constrained by the non-Abelian exponentiation theorem. Non-Abelian exponentiation implies constraints on powers of logarithms of μ in the full soft function. These constraints are satisfied by the explicit solution, since $\widetilde{s}_\mu(L,\mu)$ is an exponential. The theorem also restricts the C_F^n color structure in the soft function to be completely determined by the one-loop result, Eq. (2.16). Beyond this, however, $\widetilde{s}_f(L)$ is unconstrained. It may even have more general dependence on L than logarithms. To determine $\widetilde{s}_f(L)$, we must calculate the soft function perturbatively. The one-loop calculation has been done but the two-loop calculation, which is required for N^{3}LL resummation, has not.

A simple alternative to calculating $\widetilde{s}_f(L)$ at NNLO is to extract projections of $\widetilde{s}_f(L)$ from numerical comparisons to event shape calculations in full QCD. For example, thrust is only sensitive to $\widetilde{s}_f(0)$. Writing

$$\widetilde{s}_f(0)=1+\left(\frac{\alpha_s}{4\pi}\right)c_1^S+\left(\frac{\alpha_s}{4\pi}\right)^2c_2^S+\cdots\,, \quad (2.17)$$

and comparing to Eq. (2.16), we see that $c_1^S=-C_F\pi^2$. The two-loop constant was determined numerically in [11] with the use of the EVENT 2 program [27]. The result is

$$c_2^S=(58\pm2)C_F^2+(-60\pm1)C_FC_A+(43\pm1)C_FT_Fn_f \quad \text{(Becher and Schwartz)} \quad (2.18)$$

This is in conflict with the prediction from non-Abelian exponentiation, which requires the C_F^2 factor be $\frac{1}{2}\pi^4 C_F^2 = 48.7 C_F^2$. The two-loop constant was also determined in [21], using the same technique but imposing non-Abelian exponentiation. They found

$$c_2^S = \frac{\pi^4}{2} C_F^2 + (-59 \pm 2) C_F C_A + (44 \pm 3) C_F T_F n_f \quad \text{(Hoang and Kluth)} \tag{2.19}$$

The two results agree, except for the C_F^2 term. Indeed, the C_F^2 term seems to indicate a disagreement between the numerical results of the EVENT 2 program and the prediction from non-Abelian exponentiation. Since the uncertainty in Eq (2.18) is too small to explain this disagreement, it is reasonable also to expect the other color structures to be off. We should therefore allow for a systematic uncertainty on these fits in addition to what is presented, which is essentially a statistical uncertainty associated with the fit. We discuss this more below.

Event shapes other than thrust are sensitive to the form of $\widetilde{s}_f(L)$, not just $\widetilde{s}_f(0)$. This can be seen, for example, by the form of the heavy jet mass distribution in Eq. (2.10). For N^{3}LL resummation, the fixed order expansion is required to α_s^2. The contribution at this order involving $\widetilde{s}_f(L)$ requires at most $\widetilde{s}_{f2}(L)$, with the jet and hard functions at their tree-level values. Thus, the required projection of the $\widetilde{s}_f(L)$ for heavy jet mass is

$$c_{2\rho}^S = \widetilde{s}_{f2}(\partial_{\eta_1} - \partial_{\eta_2}) \left. \frac{e^{-\gamma_E \eta_1}}{\Gamma(\eta_1 + 1)} \frac{e^{-\gamma_E \eta_2}}{\Gamma(\eta_2 + 1)} \right|_{\eta_1 = \eta_2 = 0} = \frac{1}{\pi} \int_0^\pi \widetilde{s}_{f2}(iL) \mathrm{d}L \,. \tag{2.20}$$

The integral representation of $c_{2\rho}^S$ is suggestive of a deeper relation between heavy jet mass and the hemisphere mass distribution, however we do not have a physical explanation of why this particular moment appears. If $\widetilde{s}_f(L)$ is a polynomial, this moment is very simple. For example, if we assume

$$\widetilde{s}_f(L) = 1 + \left(\frac{\alpha_s}{4\pi}\right) c_1^S + \left(\frac{\alpha_s}{4\pi}\right)^2 \left[c_2^S + c_{2L}^S L^2 + c_{2Q}^S L^4\right] , \tag{2.21}$$

then

$$c_{2\rho}^S = c_2^S - c_{2L}^S \frac{\pi^2}{3} + c_{2Q}^S \frac{\pi^4}{5} \,. \tag{2.22}$$

At NLO, the singular part of the heavy jet mass distribution only depends on $\widetilde{s}_f(L)$ through $c_{2\rho}^S$. Thus, we can fit $c_{2\rho}^S$ numerically the same way c_2^S is fit with thrust.

To determine $c_{2\rho}^S$ we use the same technique used in [11] for thrust, and in [21] for a one-

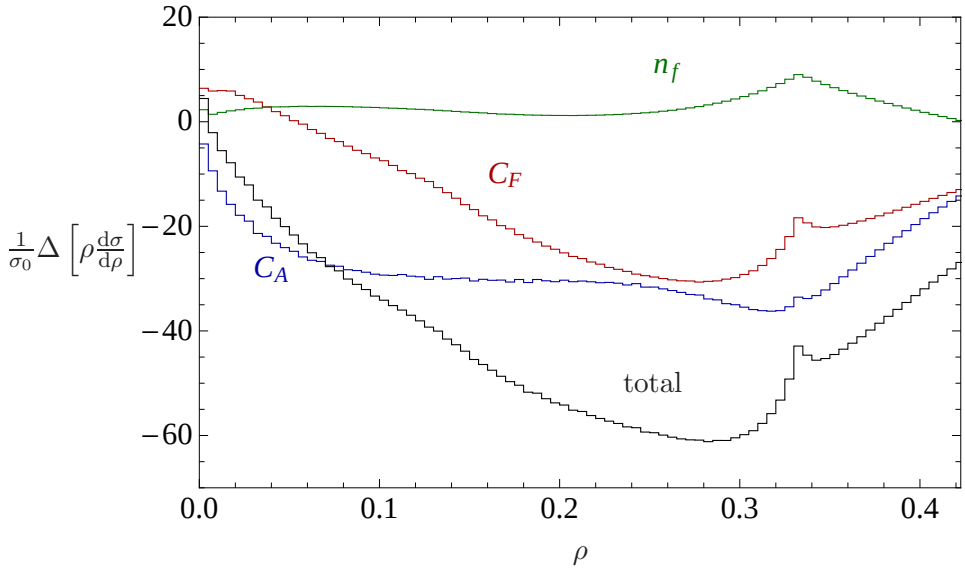

Figure 2.1: A comparison of the full fixed-order calculations and expanded SCET at NLO. Shown is the difference $\frac{1}{\sigma_0}\rho\Delta\frac{d\sigma}{d\rho} = \rho(B(\rho) - D_B(\rho))$, where $B(\rho)$ is the full NLO B-function, calculated with EVENT 2 and $D_B(\rho)$ is the singular part, calculated with SCET. The differences are separated by color structure, with the sum also shown. The kink at $\rho = \frac{1}{3}$ is the maximum heavy jet mass for a 3-particle final state. (See also Figure 2.11.)

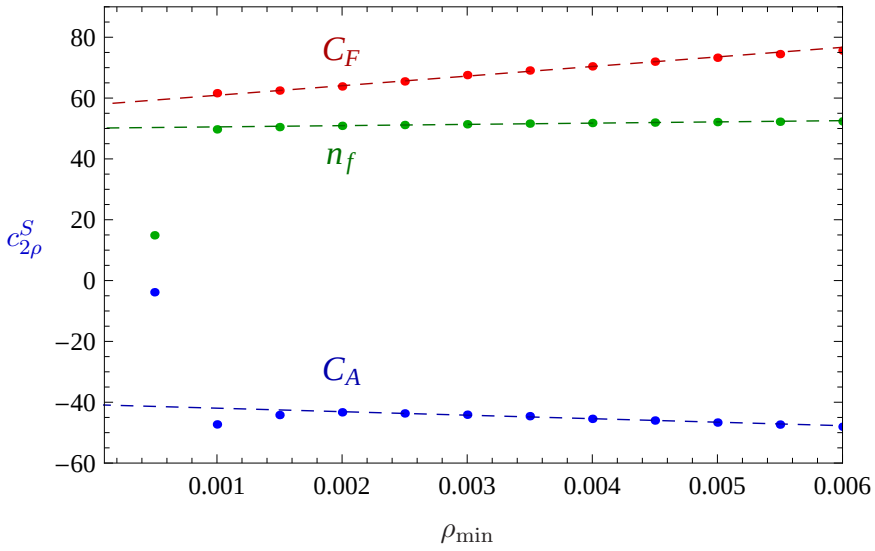

Figure 2.2: Extraction of the two-loop constants in the soft function. The points correspond to the value of a lower bound $\rho_{\min}$ applied to the fixed-order calculation. The lines are interpolations among the points from $\rho_{\min} = 0.002$ to $\rho_{\min} = 0.005$ extrapolated to $\rho = 0$ to extract the constants.(See also Figure 2.12.)

parameter family of event shapes. The basic idea is that the singular part of the heavy jet mass distribution is known analytically, through SCET. The difference between the exact NLO heavy jet mass distribution and this singular part is finite and can be integrated numerically. This integral is then the total cross section at NLO minus the integral of the singular part which is

calculable analytically and depends on the constants c_2^S for thrust and $c_{2\rho}^S$ for heavy jet mass.

In more detail, the exact heavy jet mass distribution can be expanded as a series in α_s

$$\frac{1}{\sigma_0}\frac{\mathrm{d}\sigma}{\mathrm{d}\rho} = \left(\frac{\alpha_s}{2\pi}\right) A(\rho) + \left(\frac{\alpha_s}{2\pi}\right)^2 B(\rho) + \left(\frac{\alpha_s}{2\pi}\right)^3 C(\rho) + \cdots . \tag{2.23}$$

Each term in this series is singular at $\rho = 0$. The singular parts can be written as a sum of distributions

$$\frac{1}{\sigma_0}\frac{\mathrm{d}\sigma}{\mathrm{d}\rho} = \delta(\rho) D_\delta + \left(\frac{\alpha_s}{2\pi}\right) [D_A(\rho)]_+ + \left(\frac{\alpha_s}{2\pi}\right)^2 [D_B(\rho)]_+ + \left(\frac{\alpha_s}{2\pi}\right)^3 [D_C(\rho)]_+ + \cdots . \tag{2.24}$$

The functions D_δ, $D_A(\rho)$, $D_B(\rho)$, and $D_C(\rho)$ are calculable in SCET and we give them in Appendix A.3. Up to order α_s^2, the only dependence on the unknown soft function coefficient $c_{2\rho}^S$ is in D_δ, thus the shape of the singular part of the NLO distribution is known completely. The corresponding exact distributions in perturbative QCD have been calculated for $\rho > 0$ analytically for the A function, and numerically for the B and C functions. Since SCET produces the entire singular part of the distributions, the combination

$$\frac{1}{\sigma_0}\Delta\left[\rho\frac{\mathrm{d}\sigma}{\mathrm{d}\rho}\right] = \rho B(\rho) - \rho D_B(\rho)\,, \tag{2.25}$$

should vanish at $\rho = 0$. We show this difference separated by color structure in Figure 2.1. The B functions are calculated using the Monte Carlo program EVENT 2 [27] with 10^{10} events. Curiously, while the C_F and C_A color structures do not seem to go to 0 as $\rho \to 0$, their sum does.

With these difference functions, it is straightforward to extract $c_{2\rho}^S$ as in [11] and [21]. Although the difference $\rho B(\rho) - \rho D_B(\rho)$ is regular at $\rho = 0$, the two functions are separately divergent. Since $D_B(\rho)$ is only known numerically, the difference is numerically unstable at small ρ. To do the $c_{2\rho}^S$ extraction, we use the same procedure as in [11] and impose an lower bound and take the limit that the bound is removed. The extracted values as a function of this lower bound $\rho_{\min}$ are shown in Figure 2.2. We then fit a line in the region $0.002 \leq \rho_{\min} \leq 0.005$

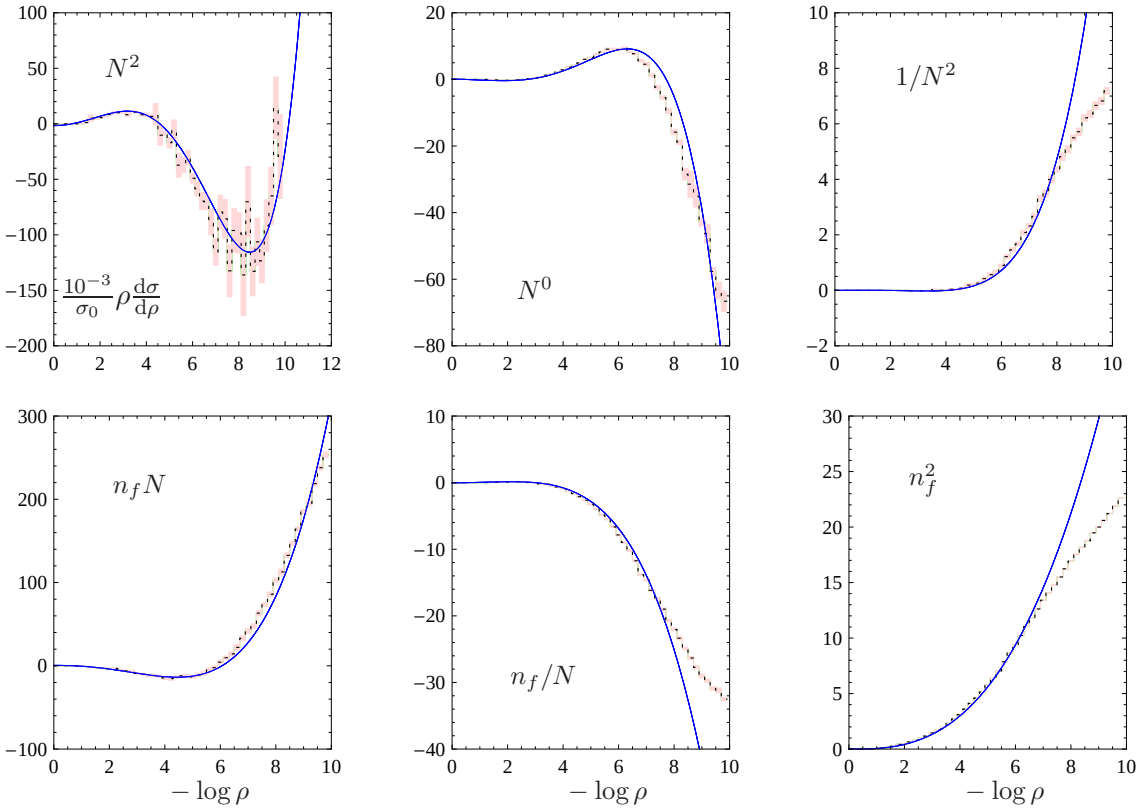

Figure 2.3: Comparison of the full NNLO heavy jet mass distribution $C(\rho)$ (dashed black histograms) [28] and the singular terms $D_C(\rho)$ (blue curves). The light-red areas are an estimate of the statistical uncertainty. The uncertainties on c_2^S and c_{2L}^S, in Eq (2.33), are not visible. The disagreement at very small ρ is due to the infrared cut-off of $y_0 = 10^{-5}$ for the NNLO calculation. It is expected that the agreement would improve if this cutoff were lowered, as can be seen in the analogous thrust plot in [11]. (See also Figure 2.13.)

and extrapolate to $\rho_{\min} = 0$. The result is

$$c_{2\rho}^S = (58 \pm 2)C_F^2 + (-41 \pm 2)C_F C_A + (50 \pm 1)C_F T_F n_f \,. \tag{2.26}$$

Note that the C_F and C_A curves have problems at small $\rho_{\min}$, in agreement with what is seen in Figure 2.1. Since the approach is linear up to around $\rho_{\min} \sim 0.002$, it is likely that this divergence is an unphysical systematic problem with the Monte Carlo, and not due to low statistics or a discrepancy with theory. [1] As with c_2^S, non-Abelian exponentiation implies that the C_F^2 term should be $\frac{1}{2}\pi^4 \approx 48.7$. Thus, our uncertainty of $c_{2\rho}^S$ from the extrapolation is probably too small and we will therefore inflate the errors by a factor of 5. (See also Eq. (2.50) and Figures 2.11 and 2.12 for an update.)

[1] We thank A. Hoang for a discussion of this point.

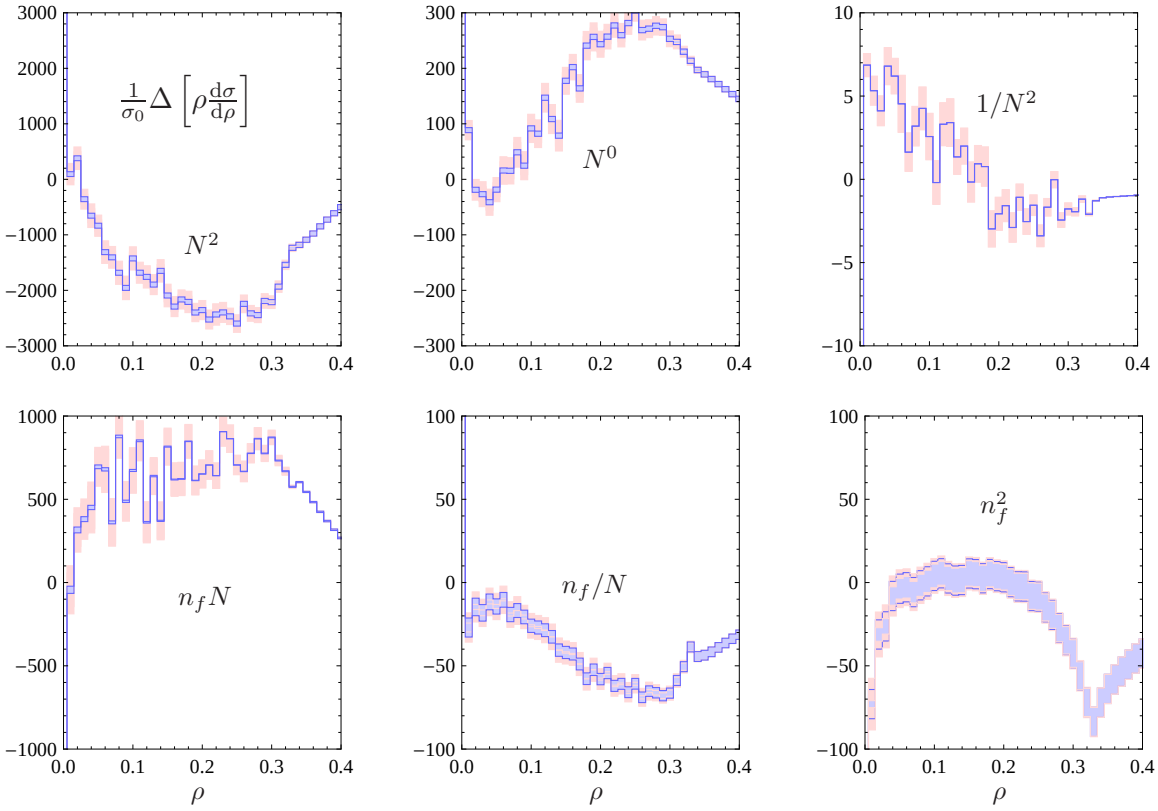

Figure 2.4: The difference, $\frac{1}{\sigma_0}\rho\Delta\frac{d\sigma}{d\rho} = \rho(C(\rho) - D_C(\rho))$, between the full NNLO heavy jet mass distribution and the singular terms. The light-red areas are an estimate of the statistical uncertainty, from [28]. The blue band is the uncertainty due to c_2^S and c_{2L}^S, in Eq (2.33). These curves should all go to 0 at $\rho = 0$. The $C(\rho)$ distributions are all calculated with an infrared cutoff of $y_0 = 10^{-5}$. (See Figure 2.14 for the same figure with $y_0 = 10^{-7}$.)

To calculate the heavy jet mass distribution to N^{3}LL+NNLO accuracy, we must match to the NNLO fixed order distribution. This requires the singular parts of heavy jet mass to α_s^3, that is, the function $D_C(\rho)$ in Eq. (2.24). To derive this, we do not need the finite part of the soft function at α_s^3, $\widetilde{s}_{f3}(L)$, since this piece only contributes to the α_s^3 part of D_δ, which is not required for matching. We do, however, need another projection of the α_s^2 soft function, of the form

$$c_{2\zeta}^S = (\partial_{\eta_1} + \partial_{\eta_2})\widetilde{s}_{f2}(\partial_{\eta_1} - \partial_{\eta_2})\left.\frac{e^{-\gamma_E\eta_1}}{\Gamma(\eta_1+1)}\frac{e^{-\gamma_E\eta_2}}{\Gamma(\eta_2+1)}\right|_{\eta_1=\eta_2=0} \tag{2.27}$$

$$= \frac{2}{\pi}\int_0^\pi \widetilde{s}_{f2}(iL)\ln\left[2\cos(\frac{L}{2})\right]\mathrm{d}L\,. \tag{2.28}$$

Again, we have no physical explanation of the intriguing integral definition in the second line.

This projection also simplifies with a polynomial soft function. For example, with Eq (2.21)

$$c_{2\zeta}^S = 4\zeta_3 c_{2L}^S + (-8\pi^2\zeta_3 + 48\zeta_5) c_{2Q}^S \,. \tag{2.29}$$

The prediction from SCET for $D_C(\rho)$ with its explicit dependence only on $c_{2\rho}^S$ and $c_{2\zeta}^S$ is given in Appendix A.3. There are only three color structures which depend on $c_{2\zeta}^S$ at all.

In order to extract the L dependence of $\widetilde{s}_{f2}(L)$, we could attempt to fit $c_{2\zeta}^S$ with the shapes of the NNLO distributions. An alternative, as pursued by Hoang and Kluth in [21], is to use the other event shapes beyond thrust and heavy jet mass at NLO. These authors considered a weighted sum of the jet masses, $\tau_\alpha = \frac{2}{1+\alpha}(\alpha M_L^2 + M_R^2)/Q^2$. This form leads to a singular distribution which depends on $\widetilde{s}_{f2}(\ln\alpha)$, hence combining event shapes with different α can probe the entire function $\widetilde{s}_{f2}(L)$. Their fits show good agreement with the form

$$\widetilde{s}_f(L) = 1 + \left(\frac{\alpha_s}{4\pi}\right) c_1^S + \left(\frac{\alpha_s}{4\pi}\right)^2 \left[c_2^S + c_{2L}^S L^2\right] \,, \tag{2.30}$$

which they have argued is likely to be the exact 2-loop soft function. We will therefore assume this form of the soft function as well, in order to proceed with the N^{3}LL+NNLO α_s fits. [2]

With this soft function and the thrust fit values in Eq. (2.18), our fit for $c_{2\rho}^S$ translates into a fit for c_{2L}^S (cf. Eq.(2.22) with $c_{2Q}^S = 0$) The result is

$$c_{2L}^S = (0 \pm 2) C_F^2 + (-5.8 \pm 1.5) C_F C_A + (-2.2 \pm 1) C_F T_F n_f \,. \tag{2.31}$$

Using a similar technique, but imposing the constraint from non-Abelian exponentiation, Hoang and Kluth found results consistent with ours

$$c_{2L}^S = (0) C_F^2 + (-6.5 \pm 2) C_F C_A + (1.3 \pm 2) C_F T_F n_f \quad \text{(Hoang and Kluth)} \tag{2.32}$$

Note that for c_{2L}^S, the C_F^2 coefficient comes out to be consistent with the prediction from non-

[2] There is a subtlety about these τ_α event shapes because of non-global logarithms [29]. For example, for very large or small α, these event shapes reduce to the left or right hemisphere mass, which are known to have non-global logs. Since $\tau_\alpha \to 0$ forces the massless dijet threshold, in which the SCET factorization theorem is derived, only up to corrections of order $\ln\alpha$, it is not completely clear that SCET will reproduce all of the α-dependence of the singular terms in τ_α.

Abelian exponentiation. Since c_{2L}^S comes from the difference between the values extracted from thrust and the values extracted from heavy jet mass, the systematic problem with EVENT 2 may be cancelling in the difference. Thus, we will inflate our uncertainties on c_{2L}^S by only a factor of 2.

In summary, for the rest of this paper, we will take

$$\widetilde{s}_f(L) = 1 + \left(\frac{\alpha_s}{4\pi}\right) c_1^S + \left(\frac{\alpha_s}{4\pi}\right)^2 \left[c_2^S + c_{2L}^S L^2\right] \tag{2.33}$$

$$c_2^S = \frac{\pi^4}{2} C_F^2 + (-60 \pm 10) C_F C_A + (43 \pm 5) C_F T_F n_f \tag{2.34}$$

$$c_{2L}^S = (0) C_F^2 + (-6 \pm 3) C_F C_A + (-2 \pm 2) C_F T_F n_f \,, \tag{2.35}$$

so that

$$c_{2\zeta}^S = 4\zeta_3 c_{2L}^S \quad \text{and} \quad c_{2\rho}^S = c_2^S - \frac{\pi^2}{3} c_{2L}^S \,. \tag{2.36}$$

The uncertainty on α_s due to the uncertainty on these numbers will be included in the fits.

Before moving on the α_s extraction, we can compare the SCET prediction for the singular parts of the NNLO distribution to the exact results, as was done for thrust in [11]. To do this, we use $D_C(\rho)$ from Appendix A.3 with the substitutions in Eq. (2.36). This lets us compare to the C functions in the NNLO distribution, from [28]. Plots of ρD_C and ρC are shown in Figure 2.3 as functions of $\log \rho$. The uncertainty on c_2^S and c_{2L}^S is included, but not visible in these plots. Although the agreement is not perfect at very small ρ, it is expected to improve, as we seen for thrust in [11], as the the infrared cutoff used in the NNLO calculation is reduced from the value $y_0 = 10^{-5}$ used here. A version of this plot with cutoff $y_0 = 10^{-7}$ has been included as Figure 2.13, confirming our expectations.

The difference between the full NNLO distribution and its singular parts, as in Eq. (2.25), is shown in Figure 2.4. These curves, for all color structures, should go to zero at $\rho = 0$. For most of the color structures, this looks plausible, although the $1/N^2$ color structure, corresponding to the $\alpha_s^3 C_F^3$ coefficient in the heavy jet mass distribution which is fixed by non-Abelian exponentiation, looks a bit suspicious. Because this constant is known, we have not included an associated uncertainty. The discrepancy is likely due to the infrared cutoff $y_0 = 10^{-5}$ used for these plots

(an update with $y_0 = 10^{-7}$ is included as Figure 2.14). Note that even if the Ansatz in Eq. (2.33) were wrong, a general dependence on $c_{2\zeta}^S$ will only affect some of the color structures, and even then would only generate an overall up or down shift in these curves (cf. the form of D_C in Eq. (A.13)).

2.1.3 α_s extraction and error analysis

In the previous section, we determined the unknown coefficients in the hemisphere soft function and checked the singular terms against the exact NLO and NNLO heavy jet mass distributions. Now we are ready to compare to data and fit for the strong coupling constant α_s. The procedure we follow is identical to the procedure used for thrust in [11], so we refer the reader to that paper for missing details.

For heavy jet mass, as for thrust, we match to the fixed order distribution via

$$\frac{1}{\sigma_0}\frac{\mathrm{d}\sigma}{\mathrm{d}\rho} = \frac{1}{\sigma_0}\frac{\mathrm{d}\sigma_2}{\mathrm{d}\rho} + r(\rho)\,, \tag{2.37}$$

with

$$r(\rho) = \left(\frac{\alpha_s}{2\pi}\right)[A(\rho) - D_A(\rho)] + \left(\frac{\alpha_s}{2\pi}\right)^2[B(\rho) - D_B(\rho)] + \left(\frac{\alpha_s}{2\pi}\right)^3[C(\rho) - D_C(\rho)]\,, \tag{2.38}$$

and D_A, D_B and D_C are given in Appendix A.3. The A function is known analytically, and is the same as for thrust (see [6]). For $B(\rho)$ we use the output of EVENT 2 [27], and for $C(\rho)$ we use the NNLO calculation which has been provided to us by the authors of [3]. We normalize to the total hadronic cross section at order α_s^2, which is

$$\frac{\sigma_{\mathrm{had}}}{\sigma_0} = 1 + \frac{\alpha_s}{4\pi}[3C_F] + \left(\frac{\alpha_s}{4\pi}\right)^2\left[C_F C_A\left(\frac{123}{2} - 44\zeta_3\right) + C_F T_F n_f\,(-22 + 16\zeta_3) - C_F^2\frac{3}{2}\right]\,. \tag{2.39}$$

Since the data is binned, what we actually use for the theory prediction is the difference between the integrated heavy jet mass distribution evaluated at the bin edges: $R_\rho(\rho_2) - R_\rho(\rho_1)$. Our fit ranges are chosen to be the same as in [30], so that we can use their values for the systematic experimental uncertainties.

The left panel of Figure 2.5 shows a comparison of the theory prediction for heavy jet mass

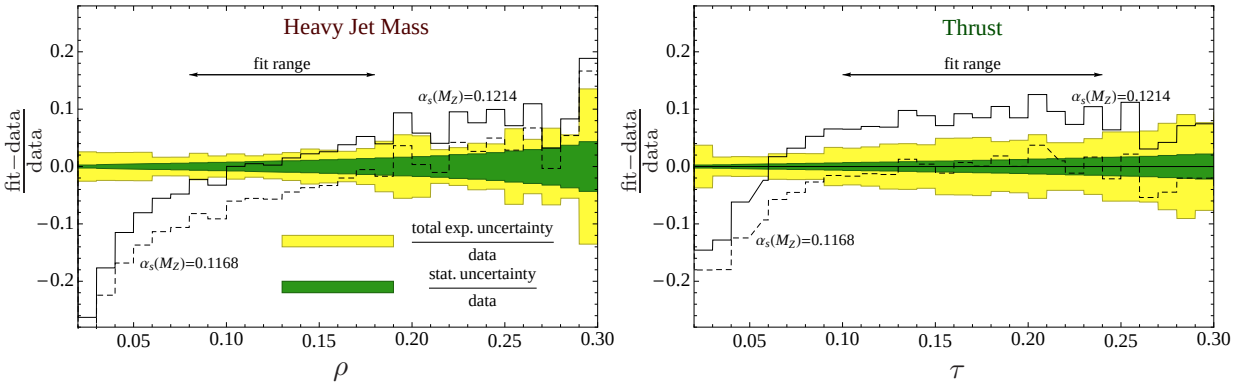

Figure 2.5: Relative error for best fit to ALEPH data at 91.2 GeV. The inner green band includes only statistical uncertainty, while the outer yellow band includes statistical, systematic and generator uncertainties. The solid black line is for $\alpha_s(M_Z) = 0.1214$, the best fit value for heavy jet mass, while the dashed line has $\alpha_s(m_Z) = 0.1168$, the best fit for thrust. The fit ranges, $0.08 < \rho < 0.18$ and $0.1 < \tau < 0.24$, are taken from [30].

to the ALEPH data at 91.2 GeV. These curves use the default scale choices

$$\mu_h = Q, \quad \mu_j = Q\sqrt{\rho}, \quad \mu_s = Q\rho\,. \tag{2.40}$$

These scales are the natural ones to minimize the large logarithms, and can be read off the formula in Eq. (2.10). The best fit value of α_s for heavy jet mass is $\alpha_s(m_Z) = 0.1214$. We show also in the same figure, the heavy jet mass distribution for $\alpha_s(m_Z) = 0.1168$, which is the value of α_s derived in [11] from the fit to the thrust distribution at the same energy. In the right panel of Figure 2.5, we show a comparison to data for thrust, with the same values of α_s. Overall, the fit to thrust is a much better fit. For heavy jet mass, the best fit gives χ^2/d.o.f.=67/9 using statistical uncertainties only, while for thrust, χ^2/d.o.f.=32.5/13. The relatively poor fit for heavy jet mass can be plainly seen in the figure. For thrust, the relative distribution is flat over the fit range (dashed curve, right panel), while for heavy jet mass, it is increasing (solid curve, left panel). This coordinates with the relatively larger power corrections that we will find in the next section.

Next, we look at the uncertainties on the theoretical prediction. As with thrust, in [11], we consider first separate variations of μ_h, μ_j, μ_s and the scale μ_m where the matching is done by factors of 2. Figure 2.6 shows the effect of the envelope of these variations on the heavy jet mass distribution, for four orders in perturbation theory. We use the same definitions for the various

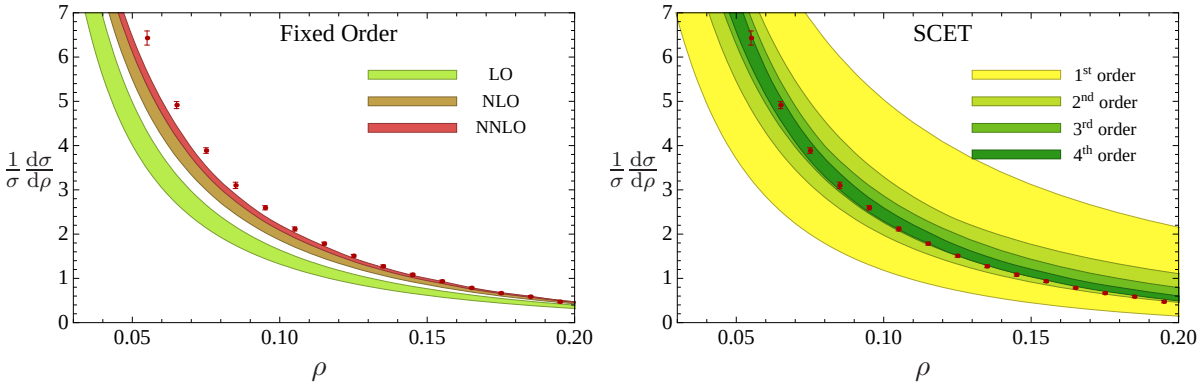

Figure 2.6: Convergence of resummed and fixed-order distributions. ALEPH data (red) at 91.2 GeV is included for reference. All plots have $\alpha_s(m_Z) = 0.1214$.

orders as in [11]:

Order	resum.	Γ_{cusp}	γ_n	c_n	matching
1^{st} order	NLL	2-loop	1-loop	tree	–
2^{nd} order	NNLL	3-loop	2-loop	1-loop	LO
3^{rd} order	N^3LL	4-loop	3-loop	2-loop	NLO
4^{th} order	N^3LL	4-loop	3-loop	3-loop	NNLO

The first three orders correspond to traditional counting in renormalization-group improved perturbation theory, while 4^{th}order simply uses all the available information.

Next, we consider, the separate variations. The bands in the first four panels of Figure 2.7 show the effect of the scale uncertainties. The bottom two panels of Figure 2.7 show the effect of the more natural correlated and anti-correlated scale variations introduced in [11]. The correlated variation is defined to hold μ_j/μ_s fixed. So we vary

$$\mu_j \to c\sqrt{\tau}Q, \quad \mu_s \to c\tau Q\,, \quad \frac{1}{2} < c < 2\,. \tag{2.41}$$

This probes the upper and lower limits on μ_j and μ_s, but avoids the unphysical region where $\mu_s < \mu_j$ or $\mu_h < \mu_j$. The orthogonal anti-correlated variation is defined to hold $\mu_j^2/(Q\mu_s)$ fixed. It is

$$\mu_j^2 \to aQ^2\tau \quad \mu_s \to aQ\tau, \quad \frac{1}{\sqrt{2}} < a < \sqrt{2}\,. \tag{2.42}$$

This is independent from the correlated mode but again avoids unphysical scale choices.

Overall, we find good convergence order-by-order in perturbation theory. However, some of

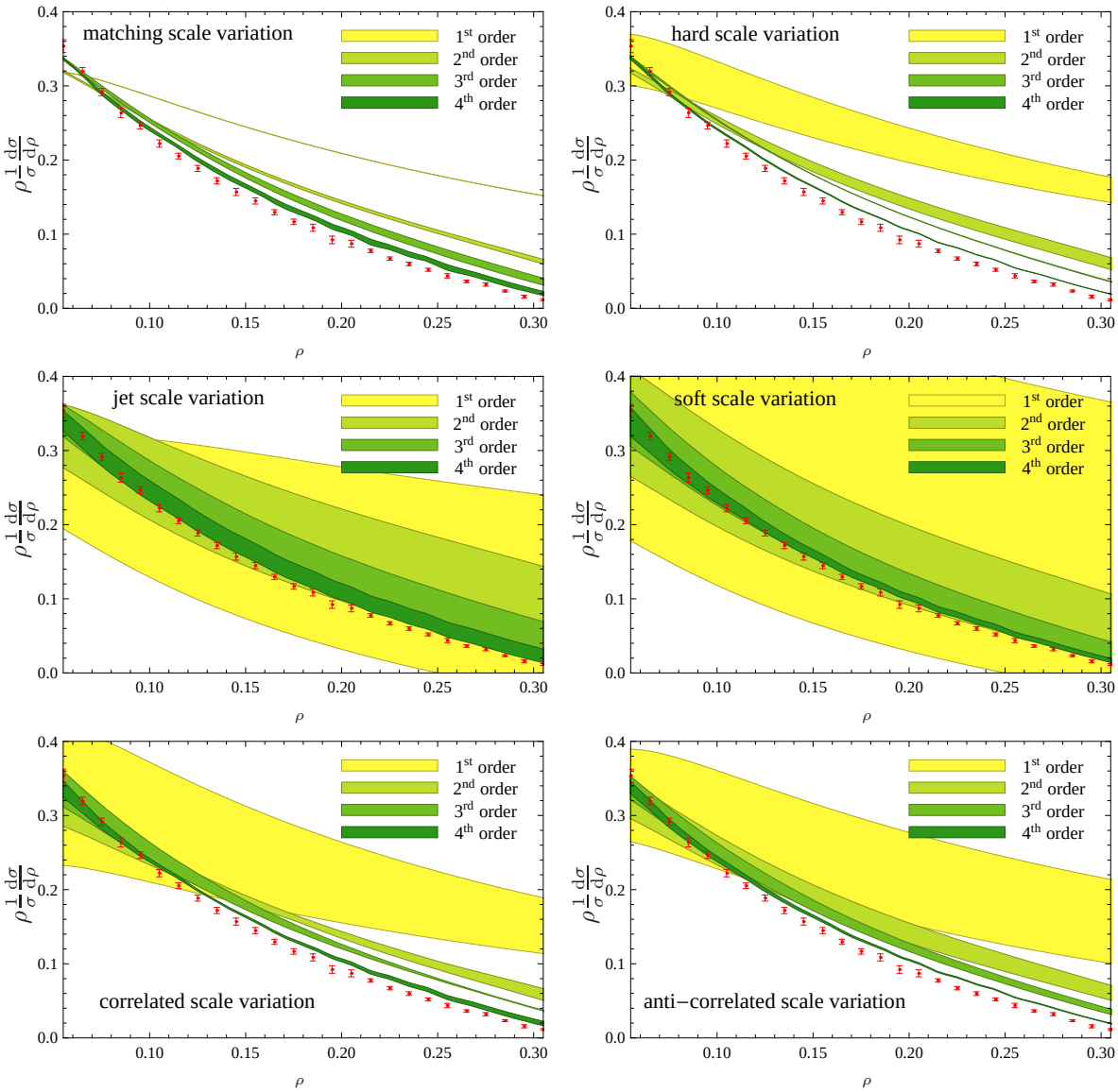

Figure 2.7: Perturbative uncertainty at $Q = 91.2\,\text{GeV}$. Each of the scales is varied separately by a factor of two around the default value. We show $\frac{1}{\sigma}\rho\frac{d\sigma}{d\rho}$ and, for reference, ALEPH data at LEP 1 scaled by the central value of each bin. All plots have $\alpha_s(m_Z) = 0.1214$.

the higher-order scale variations are outside of the range of the lower orders. This was not the case for thrust, where the central value of the prediction was much more stable. Nevertheless, for both thrust and heavy jet mass, the complete perturbative uncertainty, defined as the envelope of the various variations (that is, the maximum and minimum over them) does have the higher-order bands contained within the lower order bands, as can be seen in Figure 2.6.

Next, we fit the theoretical prediction to the ALEPH data from 91.2 to 206 GeV [23] and extract α_s. The fit is done by minimizing the χ^2, using experimental statistical uncertainties,

Table 2.1: Best fit to ALEPH data. The row labelled "pert err." is derived from scale uncertainties and the row labelled "soft err." from the uncertainty on c_2^S and c_{2L}^S in Eq.(2.33). The rows labeled PYTHIA and ARIADNE give the value of α_s after correcting for hadronization and quark masses using PYTHIA or ARIADNE. The ARIADNE corrected prediction for the two highest two energies produce very poor fits, and are excluded from the average

Q	91.2	133	161	172	183	189	200	206	AVG
fit range	0.08 0.18	0.06 0.25	0.06 0.25	0.06 0.25	0.06 0.25	0.04 0.20	0.04 0.20	0.04 0.20	–
χ^2/d.o.f.	67/9	2.3/4	0.66/4	1.8/4	5.2/4	1.1/4	8.8/4	3.8/4	–
stat. err.	0.0002	0.0055	0.0108	0.0144	0.0065	0.0032	0.0034	0.0034	0.0015
syst. err.	0.0011	0.0011	0.0011	0.0011	0.0012	0.0013	0.0014	0.0011	0.0013
hadr. err.	0.0044	0.0028	0.0022	0.0021	0.0019	0.0018	0.0017	0.0016	0.0022
pert. err.	$^{+0.0006}_{-0.0011}$	$^{+0.0006}_{-0.0011}$	$^{+0.0009}_{-0.0014}$	$^{+0.0003}_{-0.0005}$	$^{+0.0007}_{-0.0011}$	$^{+0.0006}_{-0.0009}$	$^{+0.0006}_{-0.0008}$	$^{+0.0005}_{-0.0007}$	0.0009
soft. err.	0.0005	0.0005	0.0006	0.0002	0.0005	0.0004	0.0004	0.0004	0.0004
tot. err.	0.0047	0.0064	0.0112	0.0147	0.0070	0.0040	0.0041	0.0040	0.0031
$\alpha_s(m_Z)$	0.1214	0.1235	0.1328	0.1077	0.1267	0.1234	0.1218	0.1189	0.1220
PYTHIA	0.1365	0.1239	0.1333	0.1073	0.1266	0.1214	0.1202	0.1168	0.1230
ARIADNE	0.1238	0.1262	0.1355	0.1093	0.1288	0.1239	0.1731	0.1687	0.1250

for the theory prediction with default scale choices. The **statistical** error on α_s is determined by variations around this minimum. The **perturbative** uncertainty is extracted with the uncertainty band method [31], exactly as in [11] for thrust. The envelope over the hard, matching, correlated and anti-correlated scale variations are included in this extraction. We also include an additional **soft** uncertainty associated with the errors in the extraction of c_2^S and c_{2L}^S. These are computed by fitting α_s within the errors on c_2^S and c_{2L}^S in Eq. (2.33), and taking the difference with the central value as the uncertainty. The soft and perturbative uncertainties are assumed uncorrelated. The **systematic** uncertainties are taken from [30]. To use these uncertainties, we are forced to keep our fit ranges the same as in [30]. The **hadronization** uncertainties are also taken from [30], which are based on Monte Carlo simulations. Note that, as in [11], we use the uncertainties from [30] but do not correct for hadronization. Hadronization will be discussed in detail in Section 2.1.4. Finally, the values for each energy are combined with a weight inversely proportional to the square of that energy's total error. The statistical uncertainties are assumed uncorrelated, and combined in quadrature, while for the other uncertainties a linear weighted average is performed. The results are tabulated in Table 2.1.

We show in Figure 2.8 the convergence of the best fit values as a function of energy. There is very good consistency among the different energies and the convergence order-by-order in

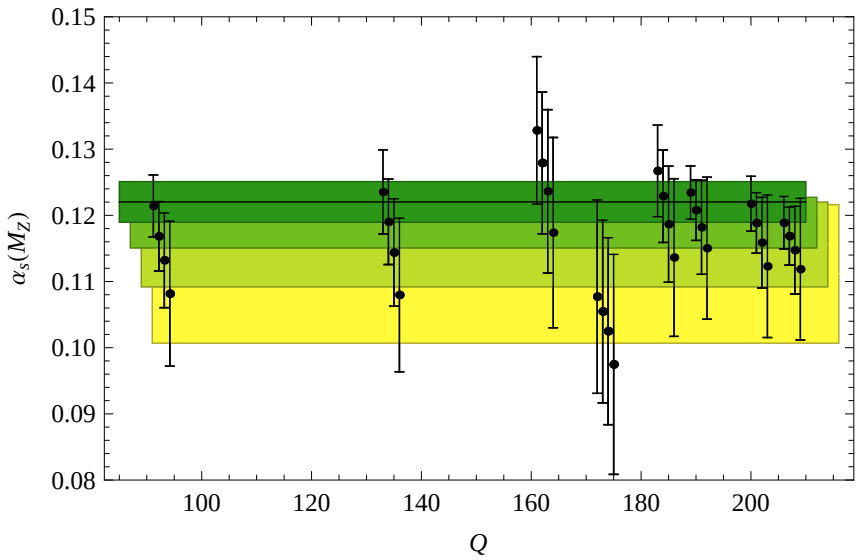

Figure 2.8: Best fit values for $\alpha_s(m_Z)$. From right to left the lines are the total error bars at each energy for first order, second order, third order and fourth order, as defined in the text. The bands are weighted averages with errors combined from all energies.

Table 2.2: Best fit values and uncertainties at different orders.

	LEP 1 +LEP 2			LEP 1 (91.2 GeV only)		
order	α_s	total err	pert. err	α_s	tot.err	pert.err
1^{st}order	0.1111	0.0104	0.0100	0 1099	0.0100	0.0110
2^{nd}order	0.1156	0.0064	0.0057	0.1132	0.0072	0.0055
3^{rd}order	0.1189	0.0038	0.0025	0.1168	0.0052	0.0026
4^{th}order	0.1220	0.0031	0.0009	0.1214	0.0047	0.0011

perturbation theory is good as well. The fit values for different orders are given in Table 2.2.

The final fit for heavy jet mass gives

$$\begin{aligned}\alpha_s(m_Z) &= 0.1220 \pm 0.0014\ (\text{stat}) \pm 0.0013\ (\text{syst}) \pm 0.0022\ (\text{had}) \pm 0.0009\ (\text{pert}) \pm 0.0004\ (\text{soft}) \\ &= 0.1220 \pm 0.0031 \quad \textbf{(Heavy Jet Mass)}\,. \end{aligned} \tag{2.43}$$

This can be compared to the result for thrust, using exactly the same technique, and the same energy ALEPH data (Table 2 of [11]). Updating this result to include the more recent NNLO distributions [3, 4], using the same c_2^S values, Eq.(2.33), with associated "soft" uncertainty, and restricting to only the ALEPH data, we find

$$\alpha_s(m_Z) = 0.1175 \pm 0.0009\ (\text{stat}) \pm 0.0011\ (\text{syst}) \pm 0.0014\ (\text{had}) \pm 0.0016\ (\text{pert}) \pm 0.0006\ (\text{soft})$$

$$= 0.1175 \pm 0.0026 \quad \textbf{(Thrust)}\,. \tag{2.44}$$

Combining these results, assuming 100% correlation between heavy jet mass and thrust, gives

$$\begin{aligned}\alpha_s(m_Z) &= 0.1193 \pm 0.0011\ (\text{stat}) \pm 0.0012\ (\text{syst}) \pm 0.0017\ (\text{had}) \pm 0.0013\ (\text{pert}) \pm 0.0005\ (\text{soft}) \\ &= 0.1193 \pm 0.0027 \quad \textbf{(Combined)}\,. \end{aligned} \tag{2.45}$$

This value is consistent with the recent world average of $\alpha_s(m_Z) = 0.1184 \pm 0.0007$ [16].

2.1.4 Non-perturbative effects and quark mass corrections

The α_s fit from the previous section used the theory prediction at the parton level with five flavors of massless quarks, neglecting hadronization and quark masses. Hadronization induces a power correction on the heavy jet mass distribution. Its effect is suppressed by a small scale, such as $\Lambda_{\rm QCD}/Q$ or $\Lambda_{\rm QCD}/\mu_s$ relative to the perturbatively calculable part. The b-quark mass corrections are suppressed by m_b/Q. These effects are therefore both parametrically smaller than the large logarithmic corrections which we resum. Nevertheless, they are quantitatively important, and our final uncertainty on α_s is dominated by the way these power corrections are modeled. The dominant part of the b-quark mass corrections is calculable, and is expected to shift α_s at around the 1% level, as observed in [11, 14]. The inclusion of b-quark corrections will be an important addition for future work. However, since they scale like $1/Q$, the dominant effect of these mass corrections can be absorbed into the same power correction model as hadronization effects, which also scale as $1/Q$. In this section, we explore the Monte Carlo treatment of power corrections, and an alternative theoretical model.

Monte Carlo simulations can include quark masses explicitly. They also attempt to model hadronization, for example with a string fragmentation model in PYTHIA. This produces an event with stable particles which can be run through a detector simulation. Such simulations are an essential part of every experimental study, and must play some role even for inclusive event shape analysis. For example, the event shape is often measured using only the charged particles, whose momenta are more precisely known, and then corrected to all particles with help of the simulation. Monte Carlo hadronization models have a number of free parameters

and can usually be tuned to any particular data set so that the simulation reproduces the data quite well. However, no single tuning reproduces all the data, and therefore different tunings are often used for different analyses. A more troubling fact is that, as demonstrated in [11], the tunings often correct for features having nothing to do with hadronization, such as subleading log resummation. Such tunings are guaranteed not to scale well with energy. This may be a serious problem for high energy colliders which simultaneously probe many energy scales, such as the Large Hadron Collider at CERN.

The hadronization uncertainty we used for the α_s determination were taken from [30], but we have also studied hadronization and mass effects in the Monte Carlos on our own. The last two rows of Table 2.1 show the best fit vales for α_s after the theory is corrected bin-by-bin for both hadronization and bottom and charm quark mass corrections using the Monte Carlo event generators PYTHIA V6.409, with default parameters [22], and ARIADNE V4.12 with the ALEPH tune [32]. Recall that ARIADNE actually feeds through PYTHIA to handle hadronization, so the difference is entirely due to the way the parton shower is implemented. With thrust, the same exercise was performed, and the corrections with ARIADNE were found to be very small, which helped justify not correcting for hadronization and quark masses at all in the published α_s fits. For thrust corrected with PYTHIA, there was a systematic downward shift in α_s. For heavy jet mass, the corrections with ARIADNE are large. In fact, for the high energy data, ridiculous values such as $\alpha_s = 0.1731$ result. The PYTHIA corrections are, for heavy jet mass, smaller than they are for thrust. In fact, we find a bigger discrepancy between the thrust and heavy jet mass α_s fits after correcting with either Monte Carlo than without. Thus, although we cannot justify correcting the theory curve with either Monte Carlo, we confirm that the hadronization uncertainties listed in Table 2.1, which were taken from [30], span reasonable Monte-Carlo simulated variations due to hadronization and quark mass effects.

To understand why the power corrections come out so differently for thrust and heavy jet mass, we compare PYTHIA at the parton and hadron levels to the 4^{th}order SCET prediction (N^3LL + NNLO), and to the ALEPH data at 91.2 GeV in Figure 2.9. From the top two panels, we see that in the peak region, in both cases the parton-level theory prediction comes out somewhere between the parton and hadron level Monte Carlo. However, in the bottom two panels, which zoom in near the fit region, the difference between the two event shapes is much

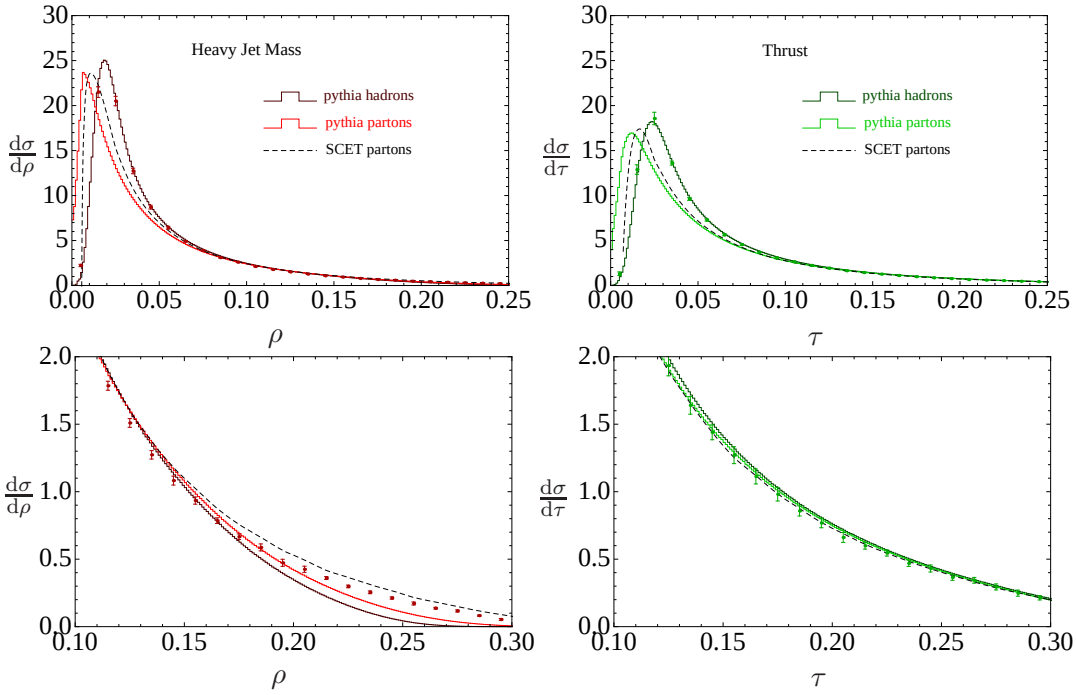

Figure 2.9: Hadronization and mass corrections with PYTHIA. The theoretical prediction using PYTHIA at the hadron level with massive quarks and the parton level with massless quarks is compared to data and to the 4^{th}order theoretical prediction using SCET. For thrust, PYTHIA agrees remarkably well with the data, while for heavy jet mass, there is a substantial discrepancy especially in the fit region, which is zoomed in on in the bottom panels.

more dramatic. For heavy jet mass, the SCET curve is above the data, while partonic PYTHIA is below it and hadronic PYTHIA is even farther below. In contrast, for thrust, all of the curves are much closer and the power corrections, as modeled by PYTHIA are a much smaller effect. It is clear that PYTHIA has trouble handling both event shapes simultaneously.

An alternative to using Monte Carlo simulations to simulate hadronization is to model the power corrections directly with effective field theory. As discussed in [21], hadronization effects can be absorbed into the soft function by convolution of the perturbatively calculable part with a non-perturbative shape function

$$S_{\text{full}}(k_L, k_R, \mu) = \int \mathrm{d}k'_L \mathrm{d}k'_R S_{\text{part}}(k_L - k'_L, k_R - k'_R, \mu) S_{\text{mod}}(k'_L, k'_R)\,, \tag{2.46}$$

where $S_{\text{part}}(k_L, k_R, \mu)$ is what we have previously just been calling $S(k_L, k_R, \mu)$ and $S_{\text{mod}}(k_L, k_R)$ is a non-perturbative model function. Generally, $S_{\text{mod}}(k_L, k_R)$ is expected to have support only for $k_L, k_R \lesssim \Lambda_{\text{QCD}}$. As observed in [33], there is an ambiguity in the factorization of the soft

function into these two pieces, which leads to a difficulty in assigning physical significance to $S_{\rm mod}(k_L, k_R)$ and poor convergence in perturbation theory. This ambiguity is associated with the existence of a renormalon, which can be removed within SCET [21,33]. Indeed, if data closer to the peak region were included in the fit, or if convergence of the model function parameters were an issue, removing the renormalon could have an important effect. Since we are not immediately interested in these issues, for simplicity, we will simply ignore the renormalon.

The simplest model function is just composed of delta functions

$$S_{\rm mod}(k_L, k_R) = \delta(k_L - \frac{1}{2}\Lambda_{\rm NP})\delta(k_R - \frac{1}{2}\Lambda_{\rm NP})\,. \tag{2.47}$$

The one parameter, $\Lambda_{\rm NP}$, can be thought of as representing the mass gap of QCD due to hadronization and therefore should be of order $\Lambda_{\rm QCD}$. This model function allows us to fit the leading power correction. Any other one-parameter family of shape functions can be written in this form up to higher power corrections, which should have a subleading effect on the distributions. For example, the smallest scale probed in our fits is the soft scale at the lower end of the fit region at 91.2 GeV, $\mu = \mu_s = \rho Q > (0.08)(91.2\text{ GeV}) \sim 7$ GeV. With $\Lambda_{\rm QCD} \sim 300$ MeV, this can be a 4% effect. Higher power corrections, of order $(\Lambda_{\rm QCD}/\mu)^2$ should have less than a 0.2% effect in our fit range.

Once this shape function is convoluted with the perturbative distribution, it has the effect of simply shifting the distributions

$$\frac{\mathrm{d}\sigma}{\mathrm{d}\tau}(\tau) \to \frac{\mathrm{d}\sigma}{\mathrm{d}\tau}(\tau - \Lambda_{\rm NP}) \tag{2.48}$$

$$\frac{\mathrm{d}\sigma}{\mathrm{d}\rho}(\rho) \to \frac{\mathrm{d}\sigma}{\mathrm{d}\rho}(\rho - \frac{1}{2}\Lambda_{\rm NP})\,. \tag{2.49}$$

The factor of $\frac{1}{2}$ is easy to understand. The shift causes each hemisphere mass to increase by $\frac{1}{2}\Lambda_{\rm NP}$. Since thrust sums both hemisphere masses, while heavy jet mass measures only one, heavy jet mass feels only half of the increase.

This model was studied for thrust in [11], where it was found that a larger $\Lambda_{\rm NP}$ can be compensated for by smaller α_s leading to a flat direction in the two parameter fits. We reproduce this result in Figure 2.10. This figure shows the 2σ and 5σ confidence regions in a combined fit

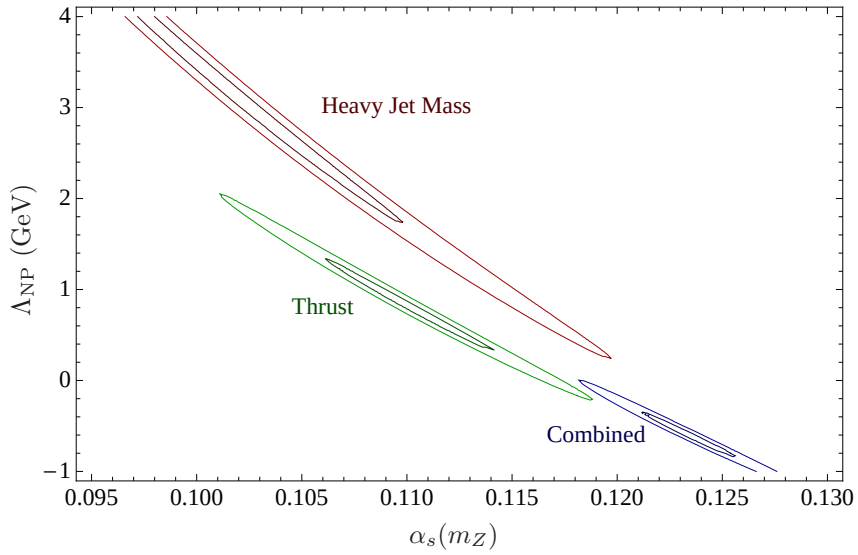

Figure 2.10: Contours of 2σ and 5σ confidence in the simultaneous fit of α_s and a non-perturbative shift parameter $\Lambda_{\rm NP}$ to the thrust and heavy jet mass ALEPH data from 91.2 to 206 GeV. The combined fit is also shown.

Table 2.3: Best fit values including leading power correction. The χ^2 is calculated using both statistical and experimental systematic uncertainties.

Event Shape	$\alpha_s(m_Z)$	$\Lambda_{\rm NP}$ (GeV)	χ^2/d.o.f.
Thrust	0.1101	0.821	66.9/47
Heavy Jet Mass	0.1017	3.17	60.4/43
Combined	0.1236	-0.621	453/92

to all of the ALEPH data for thrust from LEP. On the same plot, using the same model function, we show the contours for heavy jet mass. First of all, we observe that the flat direction exists in both of the data sets. We might have hoped that having two event shapes would remove the ambiguity, but this does not happen. Second, we see that while the perturbative fit has α_s lower for thrust than for heavy jet mass, with the power corrections, the value of α_s is higher for thrust, as found in previous studies [17,30]. However, when we perform a simultaneous fit to all of the thrust and heavy jet mass degrees of freedom, we get a value for α_s that is larger than each one separately. The best fit for thrust, heavy jet mass, and the combined fit are shown in Table 2.3. The fact that the thrust and heavy jet mass contours do not overlap indicate that a better handling of non-perturbative effects is required.

We conclude that neither correcting the theory curves with a Monte Carlo simulation nor using a minimal shape function approach for the leading power correction is satisfactory. The

shape function approach is improvable, while the Monte Carlo approach is limited by the perturbative accuracy of the parton shower, which will be limited to leading-log resummation in at least the near future (although SCET may eventually help go beyond LL [34, 35]). To improve the shape function fit, a number of additional ingredients should be included. First of all, the renormalon ambiguity in separating the perturbative and non-perturbative parts of the soft function should be removed. This is not likely to have much effect in the fit region we use, but will allow us to use data closer to the peak. Having more data involved will more highly constrain the fit and could remove the flat direction. To do this, we would need the bin-by-bin correlations among the experimental systematic uncertainties, which are not publicly available. In addition, there are perturbatively calculable effects we have not included, such as electroweak and m_b corrections, as in [14], which may have up to a 1% effect. It would be very interesting to see if the thrust and heavy jet mass distributions can be reconciled once a thorough effective field theory analysis, including non-perturbative effects, is performed.

2.1.5 Conclusions

In this paper, We have studied the heavy jet mass distribution using Soft-Collinear Effective Theory including $\mathrm{N^3LL}$ resummation and matching to the NNLO fixed order distribution. Up to this point, this kind of accuracy has only been available for the thrust distribution. Having an additional event shape helps control for systematic uncertainties, making the fit for α_s more trustworthy. It also gives us insight into power corrections and multi-scale soft functions which will be important for the LHC.

The heavy jet mass fit gives $\alpha_s(m_Z) = 0.1220 \pm 0.0031$. This value is larger than what had been found for thrust at the same accuracy, $\alpha_s(m_Z) = 0.1175 \pm 0.0026$. The uncertainty on heavy jet mass is larger partially due to a larger hadronization uncertainty. In our study, no corrections were made for hadronization. We explored the traditional method of hadronization, using Monte Carlo event generator, such as PYTHIA and concluded that such an approach is problematic for theoretical calculations of this accuracy. Since the Monte Carlo has been already tuned to the data we are trying to match, the tuning has partially compensated for resummation of subleading logarithms. Comparing PYTHIA's output in the fit region, the hadronized distribution is actually farther away from the data than the parton-level distribution.

Table 2.4: Best fit values for $\alpha_s(m_Z)$ at various orders in perturbation theory. The first three columns are our results, the last two which include a Monte Carlo based hadronization correction are from [17].

Order	N^3LL+NNLO	N^3LL+NLO	NNLO	NNLO [17]	NLL+NNLO [17]
hadronization	NO	NO	NO	YES	YES
Thrust	0.1175	0.1173	0.1262	0.1275	0.1266
Heavy Jet Mass	0.1220	0.1189	0.1265	0.1248	0.1211

Our α_s values from thrust and heavy jet mass contrast with the results of [17], which at NLL+NNLO accuracy derived $\alpha_s(m_Z) = 0.1266$ from thrust and $\alpha_s(m_Z) = 0.1211$ from heavy jet mass. A comparison of various fits to thrust and heavy jet mass using the same ALEPH data is shown in Table 2.4. The authors of [17] have observed that event shapes tend to belong to one of two classes. The first class, including thrust, tends to produce higher values of α_s than the second class, which includes heavy jet mass. These authors attributed the difference to better perturbative stability in the second class. We find, if anything, better perturbative stability for thrust. Instead, the reason for the systematic separation of α_s values in this study, and also in the NNLO study of [30], may have more to do with their use of a Monte Carlo simulation to correct for hadronization. A similar conclusion was reached in [36] which studied event shape moments. The values of α_s for the two classes must eventually be reconcilable, but there may be a physical reason why the power corrections for one class are larger than for the other. This is worth understanding more thoroughly, and may have implications for the LHC.

The alternative to using a Monte Carlo simulation for hadronization is to add a shape function contribution within the effective field theory. Our simple shape function study shows that the leading power tends to shift α_s from both heavy jet mass and from thrust to lower values, with the heavy jet mass shift of larger magnitude. This can help explain why the thrust α_s comes out lower than the heavy jet mass α_s in our study, and not in [17, 30]. However, we also found that the best fit over all the ALEPH data from 91.2 to 206 GeV for thrust was incompatible with the best fit from heavy jet mass, and that the flat direction between α_s and the non-perturbative parameter $\Lambda_{\rm NP}$ persists in both distributions.

To get the values of α_s extracted from thrust and heavy jet mass to agree may require including additional ingredients, which can be done within the effective field theory framework. For example, there is a calculable m_b correction which tends to bring α_s up at least for thrust [14]. Including every possible correction must produce the same value of α_s from thrust and heavy

jet mass, and it will be interesting to see precisely how this happens. Also, more data should be included. Using data for values of heavy jet mass and thrust closer to the peak will lead to a more constrained shape function fit, although it may require going beyond the leading power. In addition, using data from other LEP experiments and other experiments at lower center-of-mass energy can further test and constrain the event shapes.

However, it is not clear if all of the differences between thrust and heavy jet mass can be accounted for entirely within SCET. For example, there is the possibility that the difference between thrust and heavy jet mass has more to do with the way hadron masses are handled experimentally than from higher order power corrections. In [37], substantial differences in the form of power corrections among the E-scheme, p-scheme and decay-scheme were found. It may turn out that an ultra-precise α_s fit can only be made if the identity of all the hadrons is known, which may be possible for future measurements but is not available for existing data. More likely, the thrust and heavy jet mass distributions can be made to agree within SCET, but the uncertainty on α_s will ultimately be limited by a hadron-mass-scheme dependent uncertainty. In any case, once the ingredients discussed for thrust in [14] are applied to heavy jet mass, we will be able to extract a more precise lesson about the importance of power corrections. In addition to reducing the uncertainty from α_s and teaching us about power corrections, combining the insights from thrust and heavy jet mass will more generally pave the way for deeper understanding of relevant jet-based observables at the LHC.

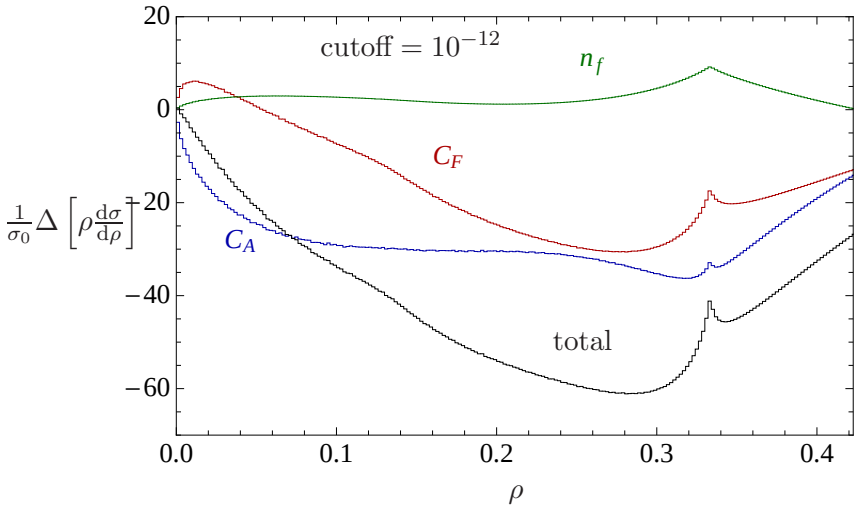

Figure 2.11: A comparison of the full fixed-order calculations and expanded SCET at NLO. Update of Figure 2.1 with cutoff $y = 10^{-12}$ in $B(\rho)$ from EVENT 2.

Note Added

After this manuscript appeared, it was suggested that the precision on $c_{2\rho}^S$ and c_2^S could be improved by lowering the infrared cutoff used by EVENT 2. The cutoff y is implemented by throwing out events if two partons have $(p_1 + p_2)^2 < yQ^2$. The default cutoff is 10^{-8}, and the authors of EVENT 2 caution about numerical instabilities if the cutoff is taken too low. We find that for cutoffs below 10^{-15}, there are insurmountable numerical problems, however $y = 10^{-12}$ seems to be convergent. We therefore ran 135 billion events with $y = 10^{-12}$ and 2500 bins ($\Delta\rho = 0.0002$)) – the main text uses 10 billion events with $y = 10^{-8}$ and 1000 bins ($\Delta\rho = 0.0005$). The difference between this new numerical data and the SCET prediction for the singular terms is shown in Figure 2.11, which is to be compared to Figure 2.1. One can see that the curves for all color structures now converge to zero, as expected.

Next, the constant $c_{2\rho}^S$ was extracted from these curves. The value $c_{2\rho}^S$ for various lower bounds $\rho_{\min}$ are shown in Figure 2.12. Again, improved numerical stability is clear. Fitting a sixth order polynomial to the 59 points between $\rho_{\min} = 0.0004$ and $\rho_{\min} = 0.012$ and extrapolating to $\rho_{\min} = 0$ leads to

$$c_{2\rho}^S = (49.1)C_F^2 + (-33.2)C_F C_A + (50.2)C_F T_F n_f\,. \tag{2.50}$$

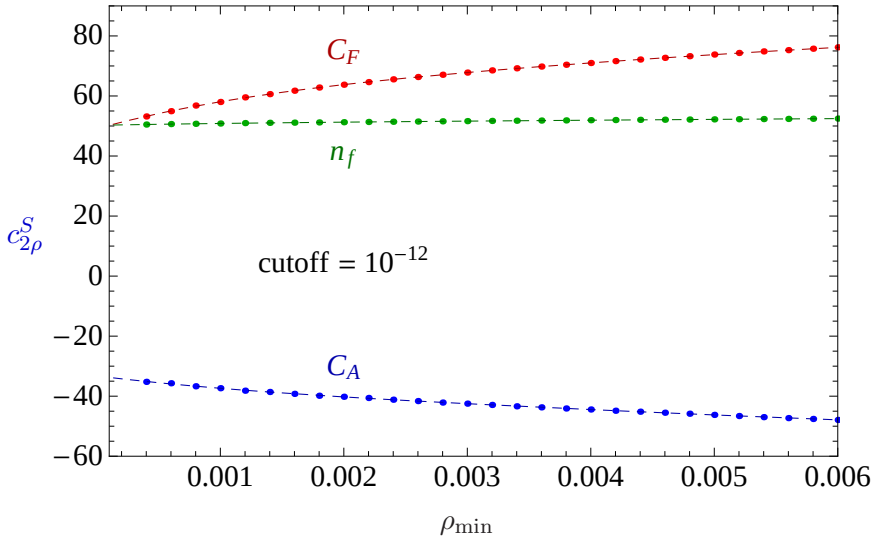

Figure 2.12: Extraction of the two-loop constants in the soft function. Update of Figure 2.2 with cutoff $y = 10^{-12}$ in $B(\rho)$ from EVENT 2.

The value of the C_F^2 coefficient is now consistent with the prediction of $\frac{\pi^4}{2} = 48.7$ from non-Abelian exponentiation. The fit is somewhat sensitive to the lower value of $\rho_{\min}$ used in the regression, but not very sensitive to the upper value. Fitting a fourth order polynomial to the 38 points between $\rho_{\min} = 0.0006$ and $\rho_{\min} = 0.008$ gives $c_{2\rho}^S = (49.8)C_F^2 + (-33.3)C_F C_A + (50.3)C_F T_F n_f$. Since the $C_F C_A$ and $C_F T_F n_f$ terms are practically unchanged, and the C_F^2 term is fixed by non-Abelian exponentiation, it is reasonable to assume that the remaining uncertainty on these numbers will have a negligible effect on the α_s fits. Performing the same analysis for thrust, leads to

$$c_2^S = (49.1)C_F^2 + (-57.8)C_F C_A + (43.4)C_F T_F n_f \tag{2.51}$$

Combining these, assuming the Hoang-Kluth Ansatz for the soft function, Eq. (2.30), gives

$$c_{2L}^S = (0)C_F^2 + (-7.5)C_F C_A + (-2.1)C_F T_F n_f \tag{2.52}$$

Thus, we take

$$c_2^S = \frac{\pi^4}{2}C_F^2 + (-57.8)C_F C_A + (43.4)C_F T_F n_f \tag{2.53}$$

$$c_{2L}^S = (0)C_F^2 + (-7.5)C_F C_A + (-2.1)C_F T_F n_f \tag{2.54}$$

With these more accurate numbers and a more accurate numerical calculation of the NNLO distribution, we can now repeat our comparison of the singular terms to the exact distribution. Using an infrared cutoff of 10^{-7} for the C functions, the agreement with the singular terms is improved. This can be seen in Figure 2.13, which is an update of Figure 2.3. Taking the difference between the curves gives Figure 2.14. One sees that the $1/N^2$ color structure, corresponding to C_F^3, has improved convergence towards zero. If these curves were known with perfect accuracy, they could be used to test the Ansatz in Eq. (2.30). The most poorly convergent color structures, $1/N^2$ and n_f^2 are not sensitive to this Ansatz, and the others are consistent with convergence to zero within the statistical uncertainty on the numerical NNLO calculation.

Finally, we reconsider the α_s fits in light of these more precise soft function coefficients and NLO matching functions. Refitting the thrust distribution to the ALEPH data changes $\alpha_s(m_Z)$ from 0.1175 to 0.1176 and refitting the heavy jet mass distribution raises $\alpha_s(m_Z)$ from 0.1220 to 0.1224. These shifts are within the quoted soft uncertainties.

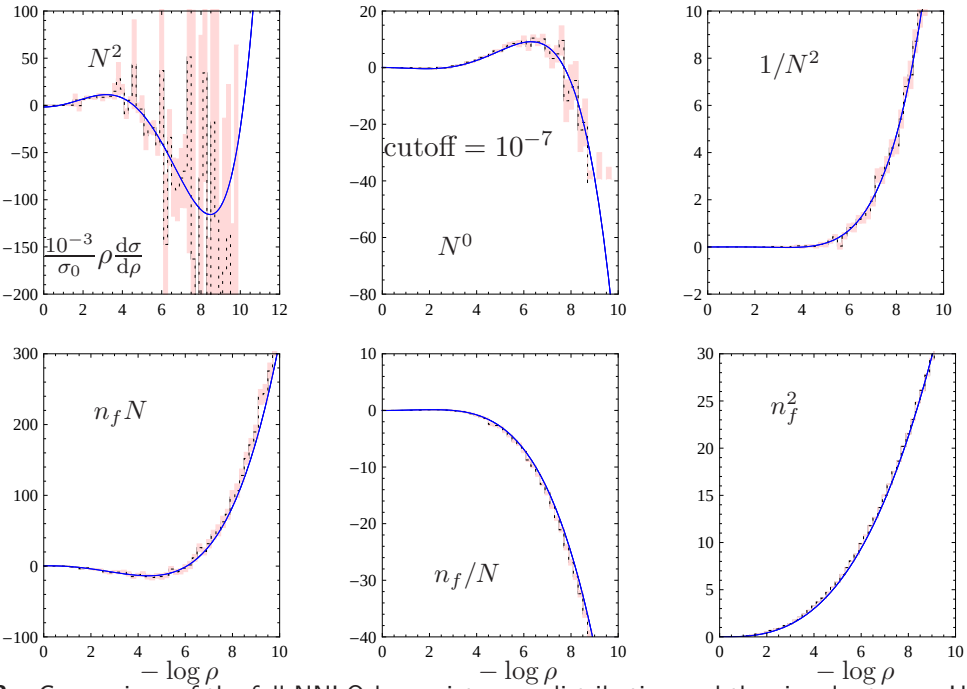

Figure 2.13: Comparison of the full NNLO heavy jet mass distribution and the singular terms. Update of Fig 2.3 with cutoff $y_0 = 10^{-7}$ in $C(\rho)$.

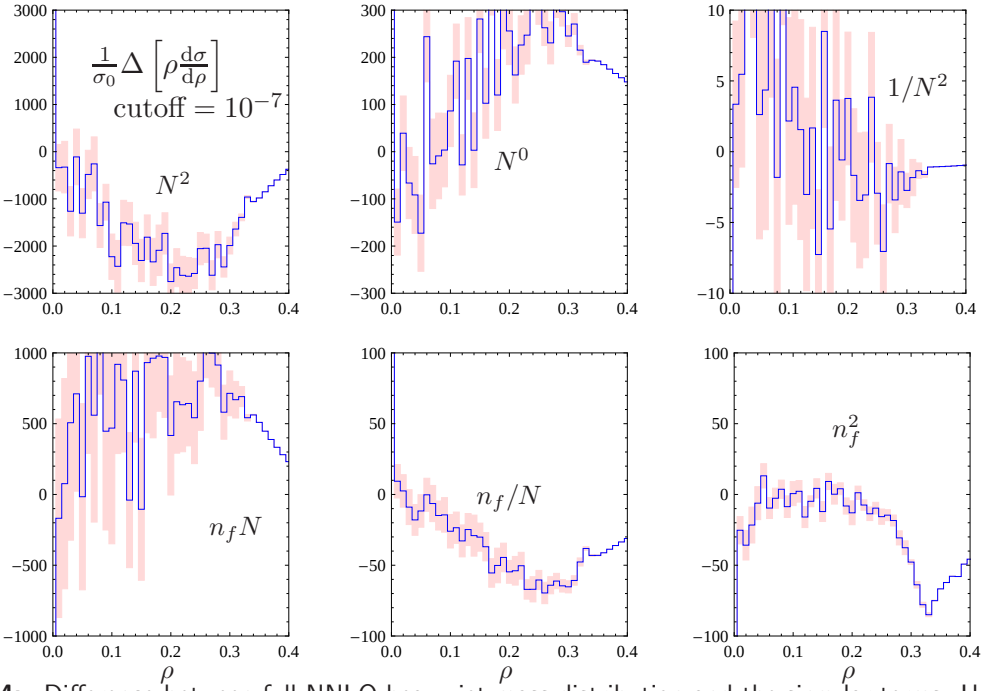

Figure 2.14: Difference between full NNLO heavy jet mass distribution and the singular terms. Update of Fig 2.4 with cutoff $y_0 = 10^{-7}$ in $C(\rho)$. The uncertainty on c_2^S and $c_{2\rho}^S$ is now negligible.

2.2 Resummation of Jet Mass at Hadron Colliders

The properties of jets produced at the Large Hadron Collider (LHC) have been coming into increased focus over the last few years, both from theoretical and experimental points of view. Jet properties can be used both to understand QCD and to find and discriminate among models of new physics. Indeed, many methods involving jet substructure have been developed over the last few years that can be used in new physics searches [38–50]. These studies are almost all based on Monte-Carlo simulations. As the precision of the experimental measurements improves, precision calculations beyond the level of current Monte-Carlo generators will become increasingly important. In this paper we provide a framework in which the simplest jet property, jet mass, can be computed in a systematically improvable way.

Precision QCD calculations of jet shapes, such as jet mass, are difficult for a number of reasons. Calculations at fixed order in perturbation theory are only useful at large values of jet mass in the tail of the distribution. Near the peak, large Sudakov double logarithms become increasingly important. The resummation of these logarithms is critical in achieving distributions with even qualitative agreement with data. However, the resummation of jet mass in a realistic hadronic collider environment is challenging due to the large number of variables: the jet size R, the jet algorithm, the beam remnants, the initial state radiation, hadronization, underlying event, etc.

There has been flurry of work on jet mass resummation over the last few years [11, 51–62]. In particular, it has been demonstrated that large logarithms of jet masses can be understood and in some cases resummed using effective field theory techniques. In this paper we consider the simplest QCD event shape, the jet invariant mass, and we focus on a very simple event topology: a jet produced in association with a hard photon. This process provides a natural setting to generalize similar work that has been done for e^+e^- colliders. Furthermore, such a simple final state allows us to explore issues such as dealing with the beam remnant and the jet size, before attempting to extend these results to more complicated multi-jet final states.

Many of the ingredients necessary for jet mass resummation in direct photon production have already been provided in previous work that calculated the direct photon p_T and rapidity distribution using threshold resummation [18]. For the p_T spectrum inclusive over the jet

properties, one can treat the jet as everything-but-the-photon. Since the beam remnants are included in the jet, the factorization formula in the inclusive case is particularly simple. In this paper, we want to calculate a cross section which is differential in the jet mass. Thus, we must separate the soft radiation into an in-jet region and an out-of-jet region, which leads to a modified factorization formula.

Although the jet mass distribution in this paper is calculated by expanding around the machine threshold limit, where the jet and photon have the maximum possible energy, the results will be accurate well away from threshold, at phenomenologically relevant values of the jet momentum, due to dynamical threshold enhancement [63–65]. Dynamical threshold enhancement works because of the extremely rapid fall-off of the parton distribution functions (PDFs) as momentum fractions approach unity. This fall off forces radiation in realistic events to have similar properties to radiation in events near threshold. In particular, the large logarithms associated with soft and collinear singularities are determined by an effective maximum energy, set by a parton threshold, rather than the hadronic threshold. The power of threshold resummation has been confirmed by direct comparison with data in many cases. Here, in the absence of direct photon jet mass data, we confirm it by comparing to PYTHIA [22].

When dealing with an exclusive observable such as the jet mass, one is forced to contend with multiple relevant scales: the hard scale of the partonic collision, the jet scale associated with collinear radiation in the jets, the factorization scale associated with collinear radiation in the beams, and various soft scales. Through the use of the soft-collinear effective field theory (SCET) [8, 9], each of these scales is associated with a function that accounts for the physics of each scale. The multiple soft scales are particularly troublesome to deal with because the factorization formula coming out of effective theory does not distinguish them: SCET gives you only one soft function, with multiple scales. Previous work on multi-scale soft functions in SCET has observed that, in the absence of an exact two loop soft function calculation, improved agreement with QCD can result from assuming a factorized soft function [57, 61]. In this paper, we make further progress in understanding this refactorization by taking inspiration from results on resummation in perturbative QCD.

Previous work on jet mass resummation in perturbative QCD, such as in [59, 62, 66] has approximated the jet as having only collinear radiation and soft-collinear radiation. These two

ingredients combine into an infrared finite object that is a type of jet function, but different from the jet function used in SCET. This simple approximation leads to good agreement with CDF data in [67] and indicates that the dominant large logarithmic corrections are contained in the collinear and soft-collinear sectors. To go beyond the leading-logarithmic accuracy of [59,62], we need to also include initial state radiation and color coherence effects. These are naturally part of the threshold calculation we provide here. We therefore factorize out of the full soft function a part associated with radiation which goes entirely into the jet, which has its own natural scale. We give a precise operator definition of this regional soft-function that, in particular, contains all the modes that are simultaneously soft and collinear to the jet. Thus our results will reduce to previous results at leading-logarithmic level, but are systematically improvable.

Our systematic improvements over previous work include the full next-to-next-to-leading logarithmic (NNLL) resummation of the global logarithms, including initial state radiation and color-coherence effects. One difficult unsolved problem in jet observables which are not completely inclusive is that of non-global logarithms (NGLs) [29, 68–70]. Although we have not succeeded in resuming NGLs in this work, and thus our distribution is only formally valid at the NLL level, our factorized soft function clarifies the role of the missing terms. In an related observable, jet thrust [57, 61], the anomalous dimension of the analogy of our regional soft function is proportional to the leading non-global logarithm. We use the correspondence to estimate the size of NGLs for jet mass by varying the appropriate coefficient in our expressions. The effect of non-global logarithms is significant in the peak region and must be understood better for further systematic improvements.

Because the factorization formula in SCET gives different objects with different associated scales, we can resum large logarithms by matching and running between these scales. It is an advantage of the effective theory approach that these scales are manifest throughout the calculation. Due to the convolution with the non-perturbative PDFs, scale choices cannot be made analytically. We therefore choose our scales numerically, following the approach of [65]. As emphasized in [71] and [72], it is an advantage of the effective theory approach that natural scales automatically appear through this numerical procedure, in contrast to fixed order calculations where they can only be guessed. Our results are compared to the output of PYTHIA [73], with very good agreement.

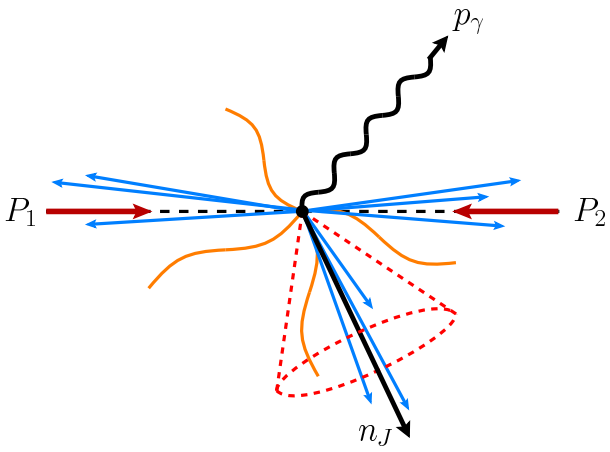

Figure 2.15: Event topology of direct photon production.

2.2.1 Kinematics and the Observable

In this section we briefly review some kinematics of direct photon production in a hadron collider and set up our notation. We will follow the conventions in [18], and we summarize the most important kinematic relationships. Once the kinematic variables are defined, we will define our jet definition and the specific observable that we calculate in this paper.

Hadronic and Partonic Kinematics

We will denote the momenta of the incoming hadrons as P_1^μ and P_2^μ, and the momentum of the photon as p_γ^μ. The observable will be categorized by the properties of the hard photon, namely its transverse momentum p_T and rapidity y. Formally, the results of this paper will be most accurate when p_T is near the *machine threshold* limit,

$$p_T \sim p_T^{\max} = \frac{E_{\rm CM}}{2\cosh y}\,, \tag{2.55}$$

where $E_{\rm CM} = \sqrt{(P_1+P_2)^2}$. A majority of events will have photon transverse momenta that are far below the machine threshold limit. However, as we will see, the calculation remains valid for transverse momenta much less than machine threshold due a phenomenon called dynamical threshold enhancement, discussed in Section 2.2.2.

A schematic showing the event topology for the collision is given in Figure 2.15. The hard

process involves the collision between two initial state partons, which have momentum $p_i^\mu = x_i P_i^\mu$, where the x_i is the momentum fraction of the constituent parton and the subscript denotes the hadron from which it came. There are two channels that are relevant at leading order in α_s, the annihilation channel, $q\overline{q} \to \gamma g$ and the Compton channel, $qg \to \gamma q$. It is convenient to use the variables w and v, given by

$$x_1 = \frac{1}{w}\frac{p_T}{E_{\rm CM} v} e^y \,, \qquad x_2 = \frac{p_T}{E_{\rm CM}(1-v)} e^{-y} \,. \tag{2.56}$$

The variable v is related to the scattering angle between the photon and the beam, θ^*, in the partonic center of mass frame through

$$v = \frac{1}{2}(1 + \cos\theta^*) \,. \tag{2.57}$$

The other variable w characterizes how much the (partonic) event deviates from exact $2 \to 2$ kinematics due to additional QCD radiation in the initial or final state. When $w = 1$, there is no additional radiation and the partonic final state consists of a photon and either a quark in the case of $qg \to q\gamma$ or a gluon in the case of $q\overline{q} \to g\gamma$.

When discussing the threshold limits, we will discuss the (total) hadronic invariant mass

$$M_X^2 = (P_1 + P_2 - p_\gamma)^2 \,, \tag{2.58}$$

and the (total) partonic invariant mass

$$m_X^2 = (x_1 P_1 + x_2 P_2 - p_\gamma)^2 \,. \tag{2.59}$$

These give the invariant mass of all particles in the final state with the photon's momentum removed from the hadronic or partonic final state, respectively. The hadronic variable M_X includes the beam remnant, whereas the partonic version does not have any information about the beam, and therefore $0 \leq m_X \leq M_X$. In terms of the momentum fractions of the partons

and the photon transverse momentum and rapidity, the invariant masses are

$$M_X^2 = E_{\rm CM}^2 - 2p_T E_{\rm CM} \cosh y = E_{\rm CM}^2 \left(1 - \frac{p_T}{p_T^{\rm max}}\right) \tag{2.60}$$

and

$$m_X^2 = \frac{p_T^2}{1-v}\frac{1-w}{w} \, . \tag{2.61}$$

In the partonic threshold limit, $w \to 1$, there is no phase space volume for the initial or final state radiation, and so the the final state consists of a single scattered parton and a photon. After removing the photon, only a massless parton remains and so the partonic mass vanishes in this limit ($m_X \to 0$). The partonic cross section is singular in this limit, and the resulting singularities take the form of $\ln^2 m_X \sim \ln^2(1-w)$. In the next section, we will introduce a factorization theorem for the partonic cross section, that will resum the logarithms of m_X that appear as $\alpha_s^n \ln^m(1-w)$ in the differential cross section.

The observable

The observable we consider is the invariant mass of the hardest jet in events with a high p_T photon. Rather than use one of the standard jet algorithms to define the jet mass, we use a simple definition in order to make the analytical calculations more tractable. The jet mass used in this paper is defined through the following procedure.

1. Remove the photon from the event record.

2. Cluster the event using the anti-k_T jet algorithm.

3. Select the jet with the hardest p_T, and find its 3-momentum $\mathbf{p}_J$. This defines the jet axis as $\hat{n}_J = \frac{\mathbf{p}_J}{|\mathbf{p}_J|}$.

4. Define m_R to be the invariant mass of all of the radiation that lies within a cone of half-angle R centered on $\hat{n}_J$.

The observable we consider is $\frac{{\rm d}\sigma}{{\rm d}m_R}$, within some range of p_T and rapidity for the jet and photon. Our calculation is not sensitive to the difference in p_T between the jet and the photon, so we put a cut only on the photon p_T, integrating inclusively over the p_T of the jet. For concreteness our

numerical results will have central photons ($y = 0$) with a given p_T, integrated over jet rapidities between -1 and 1.

Although our R differs from a usual collider R, which is defined in terms of rapidities and azimuthal angles, the difference is small for central jets that dominate at large p_T. Our method of calculation, and our factorization theorem, would also work for more standard jet algorithms, such as the k_T algorithm. However, most standard algorithms suffer from clustering effects [60, 74–77] which are not completely understood. Extending the results of this paper to more standard jet algorithms will be explored in future work.

To calculate the jet mass accurately in QCD, one would like the relevant events to come from the hard process we are considering, namely a single photon plus a single parton. However, generically, there can be contributions from events with a hard photon and 2 or 3 jets. The simplest way to ensure single jet kinematics is to use a p_T veto on the second hardest jet. This is easy to do experimentally or when using an event generator, but in QCD introducing a new scale makes the theoretical calculation significantly more complicated. In particular, non-global logarithms of the jet mass relative to the veto scale will be introduced. Although these non-global logarithms might be a small effect numerically, an advantage of the threshold resummation is that one does not have to introduce an extra scale. Instead, the scale is implicit in the out-of-jet soft radiation which is integrated over.

By expanding around the threshold limit and demanding large p_T for the photon, we can ensure that we are in the photon-plus-single-jet configuration without introducing a new veto scale. When the photon's p_T is on the order of the hard scattering scale, the radiation outside of the hardest jet must be soft, which prevents the formation of a second hard jet. By suitably restricting the photon p_T, the events will contain a single recoiling jet and we are safely in the regime where the factorization theorem is valid. To put it another way, the fact that dynamical threshold enhancement has been shown to work for the direct photon p_T distribution in [18] indicates that the single jet configuration dominates. To be clear, the threshold expansion does not obviate the need to deal with non-global logarithms, as you would with a jet veto, but it does avoid having to deal with an explicit scale.

At the partonic threshold limit, where the process only has one parton and a photon in the final state, the p_T and y of the photon constrains the scattering angle of the outgoing jet. To

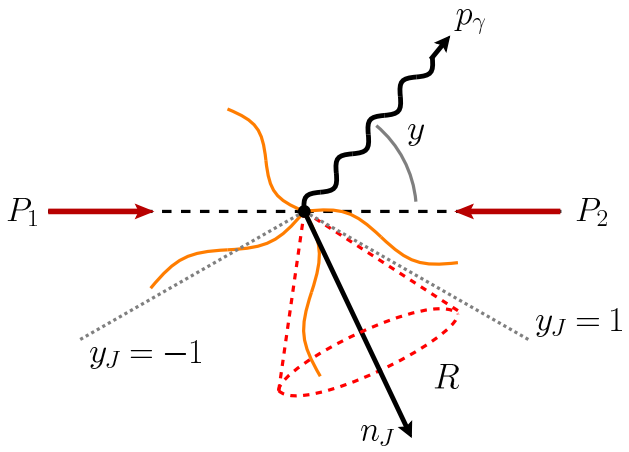

Figure 2.16: The photon's momentum and rapidity is denoted by p_γ and y, respectively. The jet cone of half angle R, centered around the direction of the jet $n_J = (1, \hat{n}_J)$. The restrictions on the jet rapidity y_J is shown by the dashed gray line. Soft radiation inside the jet contributes to $k_{\rm in} = n_J \cdot P_{X_s^{\rm in}}$, whereas the radiation outside contributes to $k_{\rm out} = n_J \cdot P_{X_s^{\rm out}}$

see this, consider momentum conservation along the direction of the beam, taken to be the z direction.

$$p_{Jz} = (x_1 P_1 + x_2 P_2 - p_\gamma)_z \tag{2.62}$$

After using the definition of rapidity, $y = \frac{1}{2} \ln \frac{E+p_z}{E-p_z}$, we can relate the rapidity of the jet y_J to the p_T and y of the photon and to $x_{1,2}$ via

$$\sinh y_J = \frac{E_{\rm CM}}{2p_T}(x_1 - x_2) - \sinh y \ , \tag{2.63}$$

Since $0 < x_{1,2} < 1$, y_J must lie within a range given by

$$-\frac{E_{\rm CM}}{2p_T} - \sinh y < \sinh y_J < \frac{E_{\rm CM}}{2p_T} - \sinh y \tag{2.64}$$

In order to perform threshold resummation, we must be careful to keep y_J small enough to ensure the jet does not enclose the beams. This restriction is $\sinh y_J < \cot R$, and so if we take $|y_J| < 1$, this implies that $R \lesssim 0.7$.

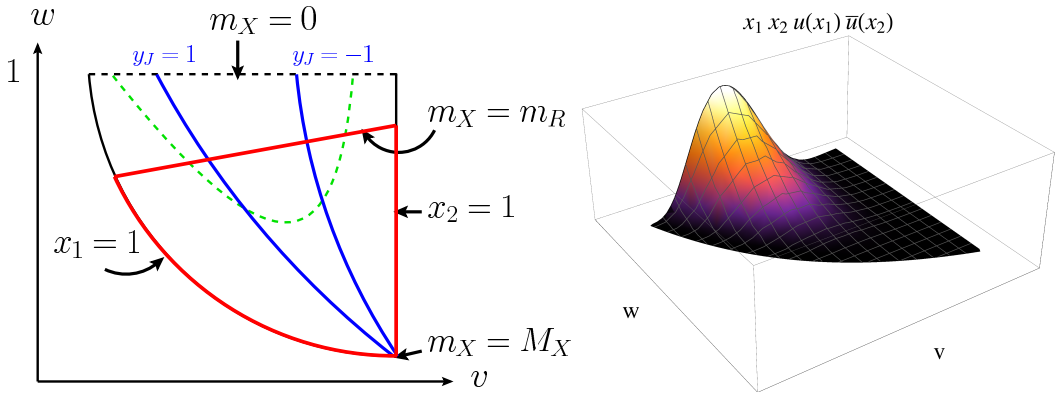

Figure 2.17: The integration region $\mathcal{R}$ is shown by the red lines. When the jet rapidity is restricted, the region is further constrained to be inside the blue lines, shown here for $y_{\rm cut} = 1$. The dashed green line outlines the region that most strongly contributes. This is demonstrated by the right hand plot, which shows the rapid fall off of $x_1 f_{u/P}(x_1) x_2 f_{\overline{u}/P}(x_2)$.

2.2.2 Differential Cross Sections and Factorization Theorem

The differential cross section for the process $N_1 + N_2 \to \gamma + X$ can be written in the form

$$\frac{\mathrm{d}^2\sigma}{\mathrm{d}p_T \mathrm{d}y \mathrm{d}m_R^2} = \frac{2}{p_T} \sum_{ab} \iint_{\mathcal{R}} \mathrm{d}v\mathrm{d}w \, \left[x_1 f_{a/N_1}(x_1,\mu)\right] \left[x_2 f_{b/N_2}(x_2,\mu)\right] \frac{\mathrm{d}^2\hat{\sigma}}{\mathrm{d}w\mathrm{d}v\mathrm{d}m_R^2} \,, \tag{2.65}$$

where N_i are the incoming partons, $f_{a/N_i}(x_i,\mu)$ is the probability distribution function for finding parton a in hadron N_i with momentum fraction x_i, and the sum is over the different partonic channels. The region of integration $\mathcal{R}$ in the $w-v$ plane is given by

$$\begin{aligned}
\frac{1 + m_R^2/p_T^2}{\frac{E_{\rm CM}}{p_T} e^{-y} + m_R^2/p_T^2} < \quad & v \quad < 1 - \frac{p_T}{E_{\rm CM}} e^{-y} \\
\frac{e^y}{v} \frac{p_T}{E_{\rm CM}} < \quad & w \quad < \frac{p_T^2}{p_T^2 + (1-v) m_R^2} \\
\frac{e^y}{v(2\sinh y + 2\sinh y_{\rm cut} + \frac{1}{1-v} e^{-y})} < \quad & w \quad < \frac{e^y}{v(2\sinh y - 2\sinh y_{\rm cut} + \frac{1}{1-v} e^{-y})} \,.
\end{aligned} \tag{2.66}$$

The first two constraints account for $0 \le x_i \le 1$ and $m_R^2 \le m_X^2$, which is the region enclosed by the red lines in Figure 2.17; the third constraint comes from a finite rapidity interval for the jet: $-y_{\rm cut} \le y_J \le y_{\rm cut}$, drawn as the blue lines in Figure 2.17. The expression $\frac{\mathrm{d}^2\hat{\sigma}}{\mathrm{d}w\mathrm{d}v\mathrm{d}m_R^2}$ gives the partonic cross section for $a + b \to \gamma + X$. For a fixed w and v, the partonic cross section, at NLO, will diverge logarithmically as $m_R \to 0$, and in this regime these logarithms can invalidate

an expansion in α_s.

The reason that the threshold expansion works away from threshold is that the parton distribution functions fall rapidly as the momentum fractions approach unity ($x_i \to 1$). In Eq. (2.69), the partonic differential cross section is weighted by the product of the PDFs. As a representative example, the right side of Figure 2.17 shows a plot of the product

$$x_1 f_{u/P}(x_1, \mu_f) x_2 f_{\overline{u}/P}(x_2, \mu_f) \,, \tag{2.67}$$

which would be necessary for process $u\overline{u} \to \gamma g$. In the plot, we have chosen $E_{\rm CM} = 8$ TeV, $p_T = 2$ TeV, $y = 0$, and $\mu_f = \sqrt{\hat{s}} = \sqrt{x_1 x_2} E_{\rm CM}$. The plot clearly shows the extremely rapid fall off of the PDFs, and this demonstrates that, for a fixed value of m_R, the region in $w - v$ space is weighted far more heavily along the line given by $m_X = m_R$.

The hadronic invariant mass can be written as

$$M_X^2 = \frac{m_X^2}{x_2} + E_{\rm CM}^2[(1 - x_1)v + (1 - x_2)(1 - v)] \,. \tag{2.68}$$

When $M_X \to 0$, this forces both $m_X \to 0$ and $x_{1,2} \to 1$; however, the fall off the PDFs favor small m_X even when x_i is not close to 1. Since $m_R < m_X$, this also means that small m_R is favored. The partonic cross section is singular in m_R, which manifests itself as powers of $\ln m_R$, and for small m_R, these logarithms are large and must be resummed. This enhancement of the singular region for the partonic cross section means that resummation of m_R is important, even when we are not near the machine threshold. This effect is known as dynamic threshold enhancement [63–65].

Factorization of the partonic cross section

When the jet invariant mass is small compared to the p_T, the jet is highly collimated and the process can be described within the framework of the Soft-Collinear Effective Theory (SCET) [8, 9, 78, 79]. Rather than give a formal derivation of the factorization formula as in [18], we will focus on how the factorization formula must be modified to become differential in the jet mass.

The partonic differential cross section can be calculated via

$$\frac{\mathrm{d}^2\hat{\sigma}}{\mathrm{d}w\mathrm{d}v\mathrm{d}m_R^2} = w\ \tilde{\sigma}(v)\ H(p_T, v, \mu) \int_0^{\frac{m_R^2}{2E_J}} \frac{\mathrm{d}k}{2E_J}\ J(m_R^2 - (2E_J)k, \mu)\ S(k, \frac{m_X^2 - m_R^2}{2E_J}, \mu)\ . \quad (2.69)$$

The three functions H, J and S are the hard, jet and soft functions, which account for the physics associated with the different scales involved. The quantity $\tilde{\sigma}(v)$ is defined through the leading order QCD result via,

$$\frac{\mathrm{d}^2\hat{\sigma}}{\mathrm{d}w\mathrm{d}v\mathrm{d}m_R^2} = \tilde{\sigma}_{ab}(v)\ \delta(m_R^2)\ \delta(m_X^2 - m_R^2)\ , \quad (2.70)$$

where the tree level parton cross sections are given by

$$\begin{aligned}\tilde{\sigma}_{q\overline{q}}(v) &= \pi\alpha_{\mathrm{em}}e_q^2\alpha_s(\mu)\frac{2C_F}{N_c}\left(\frac{v^2 + (1-v)^2}{1-v}\right)\\ \tilde{\sigma}_{qg}(v) &= \pi\alpha_{\mathrm{em}}e_q^2\alpha_s(\mu)\frac{1}{N_c}(1 + (1-v)^2)\frac{v}{1-v}\ .\end{aligned} \quad (2.71)$$

The hard function is given by the square of the Wilson coefficients that arise when matching the QCD amplitude onto the effective field theory operators. It describes the short distance physics at an energy scale $\mu_h \sim p_T$. The jet function comes from integrating energetic modes that are collinear to the jet direction that have virtuality comparable to m_R. In the threshold limit $m_R \ll p_T R$, so the collinear radiation is insensitive to the jet boundary. Thus we can use the same inclusive jet function as that in [18]. Finally, once the collinear modes are integrated out, we are left with the soft modes, which are described by soft Wilson lines. The soft function relevant for the jet mass calculation is different from the one used in [18]. As we will see, it depends separately on the radiation inside and outside of the jet, and also on the jet algorithm.

The form of the factorization theorem can be understood from power counting in the threshold region. In the partonic threshold limit, corresponding to the limit $m_X \to 0$, radiation is constrained either to be collinear to recoiling parton, which we call p_J^μ, or to be soft, which we write as k^μ. In terms of these momentum regions, the partonic invariant mass takes the form

$$m_X^2 = (p_J + k)^2 = m_c^2 + 2k \cdot p_J + \cdots \quad (2.72)$$

up to terms of order $k^2 \ll m_c^2$ where $m_c^2 = p_J^2$ is the collinear mass, whose distribution is given by the jet function.

The jet invariant mass m_R only contains the part of radiation inside the cone. Since all the collinear radiation is in the cone, we have only to split the soft radiation, which we write as $k^\mu = k_{\rm in}^\mu + k_{\rm out}^\mu$, with $k_{\rm in}^\mu$ in the cone and $k_{\rm out}^\mu$ out of the cone. Then,

$$m_R^2 = (p_J + k_{\rm in})^2 = m_c^2 + 2k_{\rm in} \cdot p_J \ . \tag{2.73}$$

and so

$$m_X^2 = m_R^2 + 2k_{\rm out} \cdot p_J \ . \tag{2.74}$$

Now, the jet momentum p_J^μ accounts for radiation that is collinear to recoiling parton, and so it can be written as

$$p_J^\mu = E_J n_J^\mu + \text{residual} \ . \tag{2.75}$$

where $n_J^\mu = (1, \hat{n}_J)$ is a lightlike vector that is directed along the jet direction. The residual momentum gives a power suppressed contribution to the jet mass compared to the leading component, and thus can be dropped. The expressions for m_X and m_R then become

$$\begin{aligned} m_X^2 &= m_R^2 + 2E_J(n_J \cdot k_{\rm out}) \\ m_R^2 &= m_c^2 + 2E_J(n_J \cdot k_{\rm in}) \ . \end{aligned} \tag{2.76}$$

Therefore, the only component that enters the soft function is $k \equiv n_J \cdot k$. These expressions explain the form of the factorization theorem, Eq.(2.69), which can be written as

$$\begin{aligned} \frac{{\rm d}^2\hat{\sigma}}{{\rm d}w{\rm d}v{\rm d}m_R^2} &= w\ \tilde{\sigma}(v)\ H(p_T, v, \mu) \int {\rm d}k_{\rm in}{\rm d}k_{\rm out}{\rm d}m^2 J(m^2) S(k_{\rm in}, k_{\rm out}) \\ &\quad \times \delta(m_R^2 - m^2 - 2E_J k_{\rm in}) \delta(m_X^2 - m_R^2 - 2E_J k_{\rm out}) \ . \end{aligned} \tag{2.77}$$

Furthermore, we see why we need a soft function that depends on the projection of the soft momentum on the jet direction separated into in-cone and out-of cone components, which we denote $k_{\rm in}$ and $k_{\rm out}$.

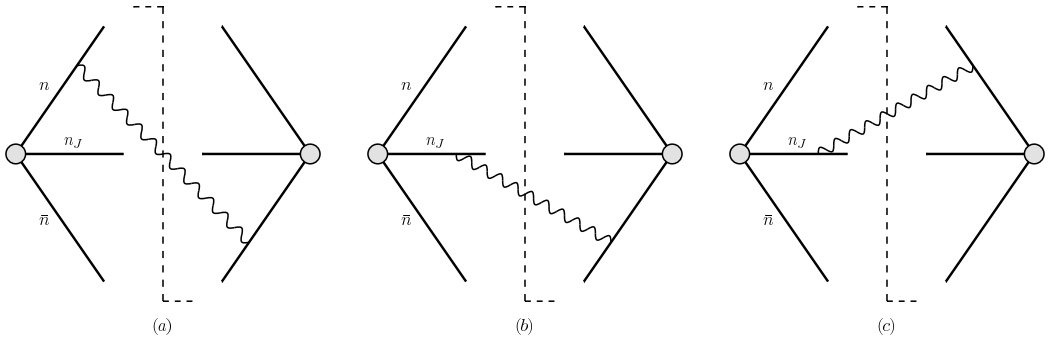

Figure 2.18: The non-vanishing diagrams that contribute to the one-loop soft function.

The precise definition of the soft function we need is, for annihilation channel,

$$S_{q\bar{q}}(k_{\rm in}, k_{\rm out}) = \frac{1}{C_F N_c} \sum_{X_s} |\langle X_s | \mathbf{T}\Big[Y_1^\dagger Y_J t^a Y_J^\dagger Y_2(0)\Big] |0\rangle|^2 \delta(n_J \cdot P_{X_s^{\rm in}} - k_{\rm in}) \delta(n_J \cdot P_{X_s^{\rm out}} - k_{\rm out}) \,, \tag{2.78}$$

and for Compton channel

$$S_{qg}(k_{\rm in}, k_{\rm out}) = \frac{1}{C_F N_c} \sum_{X_s} |\langle X_s | \mathbf{T}\Big[Y_1^\dagger Y_2 t^a Y_2^\dagger Y_J(0)\Big] |0\rangle|^2 \delta(n_J \cdot P_{X_s^{\rm in}} - k_{\rm in}) \delta(n_J \cdot P_{X_s^{\rm out}} - k_{\rm out}) \,, \tag{2.79}$$

where $P_{X_s^{\rm in}}$ and $P_{X_s^{\rm out}}$ denote the total momentum of the soft radiation propagating inside and outside the jet, respectively. Also, Y_i is a soft Wilson line directed along the $n_i = (1, \hat{n}_i)$ direction:

$$Y_i^\dagger(x) = P \exp\left(ig \int_0^\infty ds \; n_i \cdot A_s(n_i s + x) \right) \,, \tag{2.80}$$

where $i = 1, 2, J$ and P denotes path ordering and $A_s = A_s^a T^a$ are soft gauge fields in the fundamental representation.

One-loop soft function

We now calculate the required soft function to order α_s. The diagrams needed for the calculation are represented in Figure 2.18. The virtual diagrams are not shown as they give a scaleless contribution when using dimensional regularization to regulate both the ultraviolet and infra-

red divergences. The non-vanishing diagrams for the $q\overline{q} \to g\gamma$ channel give

$$S_{q\overline{q}}(k_{\rm in}, k_{\rm out}, \mu) = \frac{8\pi\alpha_s}{(2\pi)^{d-1}}\Big(\frac{\mu^2 e^{\gamma_E}}{4\pi}\Big)^{\epsilon}\int d^dq\ \delta(q^2)\theta(q_0)\mathcal{M}(k_{\rm in}, k_{\rm out}; q)$$
$$\times\Big[\Big(C_F - \frac{1}{2}C_A\Big)\frac{n_1\cdot n_2}{(n_1\cdot q)(n_2\cdot q)} + \frac{1}{2}C_A\frac{n_J\cdot n_1}{(n_J\cdot q)(n_1\cdot q)} + \frac{1}{2}C_A\frac{n_J\cdot n_2}{(n_J\cdot q)(n_2\cdot q)}\Big]\ , \quad (2.81)$$

where $q^+ = n_J\cdot q$, and $q^- = \overline{n}_J\cdot q$ with $\overline{n}_J = (1, -\hat{n}_J)$, and the measurement function is given by

$$\begin{aligned}\mathcal{M}(k_{\rm in}, k_{\rm out}; q) &= \Theta\Big(\frac{q^- - q^+}{q^- + q^+} - \cos R\Big)\delta(k_{\rm in} - q^+)\delta(k_{\rm out}) \\ &\quad +\Theta\Big(\cos R - \frac{q^- - q^+}{q^- + q^+}\Big)\delta(k_{\rm in})\delta(k_{\rm out} - q^+)\ . \end{aligned} \quad (2.82)$$

Similarly, for the $qg \to q\gamma$ channel we have

$$S_{qg}(k_{\rm in}, k_{\rm out}, \mu) = \frac{8\pi\alpha_s}{(2\pi)^{d-1}}\Big(\frac{\mu^2 e^{\gamma_E}}{4\pi}\Big)^{\epsilon}\int d^dq\ \delta(q^2)\theta(q_0)\mathcal{M}(k_{\rm in}, k_{\rm out}; q)$$
$$\times\Big[\frac{1}{2}C_A\frac{n_1\cdot n_2}{(n_1\cdot q)(n_2\cdot q)} + \Big(C_F - \frac{1}{2}C_A\Big)\frac{n_J\cdot n_1}{(n_J\cdot q)(n_1\cdot q)} + \frac{1}{2}C_A\frac{n_J\cdot n_2}{(n_J\cdot q)(n_2\cdot q)}\Big]. \quad (2.83)$$

The soft function will depend on the angle R and the rapidity of the jet y_J. For convenience we define

$$r = \tan\frac{R}{2} \qquad \beta = \exp(-y_J) \quad (2.84)$$

With these definitions, the soft functions associated with the two channels at order α_s are

$$\begin{aligned} S_{q\overline{q}}(k_{\rm in}, k_{\rm out}, \mu) &= \delta(k_{\rm in})\delta(k_{\rm out}) + 2\Big(\frac{\alpha_s}{4\pi}\Big)\Big\{\delta(k_{\rm in})\delta(k_{\rm out})\Big(C_F - \frac{1}{2}C_A\Big)\Big[\ln^2\frac{(1+\beta^2)^2}{\beta^2} - \frac{\pi^2}{6}\Big] \\ &+ 2\frac{\delta(k_{\rm out})}{k_{\rm in}}\Big[-2C_A\ln\Big(\frac{k_{\rm in}}{\mu}\frac{1+\beta^2}{\beta}\Big) + c_{q\overline{q}}\Big] \\ &+ 2\frac{\delta(k_{\rm in})}{k_{\rm out}}\Big[4C_F\ln\Big(\frac{k_{\rm out}}{\mu}\frac{1+\beta^2}{\beta}\Big) - c_{q\overline{q}}\Big]\Big\}\ , \end{aligned} \quad (2.85)$$

and

$$S_{qg}(k_{\rm in}, k_{\rm out}, \mu) = \delta(k_{\rm in})\delta(k_{\rm out}) + 2\Big(\frac{\alpha_s}{4\pi}\Big)\Big\{\delta(k_{\rm in})\delta(k_{\rm out})\Big(\frac{1}{2}C_A\Big)\Big[\ln^2\frac{(1+\beta^2)^2}{\beta^2} - \frac{\pi^2}{6}\Big]$$

$$
\begin{aligned}
&+ \quad 2\frac{\delta(k_{\rm out})}{k_{\rm in}}\Big[-2C_F \ln\Big(\frac{k_{\rm in}}{\mu}\frac{1+\beta^2}{\beta}\Big) + c_{qg}\Big] \\
&+ \quad 2\frac{\delta(k_{\rm in})}{k_{\rm out}}\Big[(2C_F+2C_A)\ln\Big(\frac{k_{\rm out}}{\mu}\frac{1+\beta^2}{\beta}\Big) - c_{qg}\Big]\Big\} \,, \qquad (2.86)
\end{aligned}
$$

where

$$
\begin{aligned}
c_{q\overline{q}} &= -C_F \ln\left[\frac{(\beta^2-r^2)(1-r^2\beta^2)}{\beta^2 r^4}\right] - C_A \ln\frac{\beta^2}{(1+\beta^2)^2} + (2C_F - C_A)\ln\frac{1+r^2}{r^2} \\
c_{qg} &= \Big[-C_F \ln\frac{\beta^2-r^2}{r^2\beta^2} - C_A \ln\frac{1-r^2\beta^2}{r^2\beta^2}\Big] - C_F \ln\frac{\beta^2}{(1+\beta^2)^2} + C_A \ln\frac{1+r^2}{r^2} \,. \qquad (2.87)
\end{aligned}
$$

The logarithmic divergences involving r and β arise when the jet cone encloses the collinear radiations from one of the incoming beams.

Since the factorization theorem contains convolutions between the jet and soft functions, it is easier to perform the calculation in Laplace space. The Laplace transformed soft function is defined as

$$
\tilde{s}(\kappa_{\rm in},\kappa_{\rm out},\mu) = \int_0^\infty dk_{\rm in}\int_0^\infty dk_{\rm out}\exp\Big(-\frac{k_{\rm in}}{\kappa_{\rm in}e^{\gamma_E}}\Big)\exp\Big(-\frac{k_{\rm out}}{\kappa_{\rm out}e^{\gamma_E}}\Big)S(k_{\rm in},k_{\rm out},\mu) \,. \qquad (2.88)
$$

Our result is then

$$
\begin{aligned}
\tilde{s}_{q\overline{q}}(L_1,L_2,\mu) &= 1+\Big(\frac{\alpha_s}{4\pi}\Big)\Big[4(2C_F L_2^2 - C_A L_1^2) + 4(L_1-L_2)c_{q\overline{q}} + \Big(C_F - \frac{1}{2}C_A\Big)\pi^2\Big] \\
\tilde{s}_{qg}(L_1,L_2,\mu) &= 1+\Big(\frac{\alpha_s}{4\pi}\Big)\Big[4((C_F+C_A)L_2^2 - C_F L_1^2) + 4(L_1-L_2)c_{qg} + \Big(\frac{1}{2}C_A\Big)\pi^2\Big] \,, \qquad (2.89)
\end{aligned}
$$

where $L_1 = \ln\left(\frac{1+\beta^2}{\beta}\frac{\kappa_{\rm in}}{\mu}\right)$ and $L_2 = \ln\left(\frac{1+\beta^2}{\beta}\frac{\kappa_{\rm out}}{\mu}\right)$.

The renormalization group equations satisfied by the soft function in the two channels are

$$
\begin{aligned}
\frac{d\tilde{s}_{q\overline{q}}}{d\ln\mu} &= \Big[2C_A\gamma_{\rm cusp}\ln\Big(\frac{1+\beta^2}{\beta}\frac{\kappa_{\rm in}}{\mu}\Big) - 4C_F\gamma_{\rm cusp}\ln\Big(\frac{1+\beta^2}{\beta}\frac{\kappa_{\rm out}}{\mu}\Big) - 2\gamma^{S_{q\overline{q}}}\Big]\tilde{s}_{q\overline{q}} \\
\frac{d\tilde{s}_{qg}}{d\ln\mu} &= \Big[2C_F\gamma_{\rm cusp}\ln\Big(\frac{1+\beta^2}{\beta}\frac{\kappa_{\rm in}}{\mu}\Big) - 2(C_F+C_A)\gamma_{\rm cusp}\ln\Big(\frac{1+\beta^2}{\beta}\frac{\kappa_{\rm out}}{\mu}\Big) - 2\gamma^{S_{qg}}\Big]\tilde{s}_{qg} \,. \qquad (2.90)
\end{aligned}
$$

where the expressions for $\gamma_{\rm cusp}$, $\gamma^{S_{q\overline{q}}}$, $\gamma^{S_{qg}}$ are given to order α_s^2 in [18] and are known to order α_s^3.

To check that the factorization theorem in Eq. (2.69) is correct, we have confirmed that the μ-dependence of the hard, jet, soft functions and PDFs near $x = 1$ cancel when combined. We also compare the singular part of the full QCD distribution at high p_T which we compute using the numerical package MCFM to the distribution produced by combining the hard, jet and soft functions at fixed order. This is shown in Figure 2.22.

Although the factorization theorem is correct, it does not automatically guarantee that we can resum all of the logarithms of m_R. Recall that the soft function in the factorization theorem in [18] was fully inclusive and had dependence only on the projection of the soft momentum in the jet direction. For the inclusive photon p_T spectrum, such a one-scale soft function is natural, since the observable only depends on a single scale, p_T. In contrast, the soft functions given in Eqs. (2.78) and (2.79) depend on two physical scales $k_{\rm in}, k_{\rm out}$ as well as on the renormalization scale μ. With multiple soft scales, there may not be a natural choice for μ, and therefore the renormalization group evolution may not resum all of the large logarithms. Indeed, in a analogous jet mass calculation for an e^+e^- collider, it was demonstrated first numerically in [57] and then analytically in [61] that the singularity structure of QCD was not completely reproduced by expanding the resummed result for jet thrust. One expects the same difficulty here.

The problem is that our soft function anomalous dimension does not depend on jet size R. This is simply because the hard and jet functions as well as the PDFs are the same as in the inclusive case and do not have a jet size dependence. However, there are large logarithms in full QCD that could only be predicted from an R-dependent anomalous dimension. To make this point more concrete, consider the singular part of the cross section calculated to $\mathcal{O}(\alpha_s)$ using SCET in the annihilation channel:

$$\frac{d\hat{\sigma}_{q\overline{q}}}{\mathrm{d}w\mathrm{d}v\mathrm{d}m_R^2} = w\tilde{\sigma}_{q\overline{q}}(v)\delta(m_X^2 - m_R^2)\frac{\alpha_s(\mu)}{4\pi}\frac{-2C_A\Gamma_0 \ln\frac{m_R^2}{p_T\mu} + c_{q\overline{q}}(r,\beta)\Gamma_0 + \Gamma_0^{J_g}\ln\frac{m_R^2}{\mu^2} + \gamma_0^{J_g}}{m_R^2} \quad (2.91)$$

Since SCET contains all of the singular contributions from full QCD, this will agree with the full one-loop QCD result expanded at small m_R. However, we should also be able to predict these

$\frac{1}{m_R^2}$ terms only using the anomalous dimensions, since they should be part of the resummation at NLL level. Since the coefficient of $\frac{1}{m_R^2}$ depends on $r = \tan R/2$ through the $c_{q\bar{q}}(r, \beta)$ term, this is impossible for R-independent anomalous dimensions. Thus, without further insight, resummation in SCET will undoubtedly miss these logarithmic corrections.

2.2.3 Refactorization of the Soft Function

The soft function depends on the two scales $k_{\rm in}$ and $k_{\rm out}$. By explicit calculation we found it has logarithmic dependence on both of the scales divided by μ already at one loop. Since there is not a single scale associated with the soft function, we should not expect that a single choice of μ will give the soft function a controlled perturbative expansion. In addition, at two loops, one generically expects a complicated dependence on $k_{\rm in}/k_{\rm out}$ in the soft function, as was found in [61, 80], representative of the non-global structure. The problem, from an effective theory point of view, is that there are two modes with different characteristic scaling described by the same object. Ideally, we could factorize the soft function into separate objects which depend only on $k_{\rm in}/\mu$ and $k_{\rm out}/\mu$. However, it does not appear that the soft function exactly factorizes in that way.

In the absence of a full refactorization, we will proceed in a conservative fashion following methods of traditional resummation [81–86]. To that end, we can at least isolate part of the soft function whose scaling we already know, namely the part associated with radiation that goes entirely into the jet, which will at least contain all of the soft-collinear divergences. To do so, we will define an auxiliary soft function that only depends on $k_{\rm in}$, reminiscent of eikonal jet functions in [81]. There are many ways to do this. A simple choice is to define the auxiliary soft function the same way we define the 2-scale soft function, but inclusive over the out-of-jet radiation. That is, we take

$$\mathbf{S}_{q\bar{q}}(k_{\rm in}) = \frac{1}{C_F N_c} \sum_{X_s} |\langle X_s | \mathbf{T}\Big[Y_1^\dagger Y_J t^a Y_J^\dagger Y_2(0)\Big]|0\rangle|^2 \delta(k_{\rm in} - n_J \cdot P_{X_s^{\rm in}}) \,, \tag{2.92}$$

for the annihilation channel, and similarly for the Compton channel. We call this a **regional soft function**. The regional soft function was deliberately chosen to have the same color structure as the original soft function.

At one-loop the regional soft function is given by Eqs. (2.81) and (2.83) with the measurement function replaced by

$$\mathcal{M}(k_{\rm in};q) \;=\; \Theta\Big(\frac{q^- - q^+}{q^- + q^+} - \cos R\Big)\delta(k_{\rm in} - q^+)\;. \tag{2.93}$$

At order α_s, we find

$$\begin{aligned}
\mathbf{S}_{q\overline{q}}(k_{\rm in},\mu) &= \delta(k_{\rm in}) + 2\Big(\frac{\alpha_s}{4\pi}\Big)\Big\{\delta(k_{\rm in})\Big(-\frac{1}{2}C_A\Big)\Big[\ln^2\frac{(1+\beta^2)^2}{\beta^2} - \frac{\pi^2}{6}\Big] \\
&+ 2\frac{1}{k_{\rm in}}\Big[-2C_A\ln\Big(\frac{k_{\rm in}}{\mu}\frac{1+\beta^2}{\beta}\Big) + c_{q\overline{q}}\Big]\,, \\
\mathbf{S}_{qg}(k_{\rm in},\mu) &= \delta(k_{\rm in}) + 2\Big(\frac{\alpha_s}{4\pi}\Big)\Big\{\delta(k_{\rm in})\Big(-\frac{1}{2}C_F\Big)\Big[\ln^2\frac{(1+\beta^2)^2}{\beta^2} - \frac{\pi^2}{6}\Big] \\
&+ 2\frac{1}{k_{\rm in}}\Big[-2C_F\ln\Big(\frac{k_{\rm in}}{\mu}\frac{1+\beta^2}{\beta}\Big) + c_{qg}\Big]\,,
\end{aligned} \tag{2.94}$$

where $c_{q\overline{q}}$ and c_{qg} are given in Eq. (2.87). The anomalous dimensions at order α_s, in Laplace space, are

$$\begin{aligned}
\frac{d}{d\ln\mu}\tilde{s}_{q\overline{q}}(\kappa_{\rm in},\mu) &= \frac{\alpha_s}{4\pi}\Big[2C_A\Gamma_0\ln\Big(\frac{1+\beta^2}{\beta}\frac{\kappa_{\rm in}}{\mu}\Big) - 4c_{q\overline{q}}(r,\beta)\Big]\tilde{s}_{q\overline{q}}(\kappa_{\rm in},\mu) \\
\frac{d}{d\ln\mu}\tilde{s}_{qg}(\kappa_{\rm in},\mu) &= \frac{\alpha_s}{4\pi}\Big[2C_F\Gamma_0\ln\Big(\frac{1+\beta^2}{\beta}\frac{\kappa_{\rm in}}{\mu}\Big) - 4c_{qg}(r,\beta)\Big]\tilde{s}_{qg}(\kappa_{\rm in},\mu)\;,
\end{aligned} \tag{2.95}$$

The dependence of the soft function on $k_{\rm out}$ is still encoded in the full soft function, so we define the **residual soft function** to be what remains after dividing the full soft function by the regional soft function.

$$S_r(k_{\rm in},k_{\rm out},\mu) = \frac{S(k_{\rm in},k_{\rm out},\mu)}{\mathbf{S}(k_{\rm in},\mu)} \tag{2.96}$$

At order α_s, the contribution from radiation going inside the jet is identical between the full soft function and the regional soft function. When the radiation goes outside of the jet, it contributes to $k_{\rm out}$ in the full contribution, however its contribution to the regional soft function vanishes since the integral is scaleless. Thus the residual soft function at order α_s only has $k_{\rm out}$ dependence:

$$S_{r\,q\overline{q}}(k_{\rm in},k_{\rm out},\mu) \;=\; \delta(k_{\rm out}) + 2\Big(\frac{\alpha_s}{4\pi}\Big)\Big\{\delta(k_{\rm out})\Big(C_F\Big)\Big[\ln^2\frac{(1+\beta^2)^2}{\beta^2} - \frac{\pi^2}{6}\Big]$$

$$
\begin{aligned}
&+ \quad 2\frac{1}{k_{\rm out}}\Big[4C_F\ln\Big(\frac{k_{\rm out}}{\mu}\frac{1+\beta^2}{\beta}\Big) - c_{q\overline{q}}\Big]\Big\} \\
S_{rqg}(k_{\rm in}, k_{\rm out}, \mu) &= \delta(k_{\rm out}) + 2\Big(\frac{\alpha_s}{4\pi}\Big)\Big\{\delta(k_{\rm out})\Big(\frac{1}{2}C_F + \frac{1}{2}C_A\Big)\Big[\ln^2\frac{(1+\beta^2)^2}{\beta^2} - \frac{\pi^2}{6}\Big] \\
&+ \quad +2\frac{1}{k_{\rm out}}\Big[(2C_F + 2C_A)\ln\Big(\frac{k_{\rm out}}{\mu}\frac{1+\beta^2}{\beta}\Big) - c_{qg}\Big]\Big\}\,. \qquad (2.97)
\end{aligned}
$$

Thus, the one-loop anomalous dimensions of the residual soft function depends only on the Laplace conjugate variable for $k_{\rm out}$, $\kappa_{\rm out}$:

$$
\begin{aligned}
\frac{d}{d\ln\mu}\tilde{s}_{rq\overline{q}}(\kappa_{\rm out}, \mu) &= \frac{\alpha_s}{4\pi}\Big[-4C_F\Gamma_0\ln\left(\frac{1+\beta^2}{\beta}\frac{\kappa_{\rm out}}{\mu}\right) + 4c_{q\overline{q}}(r,\beta)\Big]\tilde{s}_{rq\overline{q}}(\kappa_{\rm out}, \mu) \\
\frac{d}{d\ln\mu}\tilde{s}_{rqg}(\kappa_{\rm out}, \mu) &= \frac{\alpha_s}{4\pi}\Big[-2(C_F + C_A)\Gamma_0\ln\left(\frac{1+\beta^2}{\beta}\frac{\kappa_{\rm out}}{\mu}\right) + 4c_{qg}(r,\beta)\Big]\tilde{s}_{rqg}(\kappa_{\rm out}, \mu)\,, \qquad (2.98)
\end{aligned}
$$

Combining these results, we see that we have actually factorized the soft function at one-loop, since the regional and residual soft functions each depend on only one scale. At two-loops and higher, the regional soft function will still only depend on $k_{\rm in}$, however the residual soft function will have both $k_{\rm in}$ and $k_{\rm out}$ dependence. Thus, at least there should be a natural scale which minimizes the large logarithms in $\mathbf{S}(k_{\rm in}, \mu)$. In particular, this scale should correspond to the "see-saw" scale $\mu_s = \mu_j^2/\mu_h$ for the soft radiation associated with a particular collinear direction [6]. Such a scale assignment is implicit in much of the work on traditional resummation, and here we have made it explicit using SCET.

For this refactorization to make any difference, we have to allow the residual soft function scale to be different from the scale for the regional soft function. So we write

$$
S(k_{\rm in}, k_{\rm out}, \mu) = \hat{\Pi}(\mu, \mu_{\rm in})\mathbf{S}(k_{\rm in}, \mu_{\rm in})\Pi_r(\mu, \mu_{\rm out})S_r(k_{\rm in}, k_{\rm out}, \mu_{\rm out}) \qquad (2.99)
$$

where the evolution kernels $\hat{\Pi}(\mu, \mu_{\rm in})$ and $\Pi_r(\mu, \mu_{\rm out})$ evolve their respective soft functions from μ to separate scales. In Sec. 2.2.5, we investigate how choosing two soft scales affects the jet mass distribution by comparing the calculation with and without such a scale separation (see Figure 2.23).

Unfortunately, since the residual soft function will depend on both $k_{\rm in}$ and $k_{\rm out}$ beyond

one-loop, our refactorization is only approximate. At two-loops, the $k_{\rm in}/k_{\rm out}$ dependence of the residual soft function is due to non-global structure. When the scales are widely separated, $k_{\rm in} \ll k_{\rm out}$ or vice verse, the non-global structure takes the form of a logarithm of the ratio of these scales. There have been many studies of non-global logarithms (NGLs) [29, 55, 60, 61, 68–70, 80, 87]. We will not attempt to calculate the non-global structure for this observable, which would require a two-loop calculation, instead we will estimate their effects and discuss their phenomenological significance in Sec. 2.2.6.

Comparing with pQCD result

Calculating the jet mass distribution at hadron collider has been done by using traditional pQCD resummation technique [59, 62, 88]. It's interesting to compare the pQCD results and the SCET results obtained in this paper. In Refs. [59, 62], the jet mass distribution is described by a process independent quark or gluon jet function, depending on the partonic origin of the jet. These pQCD jet functions are calculated to $\mathcal{O}(\alpha_s)$ explicitly, and resumed to all orders at NLL level by solving an evolution equation in Mellin space. In their approach, both the hard-collinear mode and soft mode contribute to the jet function, in contrast to the SCET approach, where jet function is defined with zero-bin subtraction [89]. Furthermore, the jet function defined in Refs. [59, 62] is independent of underlying partonic process, and the corresponding jet mass distribution misses the contribution from soft large angle radiation between different colored partons. Therefore a simple connection between their jet function and our SCET results can not be made.

To make progress comparing the different formalisms, it is helpful to consider the $R \to 0$ limit. In this limit, a process independent combination of jet and soft function can be defined in SCET. For example, for the annihilation channel, we have

$$J_g^{SCET}(m_R^2, \mu) = \lim_{R\to 0} \int dp^2 dk_{\rm in}\, J_g(p^2, \mu) S_{q\bar{q}}(k_{\rm in}, \mu) \delta(m_R^2 - p^2 - 2E_J k_{\rm in}), \tag{2.100}$$

and similarly for the Compton channel. The fact that in the $R \to 0$ limit $S_{q\bar{q}}$ depends only on the parton that initiates the jet can be seen explicitly by taking the limit in Eq. (2.94). In this limit, only the terms proportional to $\ln r$ survive, each of which is proportional the jet's Casimir

– C_F for quark jet and C_A for a gluon jet. Alternatively, it can be understood by the rescaling argument from [61]. To be specific, by rescaling R to $\pi/2$, the cone of the $\hat{n}_J$-jet becomes a hemisphere. At the same time, all other Wilson lines, except the one along the jet direction, are forced to point in the direction of $-\hat{n}_J$. Therefore, a soft dipole contribution from partons i and J, where i denotes an initial state parton, is identical to the hemisphere soft function [61], with the color factor replaced by $-T_i \cdot T_J$ in the color generator notation [27], while dipoles contributes from two initial state partons i and j vanish. Since $(-T_1 \cdot T_J - T_2 \cdot T_J) = T_J^2$, summation over different soft dipole gives a result which depends only on the jet direction and its color content. This explains why the jet function constructed in Eq. (2.100) depends only on the parton that initiates the jet. Indeed, at $\mathcal{O}(\alpha_s)$, for quark and gluon jet, we have

$$\begin{aligned} J_q^{SCET}(m_R^2, \mu) &= \frac{\alpha_s(\mu) C_F}{\pi m_R^2} \left(\log \frac{4E_J^2 \sin^2 \frac{R}{2}}{p_T^2} - \frac{3}{4} \right), \\ J_g^{SCET}(m_R^2, \mu) &= \frac{\alpha_s(\mu)}{\pi m_R^2} \left(C_A \log \frac{4E_J^2 \sin^2 \frac{R}{2}}{p_T^2} - \frac{11}{12} C_A + \frac{1}{3} n_f T_F \right), \end{aligned} \tag{2.101}$$

respectively, where n_f is the number of light flavor and $T_F = 1/2$ in QCD. Eq. (2.101) agrees with the corresponding $\mathcal{O}(\alpha_s)$ jet function in Eqs. (A3) and (A4) of Refs. [62], after power expanding in jet mass, except the term proportional to $n_f T_F$, which is missing there. From the discussion above, we see that the results presented in Refs. [59,62] are not complete at NLL level, missing the contribution from large angle soft cross talk, as well as the term proportional to $n_f T_F$ in the gluon jet function. These extra global NLL contributions are taken into account in a more recent work [88], which also includes a numerical exponentiation of part of the non-global structure.

2.2.4 Scale Choices

While the resummed result is formally independent of the scales μ_h, μ_j, $\mu_{\rm in}$ and $\mu_{\rm out}$ as well as the factorization scale we call μ, there is residual higher-order dependence on these scales if the perturbative expansions of the hard, jet and soft functions are truncated at a finite order. To get a well behaved expansion with minimum hard, jet and soft scale dependence, we want to evaluate each contribution at its natural scale where each function does not involve large

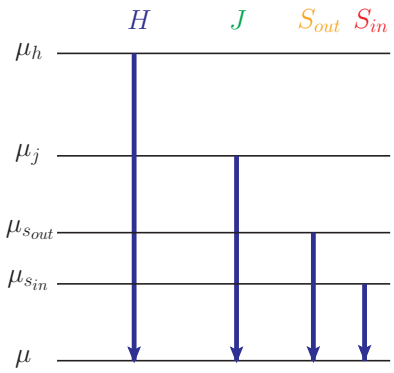

Figure 2.19: The renormalization group evolution of the hard, jet and soft functions, as shown schematically. Each function is calculated at fixed order at its natural scale, and they are evolved to a common scale μ. Two scales emerge in the soft sector which results in the refactorization of the soft function.

perturbative logarithms. We evolve the hard, jet and soft functions from their natural scales to the factorization scale μ as shown in Figure 2.19.

In the resummed distribution, the following ratios of scales appear

$$\frac{p_T^2}{\mu_h^2}\,, \qquad \frac{m_R^2}{\mu_j^2}\,, \qquad \frac{\mu_j^2}{p_T \mu_{\rm in}}\,, \qquad \frac{m_X^2 - m_R^2}{p_T \mu_{\rm out}}\,. \tag{2.102}$$

Unlike the fully inclusive case studied in [18], it would be impossible to minimize logarithms of these ratios with only 3 scales μ_h, μ_j and $\mu_s = \mu_{\rm in} = \mu_{\rm out}$. Instead, we will allow $\mu_{\rm in}$ and $\mu_{\rm out}$ to be independent, as explained in Sec. 2.2.3. When we choose a single soft scale, the resummed SCET distribution is hopelessly different from the PYTHIA output – this is shown in Figure 2.23.

The naive scale choices are

$$\mu_h = p_T\,, \qquad \mu_j = m_R\,, \qquad \mu_{\rm in} = \frac{m_R^2}{p_T}\,, \qquad \mu_{\rm out} = \frac{m_X^2 - m_R^2}{p_T}\,, \tag{2.103}$$

These would eliminate the large logarithms at each energy scale at the partonic level. However, when the partonic cross section is integrated against the PDFs, $\mu_{\rm out}$ will get arbitrarily close to zero and hit the Landau pole singularity of the running coupling. The problem is that the natural $\mu_{\rm out}$ scale choice depends on an unphysical quantity, namely $m_X^2 - m_R^2$. We can avoid the Landau pole and minimize the effects of the large logarithms by instead choosing the scales numerically to depend only on observables [65]. In fact, it is not necessary to eliminate the

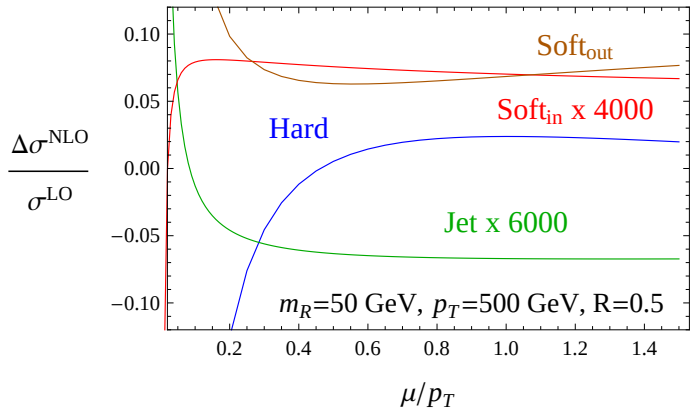

Figure 2.20: The NLO corrections of the hard, jet and soft functions to the jet mass distribution as a function of the renormalization scale for $m_R = 50$ GeV and $p_T = 500$ GeV . The natural scale of each mode is indicated by the of the extremum of the appropriate curve. The hard and soft_{out} scales do not depend on the mass of the jet; they are determined by varying the scales with the NLO delta function contributions. The jet and soft_{in} scales are determined by varying the scales with the NLO jet mass distribution. The jet and soft_{in} curves are scaled up to plot with the ones for the hard and soft_{out}.

logarithms in the unphysical, partonic cross section, but rather we want to eliminate the large logarithm in the physical, hadronic cross section.

To determine the natural RG scales, we follow the approach used in [18, 65, 71, 72]. We include separately the NLO corrections for the hard, jet or soft functions and vary the relevant scale to find out which scale minimizes the variation of the NLO distribution. For example, Figure 2.20 shows these NLO corrections for the 8 TeV LHC with a $p_T = 500$ GeV photon and $m_R = 50$ GeV. The extrema of these curves indicate a natural scale for each mode, and one can see that there is a natural hierarchy of the various matching scales. The jet and soft_{in} scales are jet mass dependent, whereas the hard and soft_{out} scales are jet mass independent (their NLO contributions have no dependence on m_R). We fit the jet mass dependence by power law curves, examples of which are shown in Figure 2.21 for different jet sizes. For example, with $R = 0.5$, the scale choice we extract are

$$\mu_h = p_T;, \qquad \mu_j = 1.6\ m_R^{1.47}\ , \qquad \mu_{\text{in}} = \frac{\mu_j^2}{6700}\ , \qquad \mu_{\text{out}} = 280\ \text{GeV}. \tag{2.104}$$

We choose the factorization scale to match the hard scale, $\mu = \mu_h$ (a high factorization scale is not natural in SCET, however it corresponds most closely to the scales where the PDFs have been fit). The renormalization group is then used to run between these scales to producing the

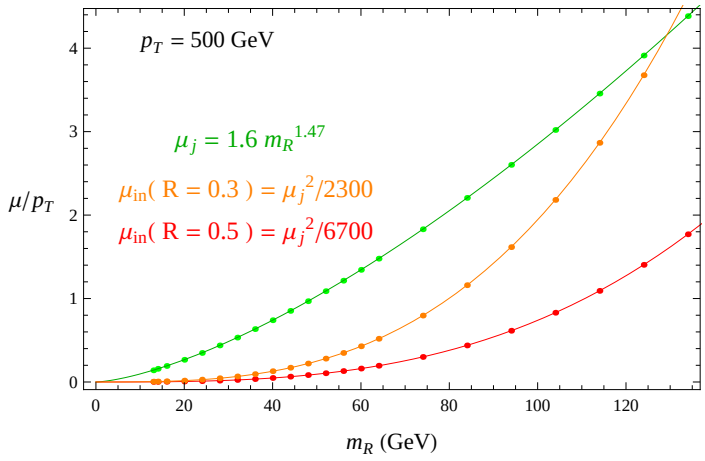

Figure 2.21: The jet and soft_{in} scales as a function of m_R for $p_T = 500$ GeV with two different cone sizes. Dots are extrema and curves are our fits. Note that μ_{in} is cone size dependent and increases when the cone gets smaller. However, μ_j^2/μ_{in} is m_R independent, which is a manifestation of the factorization theorem. The numerically determined jet and soft_{in} scales fit nicely with power law curves (m_R in GeV): $\mu_j = 1.6\ m_R^{1.47}$, $\mu_{\text{in}}(R = 0.3) = \mu_j^2/2300$, $\mu_{\text{in}}(R = 0.5) = \mu_j^2/6700$, and they are considerably higher than the naive choices of $\mu_j = m_R$ and $\mu_{\text{in}} = m_R^2/p_T$.

resummed jet mass distribution. For simplicity, we extract these curves at fixed p_T and y for the photon, although one could easily repeat this exercise integrated over some window of photon kinematics.

2.2.5 Results

To test our predictions, we compare our results to the output from PYTHIA 8 [73] for the LHC at $E_{\text{CM}} = 8$ TeV. We use the MSTW 2008 NLO PDFs [90] both for event generation and theory calculation. The event generation is made with the hadronization turned off, except for one curve on the right hand side of Figure 2.23, where you can see that it affects the peak region. For the rest of plots, we keep the initial state and final state radiation, but we turn off hadronization, underlying event and multiple interactions. These additional effects are important, but we postpone their consideration to future work. The specific observable we use is outlined in Section 2.2.1, and we test several values of R. The jet mass distribution is calculated and compared to PYTHIA in a small window of the photon transverse momentum and rapidity $(\Delta p_T, \Delta y) = (10\ \text{GeV}, 0.1)$, centered around $p_T = 500$ or 2000 GeV and $y = 0$, for various sizes of R.

Since SCET contains all the physics in the small m_R regime, it should reproduce the singular

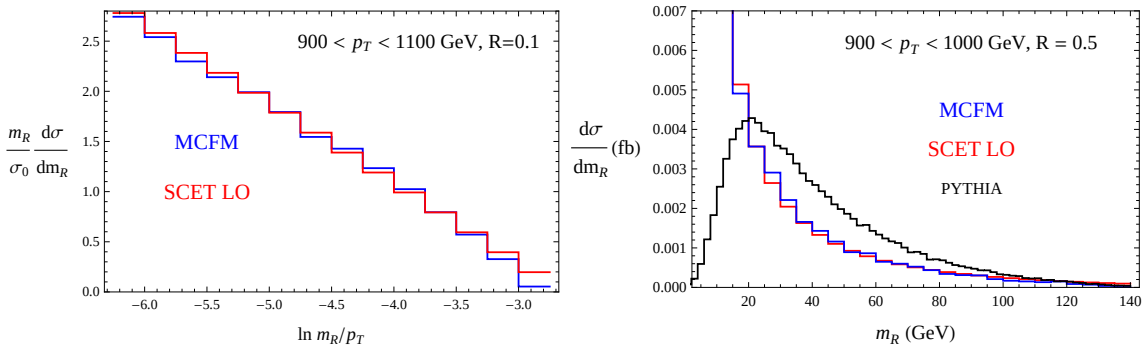

Figure 2.22: The left panel shows a comparison of the leading order jet mass distirbution calculated with MCFM and the prediction from expanding the resummed result to leading order (SCET LO). This demonstrates that SCET reproduces the singularities of QCD at leading order. The right panel compares MCFM and SCET to PYTHIA, with obvious disagreement, indicating the importance of resummation.

structure of full QCD at leading order. We check this by comparing the fixed order expansion of SCET to the exact leading order distribution, using MCFM [91], in the far singular region. The result is shown in Figure 2.22, which shows very good agreement down to very small m_R. We also compare MCFM with PYTHIA, and there is no region of m_R in which the QCD NLO calculation agrees, which suggests the necessity of resummation.

We calculate the jet mass distribution at full next-to-leading log (NLL) precision, which involves the two-loop cusp anomalous dimension and the one loop anomalous dimensions of the hard, jet and soft functions. In fact, all ingredients are known for NNLL resummation, except for the contribution of non-global logarithms. We estimate the effect of these missing NGLs in Sec. 2.2.6. We denote the partial next-to-next-to-leading log resummed result as NNLL_p, which has the three loop cusp anomalous dimension and the two-loop anomalous dimensions of the hard, jet and full soft functions. We have only included those parts of the $\mathcal{O}(\alpha_s^2)$ soft anomalous dimension that can be extracted from the RG invariance of the cross section, which does not include the angle-dependent pieces.

Figure 2.23 shows the jet mass distributions for the $p_T = 500$ GeV events at different orders of precision. For this p_T, we compute the jet mass distribution with a maximum cone size of $R = 0.5$ to avoid the jet being contaminated by the beam. We normalize the SCET distributions with the NLO QCD cross section as determined by PYTHIA 8, scaled by the QCD NLO K-factor for the cross-section with the jet rapidity restriction ($K \sim 0.8$ for a 500 GeV photon), which we compute with our own code. We do not match to the exact LO QCD calculation which

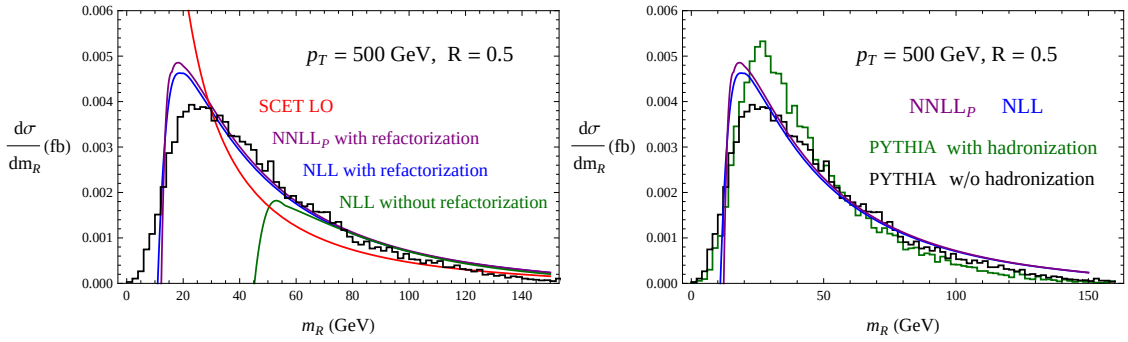

Figure 2.23: Comparison of the jet mass distributions with different orders of precision (curves) for $p_T = 500$ GeV and $R = 0.5$ to PYTHIA (histograms). The right plot shows the effects of hadronization in PYTHIA as compared to resummed distributions.

would account the power corrections in the tail. In the peak region, where most of the events lie, these power corrections are small. The scale uncertainties for the resummed result include variation of the factorization scale $\mu_f = \mu$, the hard scale μ_h, the jet scale μ_j, and the soft scales $\mu_{\rm in}$ and $\mu_{\rm out}$, Figure 2.24 shows the uncertainty bands for separate variation of the scales between $\frac{1}{2}\mu_i < \mu < 2\mu_i$ for $i = f, h, j, s_{\rm in}, s_{\rm out}$, for $p_T = 500$ GeV and $R = 0.5$ jets. Additional comparisons for $p_T = 2$ TeV and $R = 0.4$ are shown in Figures 2.25 and 2.26. The higher the transverse momentum of the photon, the closer to threshold, so we expect that threshold resummation will be more effective in this case.

2.2.6 The Role of Non-Global Logarithms

As mentioned in Section 2.2.3, although we were able to refactorize the soft function into a soft-collinear part, whose natural scale is associated with the soft modes within the jet, the remainder soft function still depended on multiple scales $S_r = S_r(k_{\rm in}, k_{\rm out}, \mu)$. Thus we cannot guarantee that all large logarithms in the jet mass distribution are resummed. The residual dependence of the remainder soft function on two scales is the problem of non-global structure. In the absence of a complete understanding of non-global structure, and how the non-global logs (NGLs) might be resummed, we will content ourselves with an estimate of how non-global structure might affect the jet mass distribution. We start by drawing on the lessons learned when considering $e^+e^- \to$ dijets, where there have been several studies [55, 60, 61, 80, 87].

A two-loop calculation of the soft function for hemispherical jets was performed in [80, 87] and for cone or anti-k_T jets, with an out-of-jet veto, in [61]. An intriguing observation from these

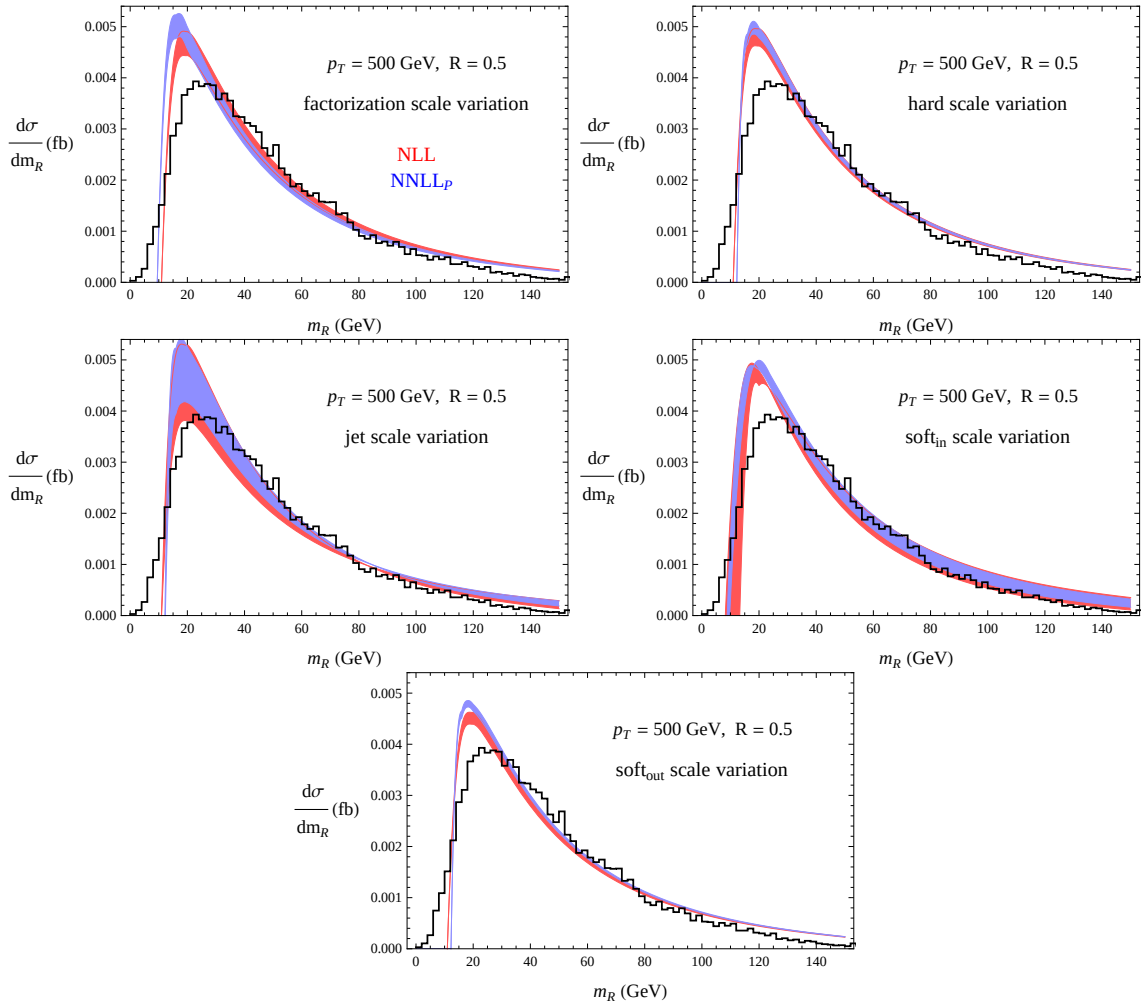

Figure 2.24: Scale uncertainties for $p_T = 500$ GeV and $R = 0.5$. The red bands are NLL and the blue bands are $\mathrm{NNLL_p}$. The PYTHIA result is the histogram shown in black.

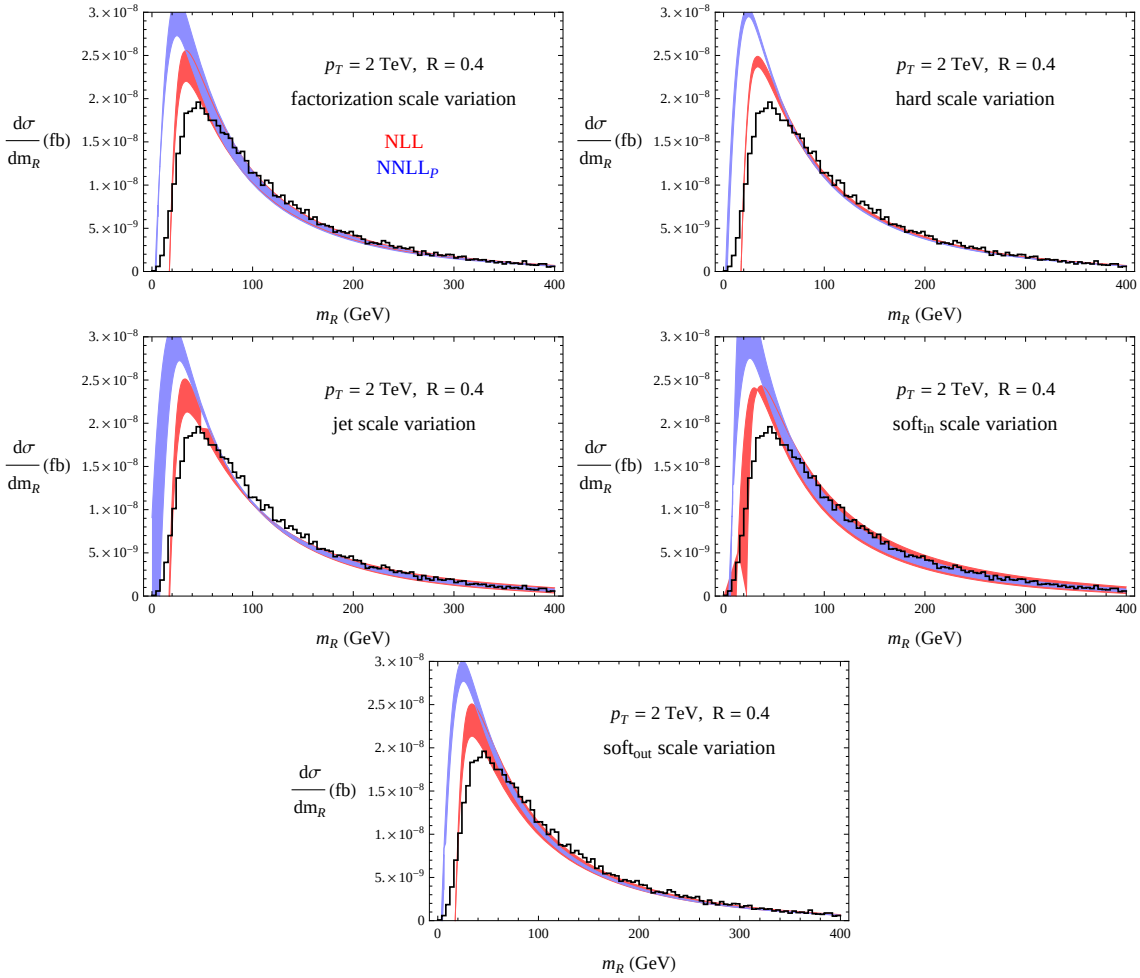

Figure 2.25: Scale uncertainties for $p_T = 2$ TeV and $R = 0.4$.

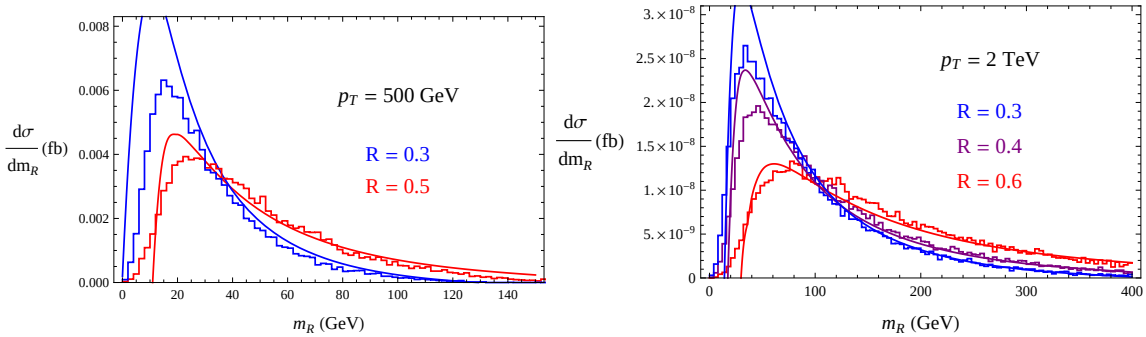

Figure 2.26: The resummed NLL jet mass distribution for different cone sizes for $p_T = 500$ GeV and 2 TeV (curves) compared to PYTHIA (histograms).

studies is that in both examples, the NGLs arose from combinations of various logarithms of a single scale, coming from integrals in separate phase space regions. To give a specific example, in the calculation of the cumulative doubly differential dijet mass distribution for hemispherical jets, the details of which can be found in [80], it was shown that the leading non-global logarithm is of the form

$$-\frac{4\pi^2}{3} C_F C_A \ln^2 \frac{E_L}{E_R} \,. \tag{2.105}$$

This is the coefficient of $\left(\frac{\alpha_s}{4\pi}\right)^2$ in the soft function, with E_L and E_R cumulant variables corresponding to integrals over $k_L = \overline{n} \cdot P_{X_L}$ and $k_R = n \cdot P_{X_R}$, respectively, where P_{X_L} and P_{X_R} are the total momentum of the soft radiation propagating in the left or right hemispheres and $n = (1, \hat{n})$ denotes the thrust axis. This double logarithm came from the sum of three contributions from the two gluon real emission graphs off the two Wilson lines

$$\begin{aligned}
&-\frac{4\pi^2}{3} C_F C_A \ln^2 \frac{E_L}{\mu} && \text{both gluons in left hemisphere} \\
&-\frac{4\pi^2}{3} C_F C_A \ln^2 \frac{E_R}{\mu} && \text{both gluon in right hemisphere} \\
&+\frac{8\pi^2}{3} C_F C_A \ln \frac{E_L}{\mu} \ln \frac{E_R}{\mu} && \text{one gluon in each hemisphere}
\end{aligned} \,.$$

One therefore expects a similar sum of phase space regions to produce the leading non-global logarithm for the soft function we need in this paper.

Now, we have already refactorized the soft function as

$$S(k_{\rm in}, k_{\rm out}, \mu) = \mathbf{S}(k_{\rm in}, \mu) S_r(k_{\rm in}, k_{\rm out}, \mu) \,, \tag{2.106}$$

with the regional soft function $\mathbf{S}(k_{\rm in},\mu)$ defined to have all the radiation going into the jet. Thus we expect a double logarithm similar to the first term in Eq. (2.106) to contribute at two loops

$$\mathbf{S}(\kappa_{\rm in},\mu) = \cdots + \left(\frac{\alpha_s}{4\pi}\right)^2 \Gamma^{\rm NGL} \ln^2 \frac{\kappa_{\rm in}}{\mu} \,, \tag{2.107}$$

where $\Gamma^{\rm NGL}$ might be $-\frac{4\pi^2}{3} C_F C_A$, but is yet unknown. Since this term has μ-dependence, it will contribute to the anomalous dimension of $\mathbf{S}$. Moreover, it will contribute a term with $\ln\mu$ in the anomalous dimension. This is unusual since, for a global observable, one normally expects that all of the $\ln\mu$ dependence in the anomalous dimension is proportional to $\gamma_{\rm cusp}$. We therefore expect similar non-cusp $\ln\mu$ dependence in the anomalous dimension of the regional soft function for the jet mass distribution as well.

With this educated guess, we expect that the two-loop regional soft function anomalous dimension for the annihilation channel has the form

$$\gamma_{\mathbf{S}} = \left(\frac{\alpha_s}{4\pi}\right)^2 \left[\left(2C_A\Gamma_1 + \Gamma^{\rm NGL}\right) \ln\left(\frac{1+\beta^2}{\beta}\frac{\kappa_{\rm in}}{\mu}\right) + C_A\gamma^s + \gamma^{\rm NGL} \right] \tag{2.108}$$

and similarly for the Compton channel, with $C_F \to C_A$ by Casimir scaling. Here, Γ_1 is the two-loop cusp anomalous dimension:

$$\Gamma_1 = 4\left(\frac{67}{9} - \frac{\pi^2}{3}\right) C_A - \frac{20}{9} n_f T_F \,, \tag{2.109}$$

and $\Gamma^{\rm NGL}$ and $\gamma^{\rm NGL}$ are unknown. By RG invariance, this implies that the anomalous dimension of the residual soft function must be

$$\gamma_{S_r} = \left(\frac{\alpha_s}{4\pi}\right)^2 \left[-4C_F\Gamma_1 \ln\left(\frac{1+\beta^2}{\beta}\frac{\kappa_{\rm out}}{\mu}\right) - \Gamma^{\rm NGL} \ln\left(\frac{1+\beta^2}{\beta}\frac{\kappa_{\rm in}}{\mu}\right) - 2C_F\gamma^s - \gamma^{\rm NGL} \right] \tag{2.110}$$

where γ_s is the two-loop direct-photon soft function anomalous dimension from [18]:

$$\gamma^s = \left(28\zeta_3 - \frac{808}{27} + \frac{11\pi^2}{3}\right) C_A + \left(\frac{224}{27} - \frac{4\pi^2}{9}\right) n_f T_F \,. \tag{2.111}$$

The terms proportional to Γ_1 and γ_s in Eq. (2.108) and Eq. (2.110), and also a known term proportional to the 3-loop cusp anomalous dimension, account for the global logarithms at NNLL.

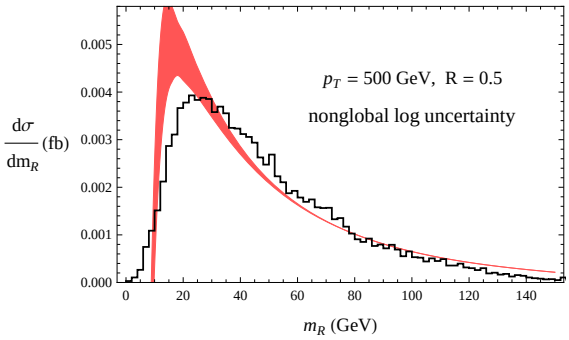

Figure 2.27: Estimation of the effect of leading non-global log resummation. Note that it affects significantly only the peak region of the distribution.

The $\Gamma^{\rm NGL}$ term parameterizing the unknown leading NGL. The $\gamma^{\rm NGL}$ anomalous dimension accounts for sub-leading NGLs, and the remaining non-global structure in the finite part of the two-loop soft function has effects which are formally $\mathrm{N^3LL}$.

Without performing a two-loop calculation, the expressions for $\Gamma^{\rm NGL}$ and $\gamma^{\rm NGL}$ are unknown. We estimate the effect of the missing terms by varying $\Gamma^{\rm NGL}$ between ± 100, since $100 \sim 4C_F\Gamma_1 \sim \frac{8\pi^2}{3}C_F C_A$. The result of performing such a variation is shown in Figure 2.27. The band in this plot shows a reasonable expectation of the improvement one could expect if the leading non-global logarithm could be resummed. We see that the NGL only affects significantly the distribution in the peak region.

2.2.7 Conclusions

In this paper we have calculated the distribution of jet mass at a hadron collider, for events in which the jet recoils against a hard photon. Our calculation includes resummation at the next-to-leading logarithmic level (NLL) which involves both final state radiation of the jet and initial state radiation of the colliding partons. We also have included resummation of all the global logarithmic terms at next-to-next-to-leading logarithmic level producing a distribution we label NNLL_p ("p" for partial, since the non-global logarithmic terms have not been resummed). Our approach is based on expanding around the threshold limit, where the photon has very large momentum. By demanding the photon be hard, we force the hadronic final state to be that of a single jet for which a simple factorization formula exists. Our result is differential in the jet and photon rapidities and transverse momenta, although we assume the photon and jet have equal

and opposite transverse momenta, which is true at leading power.

We have compared our theoretical calculation to the output from PYTHIA, and find very good agreement. Although PYTHIA is only formally accurate to the leading-logarithmic level, it has elements of subleading logarithms, and is expected to be in good agreement with collider data. Since we are able to include color coherence effects, from initial state radiation, as well as subleading logarithms, our calculation is more precise than PYTHIA, as far as perturbative QCD is concerned. Since PYTHIA also includes hadronization it is more likely to describe the data well for very small jet mass. It would be interesting to compare both directly to collider data from the LHC when it becomes available.

The two scales in our distribution, the photon p_T and the jet mass m_R lead to non-global logarithms. This is because in our approach there are two thresholds, $m_R \to 0$ and $m_X \to 0$, where m_X is the mass of everything-but-the-photon. In particular, there are two soft scales, $k_{\rm in}$ associated with soft radiation in the jet, related to m_R, and $k_{\rm out}$ associated with radiation out of the jet, which can be related to $m_X^2 - m_R^2$. Non-global logarithms of the ratio of these scales make resummation difficult beyond the NLL level. An alternative calculation would be to impose a jet veto at a scale similar to the soft scale. Then the non-global structure would reduce to a single number, which one might estimate or argue to be small. However, for an inclusive jet mass calculation, it seems impossible to avoid non-global structure and therefore resumming non-global logarithms is necessary for NNLL resummation.

Although we have not been able to resum the non-global logs in this paper, we found that if one ignores them completely, by choosing a single scale for the entire soft function, the distribution is completely wrong. This is because, using SCET alone, the two soft scales are not distinguished. Instead, we observe that contributions to the soft function coming from radiation going entirely into the jet can be consistently factorizes off. There are many ways to refactorize the soft function, and we make one particular choice, preserving the color structure associated with the hard directions. We give an operator definition to this regional soft function and calculate it at one loop. The regional soft function has a natural scale associated with soft/n_J-collinear modes. Allowing ourselves to pick two different soft scales, which we do numerically, gives a result which is in very good agreement with PYTHIA, in the region that our calculation can be trusted.

There are many directions in which this work can be continued. It would be interesting to calculate the regional soft function at two loops, to see its non-global structure. One might hope that, since we expect an anomalous dimension for this soft function to have μ dependence related to the leading non-global logarithm, that with further insight non-global logarithms could be resummed. Then one could produce an NNLL calculation of jet mass. Other related applications would include a calculation of the jet mass in dijet events, for which there is already data [92] and the one-loop hard function and anomalous dimensions have already been prepared [93], or a calculation of jet mass in direct photon events including a jet veto. With a jet veto one can force single-jet kinematics well away from threshold and the size of the non-global structure can be controlled. However, the calculation would be significantly more complicated than what we have done here. In addition, it would be interesting to pursue the consideration of the jet mass distribution using different jet algorithms.

Y: I saw a new citation of our AdS paper today!

M: Oh no!

a conversation in Jefferson 455

3

Jet Physics from Static Charges in AdS

The richness of quantum chromodynamics is hidden in its deceptively simple Lagrangian $\mathcal{L} = -\frac{1}{4}F_{\mu\nu}^2 + \overline{q}i\not{D}q - m\overline{q}q$. At low energy, the theory has a mass gap $\sim \Lambda_{\rm QCD}$ and a discrete set of bound states. At high temperature it forms a quark-gluon plasma. At high energy, another phenomenon emerges: jets. The preference for producing collimated jets arises from logarithmic enhancement due to collinear and soft singularities. The cross section for production of quarks alone is not infrared safe, but the cross-section for production of jets, built from quarks accompanied by collinear and soft radiation, is a calculable and well-defined quantity.

Another way to think about jets is through Sudakov logs. For example, consider the mass of a jet m_J computed in perturbation theory, assuming massless quarks. At leading order, the distribution is singular, $d\sigma/dm_J^2 \propto \delta(m_J^2)$, since there is no radiation. At higher orders, the distribution contains terms like $\alpha_s \frac{1}{m_J^2} \ln \frac{m_J^2}{Q^2}$ where Q is a typical hard scale, like the jet energy.

In terms of the integrated jet mass $R(m_J^2) = \int_0^{m_J^2} dm'^2 (d\sigma/dm'^2)$, the series has the structure

$$R(m_J^2) = 1 + \alpha_s \ln^2 \frac{m_J^2}{Q^2} + \alpha_s^2 \ln^4 \frac{m_J^2}{Q^2} + \cdots \tag{3.1}$$

The coefficients of these terms and the precise definition of Q depend on the particular process, and for simplicity, we have only shown the leading large logarithms. These logs are Sudakov double logs, of the form $\alpha_s^n \ln^{2n} x$. They come from the region of overlapping soft and collinear divergences and are present in any gauge theory with massless charged particles. Sudakov logs invalidate the perturbation expansion. However when one re-sums the series, the final non-perturbative expression, schematically $R(m_J^2) = \exp(-\alpha_s \ln^2 \frac{m_J^2}{Q^2})$ vanishes at $m_J^2 = 0$ implying that the cross section for producing massless quarks is zero. The objects that are produced are jets, of finite mass. The coefficient of the Sudakov log in this exponential is a function of the coupling constant $\Gamma_{\rm cusp}(\alpha_s)$ called the cusp anomalous dimension.

Sudakov logs and the cusp anomalous dimension are simplest to study in the soft limit of QCD, where one treats a massless parton (quark or gluon) as a hard charged object plowing through a background of soft radiation. The soft radiation cannot change the direction or energy of the hard parton, and so the parton factorizes out as a Wilson line source for soft gluons. This treatment of soft radiation becomes manifest when using QCD factorization theorems to describe hard collisions, see the reviews [83, 84], or when using soft-collinear effective theory (SCET) [8,9,78,79,94] to describe the interaction of soft and collinear partons in hard collisions. Thus using Wilson line operators the soft interaction properties of jets can be investigated. Wilson lines also appear in the study of scattering in planar $\mathcal{N} = 4$ SYM, via a surprising duality relating null polygonal loops to scattering amplitudes [95–102].

A Wilson line is defined as

$$\mathcal{W}(C) = \mathcal{P} \exp \leftrightarrow (ig \int_C A_\mu \mathrm{d}x^\mu) \,, \tag{3.2}$$

where C is a contour describing the path of the partons and $\mathcal{P}$ denotes path-ordering, along the contour. Typically, one takes C to be a simple closed contour, and makes $\mathcal{W}$ gauge invariant by taking a trace. We will be creating gauge invariants using $\mathcal{W}$ in more complicated ways. For

example, a process like $e^+e^- \to$ hadrons is, to leading order in α_s, described by $e^+e^- \to \overline{q}q$ with the quarks traveling off in the $n_1^\mu = (1, \vec{v})$ and $n_2^\mu = (1, -\vec{v})$ directions. In this case, we can write $\mathcal{W}(C)$ as the product of two Wilson lines from 0 to ∞ along n_1 and n_2, with one in the fundamental and one in the anti-fundamental representation.

More generally, for N-jet production in e^+e^- collisions or $(N-2)$-jet production in pp or $p\overline{p}$ collisions, we are interested in a product of N Wilson lines along directions n_i^μ,

$$\mathcal{W}_{d_1,\cdots,d_N}(n_1,\cdots,n_N) = t_{c_1,\ldots,c_N} \prod_{i=1}^{N} \leftrightarrow (\,\mathcal{P} \exp\, ig \int_0^\infty ds\; n_i \cdot A^a(s\, n_i) \boldsymbol{T}_i^a)_{d_i}^{c_i}\,. \tag{3.3}$$

The lines here are all outgoing. For an incoming Wilson line we simply replace the path-ordering, $\mathcal{P}$, by anti-path ordering, $\overline{\mathcal{P}}$, and replace the ig with $-ig$. Let us take a moment to explain the remaining notation. The $\boldsymbol{T}_i$ are gauge generators in the color representation R_i associated with parton i. They satisfy $[\boldsymbol{T}_i, \boldsymbol{T}_j] = 0$ for $i \neq j$, along with the color conservation relation $\sum_i \boldsymbol{T}_i = 0$. For light quarks and gluons the directions n_i^μ are light-like, $n_i^2 = 0$, while for heavy quarks like the top where mass effects are important, we have $n_i^2 \neq 0$. To keep our discussion general we will mostly work with $n_i^2 \neq 0$. Often in the literature the time-like component of n_i^μ is taken to be positive, and the integration along the path extends from $s = 0$ to ∞ for outgoing partons and from $s = -\infty$ to 0 for incoming partons. For simplicity we will always take $s = 0$ to ∞ and let n_i^μ have a negative time-like component for incoming particles.[1]

$\mathcal{W}$ depends on a tensor $t_{c_1,\ldots,c_N}$, where the c_i denote the color indices at $s = 0$. These tensors live in the color-invariant subspace $\mathcal{I}$ of the tensor product of representations associated with each jet

$$\mathcal{I} = \Big(R_1 \otimes R_2 \otimes \cdots \otimes R_N\Big)_{\text{color singlet subspace}}\,. \tag{3.4}$$

In a scattering process, the short-distance physics at the origin specifies the relevant channels and determines the $t_{c_1,\ldots,c_N}$, which are Clebsch-Gordan coefficients.

The d_i indices on Eq. (3.3) denote the color indices at $s = \infty$. Matrix elements of $\mathcal{W}(n_i)$ will be infrared divergent unless the d_i are contracted, as in various physical calculations. For

[1] Another common convention in the literature is to use tangent vectors to the contour v_i^μ, in place of our n_i^μ. For a 2-jet Wilson line for $e^+e^- \to q\overline{q}$, the relation to our conventions is $v_1 = -n_1$ to $v_2 = n_2$, where n_1 and n_2 have positive time-components.

example, Wilson line matrix elements contribute to matching calculations in SCET, see eg. [8, 26, 34, 35, 93, 103]. Operators describing the hard interaction for N-jet production appear in the SCET Lagrangian as

$$\begin{aligned}\mathcal{L} &= C_{c_1,\ldots,c_N}(s_{ij})\mathcal{O}^{c_1,\ldots,c_N}(n_i) \\ &= C(s_{ij})\left[\chi_{n_j}^{d_j}\cdots\overline{\chi}_{n_k}^{d_k}\cdots\mathcal{B}_{n_\ell}^{\perp d_\ell}\ldots\right]\mathcal{W}_{d_j,\cdots,d_k,\cdots,d_\ell,\cdots}(n_i)\,,\end{aligned} \tag{3.5}$$

where $C_{c_1,\ldots,c_N}(s_{ij}) = t_{c_1,\ldots,c_N}C(s_{ij})$ is a Wilson coefficient depending on hard scales $s_{ij} = p_i\cdot p_j$, where $p_i = n_iQ_i$ are the jet four-momenta at leading power (and in general we have a sum over terms of this sort for the possible color structures $t_{c_1,\ldots,c_N}$). In square brackets are collinear quark (χ_{n_j}) and gluon ($\mathcal{B}_{n_\ell}^{\perp}$) fields that are each contracted in color with the d_j or d_ℓ indices from the Wilson line. In a matching computation the infrared divergences from matrix elements of collinear fields and from the soft Wilson lines combine to yield the same infrared divergences as for the corresponding matrix element in QCD, ensuring that the Wilson coefficients $C(s_{ij})$ are finite. In this computation there is a cancellation of overlapping infrared and ultraviolet divergences between the collinear matrix elements and matrix elements involving the soft Wilson lines.

Alternatively, the Wilson line can be used to calculate a soft function (for examples see [6, 18, 26, 54, 58, 104–107]), which appear in physical cross sections for hard processes with jet production,

$$S(k) = \langle 0|\mathcal{W}_{d_1,\cdots,d_N}(n_i)\hat{M}(k)\mathcal{W}^{\dagger}_{d_1,\cdots,d_N}(n_i)|0\rangle\,. \tag{3.6}$$

In this case, the d_i indices of the Wilson line are contracted with those of its adjoint and the product includes a measurement function $M(k)$ which acts on final state soft partons, measuring momentum components k. These soft functions are cross sections for soft radiation and are infrared finite by themselves.

An important property of Wilson lines is that, even though they are non-local objects, they are multiplicatively renormalizable. A number of **features** are known (or conjectured) about the renormalization of $\mathcal{W}(C)$.

1. If the contour C is smooth and not self-intersecting, any ultraviolet divergences in correlators of $\mathcal{W}(C)$ are exactly canceled by field strength and coupling constant counterterms.[2] For the $\mathcal{W}(n_i)$ relevant for jet physics, the Wilson line has kinks and self-intersections in its path at the origin, and C is not smooth. In this case additional divergences are present and the Wilson line picks up an anomalous dimension Γ. This anomalous dimension can only depend on the angles β_{ij} where the contour abruptly changes direction or on crossing angles at self-intersections [108]. When the direction of the contour changes from n_i^μ to n_j^μ, the *cusp angle* is

$$\cosh \beta_{ij} = \frac{n_i \cdot n_j}{|n_i||n_j|}\,, \tag{3.7}$$

where here we consider paths where $|n_i|^2 = n_i^2 \neq 0$. For two jets from $e^+e^- \to q\overline{q}$ (with massive quarks), β_{12} is real. More generally, for $e^+e^- \to N$ jets, all the n_i^μ correspond to final state jets and each β_{ij} is real.

2. At order α_s, the anomalous dimension is

$$\Gamma = -\frac{\alpha_s}{\pi} \sum_{i<j} \boldsymbol{T}_i \cdot \boldsymbol{T}_j \left((\beta_{ij} - i\pi) \coth \beta_{ij} - 1 \right) \tag{3.8}$$

where the sum is over pairs of jet directions n_i, n_j. The color structure $\boldsymbol{T}_i \cdot \boldsymbol{T}_j \equiv \boldsymbol{T}_i^a \boldsymbol{T}_j^a$ involves the generators from Eq. (3.3). These generators allow the anomalous dimension Γ to mix the different invariant tensors t_{c_i} in Eq. (3.3) during renormalization group flow. Γ is an operator on the space $\mathcal{I}$, which we can write as a general expression with generators $\boldsymbol{T}_i$ acting on the i-th tensor factor.

3. In situations like jet production in hadron collisions or deep inelastic scattering (DIS), there are both initial state and final state Wilson lines. Initial state Wilson lines follow paths that extend backward in time from the origin, $n^\mu = (-1, \vec{v})$. For cusps between initial and final state partons β_{ij} is complex, but we can define a real cusp angle $\gamma_{ij} = \beta_{ij} - i\pi$. This

[2] At least this is the case in dimensional regularization. More generally, there can be an overall linear divergence proportional to the length of the Wilson line, which can also be subtracted off with an appropriate counterterm.

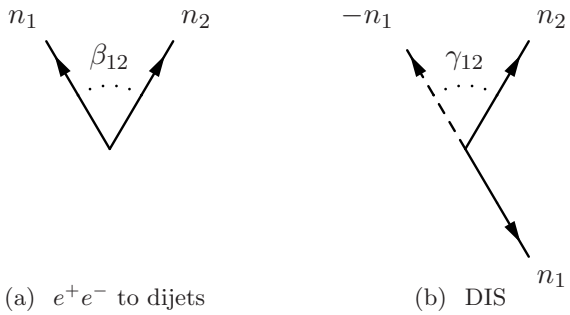

(a) e^+e^- to dijets (b) DIS

Figure 3.1: Our definitions for the cusp angles β_{12} and γ_{12}. β_{12} is real when both Wilson lines represent final-state partons, while γ_{12} is real when one Wilson line represents a final state parton, and one represents an initial state parton.

alternative definition of the cusp angle is related to the previous one by a sign

$$\cosh \gamma_{ij} = -\frac{n_i \cdot n_j}{|n_i||n_j|} = -\cosh \beta_{ij} \,, \tag{3.9}$$

The angles β_{ij} and γ_{ij} are illustrated in Fig. 3.1. Whether γ_{ij} or β_{ij} are complex affects the complexity of the anomalous dimension, which has physical consequences. For example, these factors of $i\pi$ can partly explain the large K-factor in the Higgs production cross section [109].

4. *Abelian exponentiation*: The anomalous dimension in QED without propagating quarks is one-loop exact.

5. In the limit that the tangent vectors become lightlike, $n_i^2 \to 0$ and $\beta_{ij} \to \infty$, the anomalous dimension becomes *linear* in the cusp angles β_{ij} to all orders in perturbation theory [108, 110, 111],

$$\Gamma = -\sum_{i<j} \mathbf{\Gamma}^{ij}(\alpha_s)\beta_{ij} + \dots \tag{3.10}$$

where "..." are terms that are constant or go to zero as $\beta_{ij} \to \infty$. The possibility that $\mathbf{\Gamma}^{ij}(\alpha_s) = \boldsymbol{T}_i \cdot \boldsymbol{T}_j \Gamma_{\text{cusp}}(\alpha_s)$, where $\Gamma_{\text{cusp}}(\alpha_s)$ is independent of i and j, is known as *Casimir scaling*. This has been shown by explicit calculations for two lines at three loops [112], and by other arguments for multiple lines up to 4-loops [106].

Exactly at $n_i^2 = 0$, $\beta_{ij} = \infty$ and the anomalous dimension is singular. This singularity is due to additional overlapping soft and collinear divergences, and induces dependence of

the anomalous dimension on the renormalization group scale μ. For example, at one loop,

$$\Gamma = \frac{\alpha_s}{\pi} \sum_{i<j} \boldsymbol{T}_i \cdot \boldsymbol{T}_j \ln \frac{\mu^2}{n_i \cdot n_j \Lambda^2} + \dots \,. \tag{3.11}$$

Here Λ is another scale with dimension of mass. In matrix elements of Wilson lines, which are infrared divergent, Λ is related to the infrared regulator. When collinear graphs are included in the the calculation of Wilson coefficients for a hard scattering process, as in Eq. (3.5), the infrared regulator will cancel and Λ will be replaced by a hard scale $\Lambda^2 \to \pm Q_i Q_j$. In calculating soft functions, as in Eq. (3.6), the infrared divergences will cancel between real and virtual contributions, and the scale will be replaced by a physical one, relevant to the soft function $\Lambda^2 \to k_i k_j$. At all orders, the anomalous dimension is linear in $\ln \mu^2$, for the same reason that Γ is linear in β_{ij} at large cusp angles. Proofs of Eq. (3.10) for two Wilson lines have been given in Refs. [103, 110, 113], and for multiple lines in Refs. [106, 114, 115].

6. At 1-loop the anomalous dimension must be a sum over pairs of Wilson lines. Surprisingly some pairwise structure seems to persist to higher orders in perturbation theory. For example, in the massless case, the anomalous dimension of a 4-jet Wilson line at 2-loops, as a matrix in color space, was found to be exactly proportional to the 1-loop anomalous dimension, an unexpected result [116].

   It has been conjectured that for massless jets the anomalous dimension of the N-jet Wilson line has a pairwise structure to all orders in perturbation theory for the $\ln \mu$ term [106, 115, 117–119]

$$\Gamma \stackrel{?}{=} \sum_{i \neq j} \Gamma^{ij}_{\text{cusp}}(\alpha_s) \boldsymbol{T}_i \cdot \boldsymbol{T}_j \ln \frac{\mu^2}{n_i \cdot n_j \Lambda^2} + \gamma(\alpha_s, \{n_k \cdot n_\ell\}) \,. \tag{3.12}$$

   Given Eq. (3.10), Eq. (3.12) becomes non-trivial for four or more Wilson lines where matrices appear for the color structures. If there were a general proof of Casimir scaling it would imply that $\Gamma^{ij}_{\text{cusp}}(\alpha_s)$ cannot depend on the representations i and j, making the coefficient a universal function $\Gamma^{ij}_{\text{cusp}}(\alpha_s) = \Gamma_{\text{cusp}}(\alpha_s)$. This was conjectured in [106, 117].

   It has been furthermore conjectured that the regular anomalous dimension γ is independent

of conformal cross ratios (combinations of cusp angles $\beta_{ij} + \beta_{k\ell} - \beta_{ik} - \beta_{j\ell}$ that approach nontrivial constants as the $\beta_{ij} \to \infty$), so that [106]

$$\gamma(\alpha_s, \{n_i \cdot n_j\}) \stackrel{?}{=} \sum_i \gamma^i(\alpha_s)\,. \tag{3.13}$$

This is known to be true to $\mathcal{O}(\alpha_s^2)$. At $\mathcal{O}(\alpha_s^3)$ and beyond general constraints on the form of $\gamma(\alpha_s, \{n_i \cdot n_j\})$ were reviewed in Ref. [106, 120]. Dependence on conformal cross ratios appears not to be forbidden by symmetry arguments, but whether this dependence exists is an open question. Possible terms at $\mathcal{O}(\alpha_s^3)$ which were not obviously forbidden were suggested in Ref. [120]. Very recently it was argued that these terms are forbidden by considerations from the Regge limit in Refs. [121, 122].

Most of these results have been shown only through direct, and sometimes laborious calculations. Even a simple result, such as Abelian exponentiation, requires the use of eikonal identities and monitoring of combinatoric factors. In this paper, we will show how some of these results can be understood in a simple way using a mapping inspired by the approximate conformal invariance of QCD.

At the classical level, QCD is conformally invariant. This symmetry is broken by quantum effects, but for high energy scattering it continues to have implications for the structure of perturbative results. Examples of the implications of conformal symmetry for QCD can be found in Refs. [111, 123–127]. Our main focus here will be on exploiting conformal invariance to understand properties of the anomalous dimensions of Wilson lines relevant for jet physics.

A Wilson line emanating from the origin in the direction n^μ comprises the points $x^\mu = sn^\mu$, for $s > 0$. A scale transformation is simply a change in s. Scale invariance is made more manifest by defining a new time coordinate $\tau \equiv \ln |x|$ where $|x|$ is the (Lorentzian) distance from the origin. This makes the Wilson lines parallel, as shown in Figure 3.2. In terms of τ, rescaling becomes simply time translation, and conformal symmetry becomes the statement that the physics is time translation invariant in τ. The Wilson lines become static charges whose energy is the anomalous dimension. Spatial slices in these coordinates are copies of Euclidean Anti-deSitter space (AdS). In this paper, we describe how many of the features of Wilson lines enumerated above can be understood in AdS coordinates. For example, that the Coulomb potential is one-

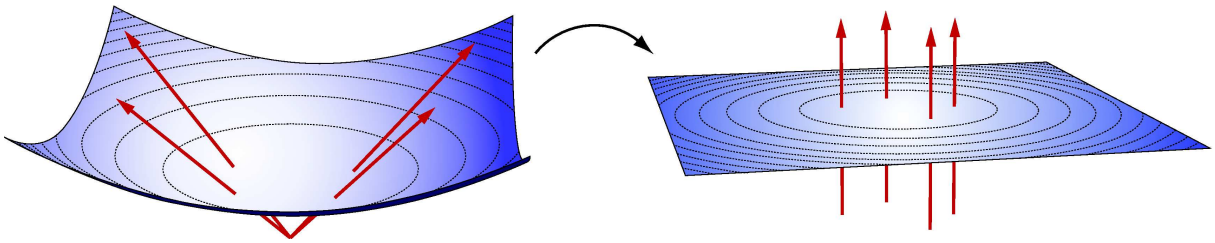

Figure 3.2: A coordinate change maps Minkowski space to $\mathbb{R} \times$ AdS. In this figure the outgoing Wilson lines become static charges in AdS, and their tree level energy in AdS is equal to the original one-loop anomalous dimension for the lines.

loop exact in QED automatically implies that the anomalous dimension of multiple Wilson line operators are one-loop exact in QED.

In addition to providing a pleasing physical picture, radial coordinates make a number of calculations much easier. One of the reasons that the classical conformal invariance of QCD rarely simplifies diagrammatic computations is that it is broken by standard gauge choices, such as Feynman gauge. Feynman gauge in flat space leads to kinetic mixing between the time-like components A_τ and space-like components A_i of the gauge field in $\mathbb{R} \times$ AdS. Here we introduce a new gauge, which we call *conformal gauge*, in which there is no such mixing. One consequence is that in this gauge, since only A_τ is sourced by the Wilson lines, and there is no A_τ^3 or A_τ^4 vertex in Yang-Mills theory, many of the non-planar graphs at 2 and 3-loops automatically vanish. This automatically implies that the only graphs at 2-loops contributing to the anomalous dimension have gluons going between pairs of Wilson lines, which strongly suggests a pairwise structure. This reasoning alone does not imply that Γ must be pairwise at 3-loops or higher.

The organization of this paper is as follows. In Sec. 3.1 we discuss the appropriate mapping of Minkowski to AdS coordinates and simple implications for multi-Wilson line configurations. In Sec. 3.2 we compute the one-loop anomalous dimension of $\mathcal{W}$ by carrying out a classical energy computation in AdS, paying special attention to boundary conditions and differences for incoming and outgoing lines. We repeat this computation using the standard one-loop diagrams in Sec. 3.3, but utilizing the AdS coordinates. A discussion of the lightlike limit and a way to think about the imaginary energy in AdS is given in Sec. 3.4. In Sec. 3.5, we introduce conformal gauges which do not mix the time and spatial components of the gauge boson propagator in $\mathbb{R} \times$ AdS, and in Sec. 3.6 we demonstrate the utility of such gauges by computing a two-loop contribution to the anomalous dimension of $\mathcal{W}$ in a simple way. In

Sec. 3.7, we mention an interesting formal relation between anomalous dimension calculations for $\mathcal{W}$ and Witten diagrams. We conclude in Sec. 3.8. Several technical discussions are relegated to appendices. In App. B.1 we construct the most general class of conformal gauges without auxiliary parameters, and in App. B.2 we give the corresponding Feynman rules for ghosts.

3.1 Conformal Coordinates

Having replaced hard partons by Wilson lines, the soft physics is described simply by Yang-Mills theory, which enjoys classical conformal invariance in four dimensions. Equivalently, the soft action coupled to a background metric $g_{\mu\nu}$ is Weyl-invariant: it is unchanged under a local rescaling of the metric, $S_{\rm YM}[g] = S_{\rm YM}[e^{2\omega(x)}g]$. Although this symmetry is broken by fermion masses and the QCD scale anomaly that generates $\Lambda_{\rm QCD}$, it continues to have important implications for scattering amplitudes at high energies.

One reason conformal invariance can be useful for QCD is that some quantities are completely insensitive to the breaking of conformal invariance. For example, the one-loop cusp anomalous dimension Eq. (3.8) is independent of the matter content of the theory, since Feynman diagrams contributing to it only involve a single gluon exchanged between Wilson lines. Consequently, it has a universal form, and we can compute it assuming exact conformal invariance. In other words, we can compute it in our favorite conformal theory, for instance $\mathcal{N} = 4$ SYM, and the result will hold in any gauge theory. In the next two sections, we will use this fact to give a simple and intuitive derivation of Eq. (3.8).

To the extent that conformal symmetry is a good approximation, it is natural to apply techniques which have proved useful for studying conformal field theories in other contexts. In particular, we consider *radial quantization* around the origin. In Ref. [95] this was used to study the anomalous dimensions of high spin operators, and has also been used in Ref. [123]. In this section, we review the relevant ideas in the context of N-jet Wilson lines.

Consider a Wilson line in the direction n^μ. We can write $n^\mu = (\cosh\beta, \sinh\beta\,\hat{\mathbf{n}})$, with $\hat{\mathbf{n}}$ a unit vector in $\mathbb{R}^3$, and $x^\mu = e^\tau n^\mu$. The path of the Wilson line is then described by

$$t = e^\tau \cosh\beta, \qquad r = e^\tau \sinh\beta, \qquad \beta, \theta, \phi \text{ fixed}, \tag{3.14}$$

with τ running from $-\infty$ to ∞. Wilson lines in different directions will correspond to different values of β, θ and ϕ. In these coordinates, the Minkowski metric becomes

$$\begin{aligned} ds^2_{\mathbb{R}^{1,3}} &= dt^2 - dr^2 - r^2 d\Omega_2^2 \\ &= e^{2\tau}\left[d\tau^2 - (d\beta^2 + \sinh^2\beta\, d\Omega_2^2)\right]. \end{aligned} \tag{3.15}$$

Strictly speaking, this metric describes only a patch of $\mathbb{R}^{1,3}$ — namely the interior of the future light-cone. We will return to this point shortly.

The idea of radial quantization is to interpret τ as a new time coordinate. A naïve complication in this picture is that the metric Eq. (3.15) is now time-dependent. However, in a conformal theory, the dynamics is independent of the local scale, and we can equivalently consider our theory with any metric related via $ds^2 \to e^{2\omega(x)} ds^2$. Thus, let us drop the overall $e^{2\tau}$ to obtain a simple time translation-invariant product space,

$$ds^2_{\mathbb{R}\times \mathrm{AdS}} = d\tau^2 - (d\beta^2 + \sinh^2\beta\, d\Omega_2^2). \tag{3.16}$$

The spatial part of this metric is the 3D hyperboloid, or Euclidean Anti-deSitter space. With a slight abuse of nomenclature, we call it simply AdS.

In radial coordinates, the origin maps to $\tau = -\infty$ and motion along a Wilson line corresponds to shifts in τ. So to the extent that our theory was scale invariant in Minkowski space, it is now time-translation invariant in $\mathbb{R} \times$ AdS. Each Wilson line sits at fixed (β, θ, ϕ) and extends from $-\infty$ to ∞ in the time coordinate τ. That is, each Wilson line becomes a static charge in AdS. For perturbative computations in QCD (where conformal invariance is broken by the scale anomaly) we may simply adopt the change of coordinates in Eq. (3.14) as a method to carry out computations. If the computation involves ingredients satisfying the conformal invariance then the factors of e^{τ} will cancel out, and the result will be constrained by properties of the AdS space.

For the sake of doing calculations, a key point is that the dilatation operator in Minkowski space maps to the Hamiltonian in AdS in radial quantization,

$$\mathcal{D}^{\mathbb{R}^{1,3}} = x^\mu \partial_\mu = \partial_\tau = i\mathcal{H}^{\mathbb{R}\times \mathrm{AdS}}. \tag{3.17}$$

Consequently, the eigenvalue of dilatation — the dimension (or when acting on classically scale invariant Wilson lines, the anomalous dimension) — is just i times the energy in AdS. So we can calculate anomalous dimensions by calculating energies and apply our intuition from electrodynamics to understand anomalous dimensions of Wilson lines.

What can the energy of two static charges in AdS depend on? Since the space is homogeneous, it can depend only on the geodesic distance between the charges. For example, suppose we have two time-like Wilson lines, pointing in the directions n_1^μ and n_2^μ, normalized so that $n_1^2 = n_2^2 = 1$. We may first go to the rest frame of one, $n_1^\mu = (1, 0, 0, 0)$, and then rotate so the other is at $n_2^\mu = (\cosh\beta_{12}, \sinh\beta_{12}, 0, 0)$. Then the geodesic distance between them, using the spatial part of the metric Eq. (3.16), is just

$$\Delta s = \beta_{12}\,. \tag{3.18}$$

Considering also that $\frac{n_1\cdot n_2}{|n_1||n_2|} = \cosh\beta_{12}$, we see that the geodesic distance in AdS is the cusp angle. Thus, the energy of the two charges, and hence the anomalous dimension in Minkowski space, can depend only on the cusp angle. This was **feature 1** from the introduction. More succinctly, the original Lorentz symmetry of Minkowski space becomes the isometry group of AdS in radial coordinates. Just as Lorentz invariance dictates that the anomalous dimension can depend only on the cusp angle, the isometries of AdS dictate that the energy can depend only on the geodesic distance.

We can also consider initial state Wilson lines. For example, in deep inelastic scattering as Bjorken $x \to 1$, the initial state contains an energetic proton in the Breit frame, the final state contains a jet, and the Wilson line description applies. In our convention, the spatial vectors for these lines still point out from the origin, and the lines extend to negative Minkowski times. Instead of Eq. (3.14), the path of an initial state line is then described by

$$t = -e^\tau \cosh\gamma, \qquad r = e^\tau \sinh\gamma, \tag{3.19}$$

for fixed real γ. When comparing the coordinates for parallel initial and final state lines we have $\hat{n} \to -\hat{n}$ so $\theta \to \theta + \pi$ and $\phi \to \phi + \pi$. In radial quantization, initial state lines map to static charges in a different copy of $\mathbb{R} \times$ AdS comprising points in the interior of the past

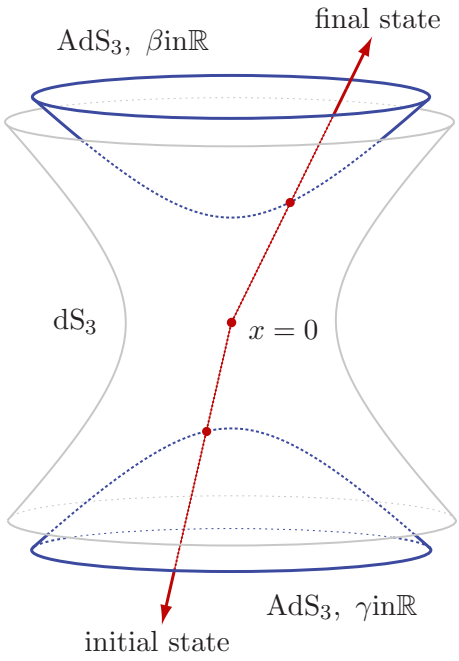

Figure 3.3: In radial quantization, final state lines map to a copy of AdS_3 at positive Minkowski times, while initial state lines map to a second copy of AdS_3 at negative Minkowski times. Points that are space-like separated from the origin map to dS_3.

light-cone (Figure 3.3). It is useful to think of this second copy of AdS as being related by analytic continuation to the first. Since from Eq. (3.9) we have $\cosh\gamma = -\cosh\beta$, we can write $\beta = \gamma + i\pi$. Both copies of AdS (along with a copy of deSitter space describing points at spacelike separation from the origin) are related by analytic continuation to the three-sphere S^3 that one would obtain by repeating the exercise of radial quantization starting from Euclidean space, $\mathbb{R}^4$. This will be a useful tool in the following section.

For most of the remainder of the paper, we will focus on time-like Wilson lines whose directions are normalized to $n^2 = 1$. Since all the energies and dimensions are independent of rescaling of the n's, the dependence on $|n|$ can be put back by dimensional analysis: $n_i^\mu \to \frac{n_i^\mu}{|n_i|}$. We will also have occasion to consider the light-like limit $n^2 \to 0$, which is phenomenologically relevant for the majority of processes at colliders. Many of the properties of the light-like case can be derived as a limiting case of the general time-like results. In the light-like limit $n_i^2 \to 0$, and the charges move towards the boundary of AdS with $\beta \to \infty$. Some results simplify for $n^2 = 0$, and when appropriate we will consider this case separately.

3.2 Classical AdS energies

In radial coordinates, we have seen that the anomalous dimension of a collection of Wilson lines intersecting at a point is proportional to the energy of a collection of static charges in AdS. This energy can only depend on the geodesic distance between the charges, which is the same as the cusp angle $\beta_{ij} = \cosh^{-1} n_i \cdot n_j$. Now let us calculate that energy.

The energy of two charges in QCD at leading order is given, as in QED, by solving Laplace's equation for the scalar potential A_τ in the presence of point sources J_μ given by $J_\tau = \delta^3(x)$ and $\vec{J} = 0$. The homogeneous solutions are

$$\frac{1}{\sinh^2\beta}\partial_\beta\left(\sinh^2\beta\,(\partial_\beta A_\tau)\right) = 0 \quad \Rightarrow \quad A_\tau(\beta) = C_1 + C_2\coth\beta \tag{3.20}$$

Unfortunately, neither of these is the physically correct answer. This can be seen most easily by looking at the large β limit, where we expect $A_\tau(\beta)$ to be linear in β. In this limit Eq. (3.20) behaves as a constant.

The problem with this potential is that it has the wrong boundary conditions. This is easiest to understand by analytically continuing to Euclidean space. Defining $\beta = i\alpha$, the metric becomes

$$ds^2 = d\tau^2 + d\alpha^2 + \sin^2(\alpha)d\Omega_2^2 = d\tau^2 + d\Omega_3^2, \tag{3.21}$$

which describes a Euclidean cylinder $\mathbb{R}\times S^3$. The Wilson lines are now static charges at points on a three-sphere. The general homogeneous solution to Laplace's equation on $\mathbb{R}\times S_3$ is the analytic continuation of Eq. (3.20),

$$A_\tau(\alpha) = C_1 + C_2\cot\alpha. \tag{3.22}$$

Since $\cot\alpha$ has a pole at both $\alpha = 0$ and $\alpha = \pi$, Eq. (3.22) actually describes a configuration with two charges: a (+) charge at the north pole and a phantom (−) charge at the south pole. If we now consider two physical charges separated by an angle $\Delta\alpha$ on the sphere, we obtain a potential for not just these two charges, but also for two additional phantom charges, which is incorrect. This is shown graphically in Figure 3.4(a). The AdS version is shown in Figure 3.4(b)

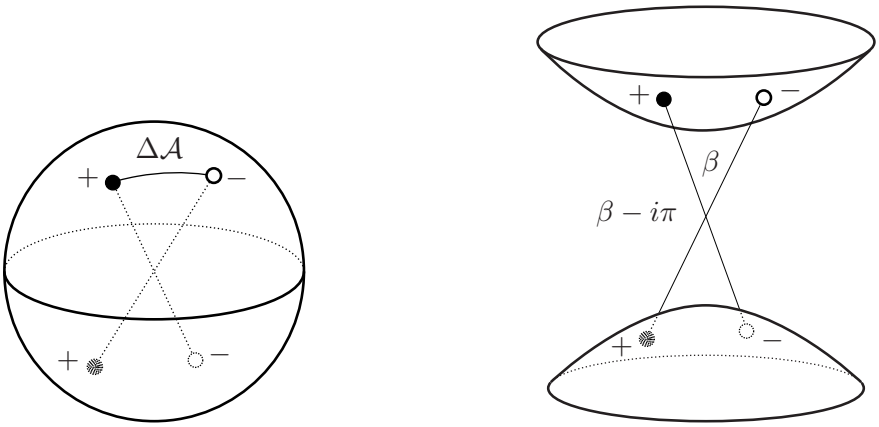

(a) phantom charges on S^3 (b) phantom charges on AdS

Figure 3.4: The naive solution to Laplace's equation on the Euclidean cylinder, Eq. (3.22), represents the potential in the presence of additional phantom charges at diametrically opposite points on the sphere, Figure 3.4(a). After analytic continuation back to Minkowski signature, the phantom charges map to another copy of AdS, Figure 3.4(b), corresponding to phantom initial state particles.

and discussed more below.

A nice way to get the correct solution to Laplace's equation on the Euclidean cylinder is to add and subtract a constant charge density. On the Euclidean cylinder, a point charge should correspond to the source current $J_\tau = \delta^3(x)$. Instead, we take $J_\tau(x) = \delta^3(x) - \frac{1}{2\pi^2}$ which has a point charge at $x = 0$ but is neutral overall. If we linearly combine such charge densities to construct an overall neutral collection of point charges, the constant parts of the charge density will exactly cancel, but the phantom charges will be absent. The solution to Laplace's equation on the Euclidean cylinder with this current is

$$A_\tau^{\text{Eucl.}}(\alpha) = \frac{1}{4\pi^2}(\pi - \alpha)\cot\alpha + \text{constant} \tag{3.23}$$

where the constant is an overall energy which is not yet fixed. This same result was computed earlier in Ref. [123] by computing the transition amplitude by summing over classical paths, and performing an infinite sum of SU(2) characters.

The quantity $A_\tau(\alpha)$ in Eq. (3.23) is the scalar potential on the sphere due to one charge, assuming an overall neutral distribution. To calculate the total energy for two charges $q_1 = -q_2$

separated by a distance α_{12}, we can compute

$$E^{\text{Eucl.}}_{\text{pair}}(\alpha_{12}) = \frac{1}{2}\int_{\Omega_3}(\vec{E}_1 + \vec{E}_2)^2, \tag{3.24}$$

where $\vec{E}_{1,2} = \vec{\nabla}(qA_\tau)_{1,2}$ is the electric field due to each charge. Integrating by parts, using the equations of motion, and throwing away the infinite self-energy of each charge, this is just

$$E^{\text{Eucl.}}_{\text{pair}}(\alpha_{12}) = q_1 q_2 A_\tau(\alpha_{12}) + \text{constant}. \tag{3.25}$$

Already, the reader may recognize $E^{\text{Eucl.}}_{\text{pair}}(\mathcal{A})$ as the α-dependent part of the cusp anomalous dimension in Euclidean space.

The equivalent of this calculation in AdS gives

$$E_{\text{pair}}(\beta_{12}) = \frac{q_1 q_2}{4\pi^2}\Big[(\pi + i\beta_{12})\coth\beta_{12} + C\Big]. \tag{3.26}$$

Here C is an undetermined constant setting the zero of energy, which must be fixed by other considerations. When both Wilson lines are outgoing, as in the process $e^+e^- \to q\overline{q}$, β_{12} is real and positive. At small β, the charges become closer than the curvature scale, and the energy reduces to

$$E_{\text{pair}}(\beta_{12}) \to \frac{q_1 q_2}{4\pi}\frac{1}{\beta_{12}}. \tag{3.27}$$

This is the correct behavior of the energy of two charges as a function of geodesic separation. Unfortunately, setting $\beta = 0$ is singular, so this limit cannot be used to determine the constant C.

When one Wilson line is outgoing and one is incoming, as in DIS, there is a smooth limit to zero separation which can be used to fix C. In this configuration, the quantity $\gamma = \beta - i\pi$ is real. Expressing the energy in terms of γ_{12}, we obtain

$$E_{\text{pair}}(\gamma_{12}) = i\frac{q_1 q_2}{4\pi^2}(\gamma_{12}\coth\gamma_{12} - iC). \tag{3.28}$$

In this case, the limit $\gamma_{12} = 0$ is physical: it corresponds to our two Wilson lines reducing to a single straight line going from $t = -\infty$ to $t = +\infty$ through the origin. This contour has no cusp

and is in fact a conserved current (occurring in the Isgur-Wise function [128]), so its anomalous dimension must vanish. This determines the boundary condition $E_{\rm pair}(\gamma_{12}=0)=0$, which sets $C=-i$.

In summary, restoring the color factors, charges, and coupling constant for QCD, and summing over pairs of charges to compute the total energy, we have found

$$E_{\rm tot}=\frac{i\alpha_s}{\pi}\sum_{i<j}\boldsymbol{T}_i\cdot\boldsymbol{T}_j\Big[(\beta_{ij}-i\pi)\coth\beta_{ij}-1\Big]\,. \tag{3.29}$$

Taking into account the factor of i in going from the energy to the anomalous dimension, Eq. (3.17), this implies

$$\Gamma=-\frac{\alpha_s}{\pi}\sum_{i<j}\boldsymbol{T}_i\cdot\boldsymbol{T}_j\left((\beta_{ij}-i\pi)\coth\beta_{ij}-1\right) \tag{3.30}$$

which agrees exactly with the anomalous dimension extracted from the one-loop calculation, Eq (3.8). Thus, we have reproduced **feature 2** in the introduction with a simple classical calculation. Note that with nontrivial color factors, the energy of the state in AdS corresponding to the Wilson line operators becomes a matrix on the space of Wilson lines $\mathcal{W}$ described in Eq. (3.3). This is a manifestation of the state-operator correspondence in conformal field theory [129].[3]

Before moving on to the other **features**, it is interesting to think about the "wrong" solution, Eq. (3.20) in AdS. On the sphere, the wrong solution had phantom charges on the antipoles. The location of these phantoms on AdS are shifted from the location of the physical charges by $\beta_{ij}^{\rm phant.}=\beta_{ij}-i\pi$. That is, the phantom is an initial state parton pointing in same direction as the outgoing one. So, for example, if we were trying to calculate $e^+e^-\to\overline{q}q$, the wrong solution would have corresponded to forward (non)scattering in $\overline{q}q\to\overline{q}q$, depicted in Figure 3.4(b). In contrast to the $e^+e^-\to\overline{q}q$, this process has a smooth limit in which the S matrix is just $\mathbb{1}$.

That there is a smooth limit $\gamma\to 0$ with one incoming and one outgoing Wilson line but

[3] In radial quantization, the operators $\mathcal{W}(n_i)$ with different t_{c_i} map to states in the Hilbert space $\mathcal{I}$ with a Hamiltonian given by Eq. (3.29). One usually considers the state-operator correspondence for local operators, which map to the states on AdS or S^3, depending on the signature. In the presence of Wilson lines in the τ-direction, the Hilbert space changes $\mathcal{H}_{\rm AdS}\to\mathcal{H}_{{\rm AdS},\mathcal{W}}$, and we can think of $\mathcal{I}$ in Eq. (3.4) as the space of lowest-lying states in $\mathcal{H}_{{\rm AdS},\mathcal{W}}$. Interpreting the Wilson lines as infinitely-massive charged particles, $\mathcal{I}$ is the space of lowest energy "bound states" of these particles, and the anomalous dimension measures the finite energy differences between different bound states. Additional local operators would map to excitations on top of the states in $\mathcal{I}$.

not $\beta \to 0$, with two outgoing or two incoming Wilson lines is closely related to **feature 3** from the introduction, concerning the complexity of the anomalous dimension. The anomalous dimension is real in DIS, since there is no obstruction to flattening the cusp. In the $e^+e^- \to$ dijets case, one cannot remove the cusp for any geodesic separation – the anomalous dimension has an $i\pi$ for any β. For a single log, the $i\pi$ in the anomalous dimension can be seen to come from $\ln\left(-\frac{\mu^2}{n_i\cdot n_j}\right)$, whose real part is the same as $\ln\left(\frac{\mu^2}{n_i\cdot n_j}\right)$. For a double log,

$$\mathrm{Re}\left[\ln^2\left(-\frac{\mu^2}{n_i\cdot n_j}\right)\right] = \mathrm{Re}\left[\ln^2\left(\frac{\mu^2}{n_i\cdot n_j}\right)\right] - \pi^2\,. \tag{3.31}$$

These π^2 terms get exponentiated leading to large factors of $e^{-\alpha_s\pi^2}$ in cross sections. In fact, this factor is a significant part of the large $\sim 2-3$ K-factors in Higgs or Drell-Yan production at the LHC [109, 130–133]. Roughly, $\sigma_{\rm NLO} = \sigma_{\rm LO}\exp\left(\gamma_{\rm cusp}(\alpha_s)C_A\pi^2\right) \sim 3\sigma_{\rm LO}$, where the $C_A = 3$ factor comes from these being gg initial states at the LHC, and at leading order $\gamma_{\rm cusp}(\alpha_s) = \frac{\alpha_s}{\pi} \sim 0.04$. The AdS picture gives us a way to visualize the situations, like DIS, where the anomalous dimension is real and situations like Drell-Yan, where it is complex. Note that, for most processes, the anomalous dimension is a matrix, with some real and some imaginary parts, so this picture is not tremendously useful in general.

Next, we observe that since the Coulomb potential does not get radiative corrections in QED (without propagating fermions), the anomalous dimension derived with energies in AdS is also one-loop exact. This implies that the anomalous dimension of a configuration with two Wilson lines is 1-loop exact in QED, which is equivalent to Abelian exponentiation which was **feature 4**. This same reasoning applies to the potential for N charges in QED. This classical proof of Abelian exponentiation is more intuitive than the conventional proof [134] which dissects the relevant Feynman diagrams through repeated use of the eikonal identity and careful consideration of diagrammatic combinatorics.

Beyond Abelian exponentiation, there are results about non-Abelian exponentiation [135, 136], including recent generalizations to multijet Wilson lines [137, 138]. Non-Abelian exponentiation is not as constraining as Abelian exponentiation, but it does imply that only a reduced set of web diagrams contribute in perturbation theory. There are also intriguing results on the exponentiation properties of Wilson lines for quantum gravity [139–141]. It is natural to expect

that there should be a way to understand these results using the AdS language as well, but we leave this for future consideration.

3.3 One-loop results

For the anomalous dimension at 1-loop, all that is needed is the classical Coulomb energy between two charges, as calculated in section III. It is helpful to see how this calculation connects directly to the field theory calculation using propagators, which will also set up the discussion of conformal gauge and 2-loop results in the next sections. We will perform most of our calculations in the DIS case, where the cusp angle $\gamma = \cosh^{-1}(-n_1 \cdot n_2)$ is real, since that simplifies many of the expressions. We will also use γ in place of β in our AdS coordinates.

The classical Coulomb potential $A_\tau(x)$ can be calculated using the AdS propagator via

$$A_\mu(x) = -i \int d^4y D_{\mu\nu}(x,y) J^\nu(y) \tag{3.32}$$

with the current $J^\nu(y)$ of a static charge. Putting the charge at the origin we set $J^\tau(y) = \delta^3(y)$ and $\vec{J}(y) = \vec{0}$, and we have

$$A_\tau(\tau,\gamma) = -i \int_{-\infty}^{\infty} d\tau' D_{\tau\tau}(\tau,\gamma;\tau',0). \tag{3.33}$$

In Minkowski space $\mathbb{R}^{1,3}$ the position space Feynman propagator is

$$D^F_{\mu\nu}(x,y) = \frac{1}{4\pi^2}\frac{g^{\mu\nu}}{(x-y)^2}. \tag{3.34}$$

Projecting onto the τ direction, this becomes

$$D^F_{\tau\tau}(x,y) = D^F_{\mu\nu}(x,y)\frac{\partial x^\mu}{\partial \tau}\frac{\partial y^\nu}{\partial \tau} = \frac{1}{4\pi^2}\frac{x\cdot y}{(x-y)^2}. \tag{3.35}$$

Finally, taking $x = e^\tau(-\cosh\gamma, -\sinh\gamma, 0, 0)$ and $y = e^{\tau'}(1,0,0,0)$, we find

$$D^F_{\tau\tau} = -\frac{1}{8\pi^2}\frac{\cosh\gamma}{\cosh(\tau-\tau')+\cosh\gamma}, \tag{3.36}$$

so that

$$A_\tau(\tau,\gamma) = -i\int_{-\infty}^{\infty} d\tau' D^F_{\tau\tau} = \frac{i}{4\pi^2}\gamma\coth\gamma. \tag{3.37}$$

Which is the same result we found in the previous section Eq. (3.28), up to an undetermined additive constant. We can again fix the constant by specifying which energy we mean by matching to the case of a conserved current with $\gamma = 0$, to get $\gamma\coth\gamma - 1$.

The propagator calculation lets us connect the energy directly to the anomalous dimension. Consider the 1-loop calculation with the gluon exchanged between the two Wilson lines. In position space, the integral is

$$I = \frac{g^2}{(4\pi)^2}\int_\infty^0 ds\int_0^\infty dt\frac{n_1\cdot n_2}{(sn_1 - tn_2)^2} \tag{3.38}$$

Pulling out the overall scale and changing to radial coordinates via $t = se^\tau$ this becomes

$$I = \frac{g^2}{2(4\pi)^2}\int_0^\infty \frac{ds}{s}\int_{-\infty}^\infty d\tau\frac{\cosh\gamma}{\cosh\tau + \cosh\gamma} \tag{3.39}$$

where we have used $\cosh\gamma = -n_1\cdot n_2$ as usual. The first integral is scaleless, resulting from the fact that our configuration of Wilson lines is rescaling-invariant. In general, one must break rescaling invariance with UV and IR regulators, and carefully extract the coefficients of the UV divergences to compute the anomalous dimension. However at 1-loop, we can be more cavalier. With regulators in place $\int\frac{ds}{s}$ will become $\log\frac{\Lambda_{\rm UV}}{\Lambda_{\rm IR}}$, so that the 1-loop anomalous dimension is simply the coefficient of this scaleless integral. This is precisely Eq. (3.29), the energy of the charges in AdS, as expected. In the field theory calculation the -1 factor that appears in the energy is correctly reproduced by the self-energy graphs for $n_i^2 \neq 0$. This calculation makes the connection transparent at the level of the integrals.

3.4 Lightlike limit

In this section, we consider the lightlike limit $n_i^2 \to 0$ which was the subject of **feature 5**. In this limit the static sources on the AdS space (corresponding to the Wilson lines) move towards the boundary of AdS, $\gamma_{ij}\to\infty$ or $\beta_{ij}\to\infty$. The anomalous dimension becomes linear in the cusp angles, which diverge as $\beta_{ij}\to\infty$ or $\gamma_{ij}\to\infty$. Equivalently, the imaginary part of the

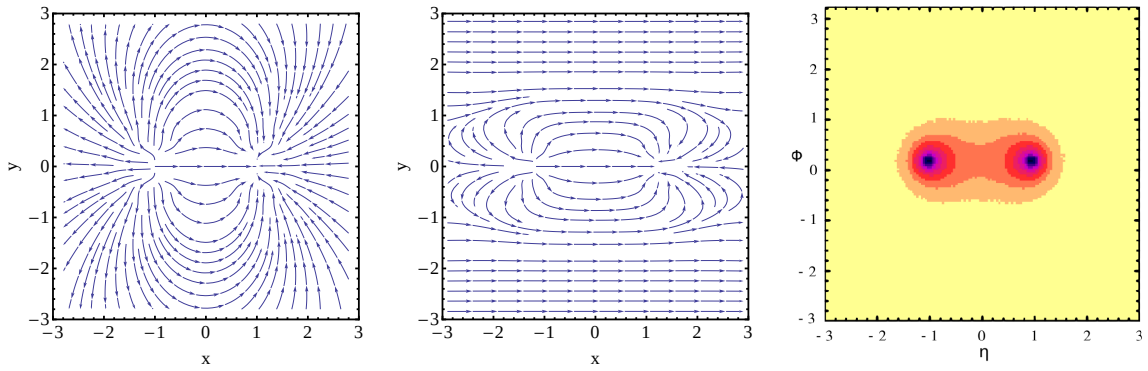

Figure 3.5: On the left is the electric field lines for two charges in flat space. The middle shows the imaginary part of the electric field for two charges in AdS, after projecting to rectangular coordinates with $x = \beta \sin\theta$ and $y = \beta\cos\theta$. The right (from [46]), shows the distribution of radiation from a color singlet scalar decaying to two jets at the LHC. The axes in this case are psuedorapidity and azimuthal angle, and the contours correspond to factors of two in the accumulated energy distribution. The rightmost plot is included to remind the reader that a color dipole radiates between the color charges, which roughly corresponds to the region where the energy density has support in the AdS picture. The sharp drop-off of the radiation pattern in the effect of color coherence. In a qualitative sense only, this corresponds to the exponential decay of the radiation away from the dipole axis in the AdS picture.

energy becomes linear in the geodesic distance between the charges, while the real part goes to a constant (see Eq. (3.28)). This is a qualitatively very different behavior from flat space, where the energy vanishes as the inverse of the distance.

If we try to actually set $n_i^2 = 0$, the cusp angle is infinite and the energy is formally infinite, indicating new unregulated singularities. The linearly diverging cusp angle is connected to the appearance of additional collinear divergences that appear in both the ultraviolet and infrared in the anomalous dimension computation. Effectively in the computation of matrix elements of $\mathcal{W}$ we are forced to introduce a small dimensionful IR regulator Λ. With UV divergences regulated in dimensional regularization the dimensions are compensated by μ, so $1/|n| \to \Lambda/\mu$, giving the form in Eq. (3.11). Introducing Λ/μ is equivalent to moving light-like charges away from the boundary of AdS, so that we can still sensibly talk about the geodesic distance between charges. The dependence on the IR regulator cancels out in physical cross section computations. For example, eikonal scattering involves a square of $\mathcal{W}$ matrix elements which yields the soft function $S(k)$ in Eq. (3.6). In this case the IR divergences cancel between virtual and real emission diagrams and Λ is replaced by the observed momenta of particles, $\Lambda \to k$.

To secure a clearer physical picture of what this growing imaginary energy means, consider

the case of two outgoing lightlike partons, such as in dijet production. In Figure 3.5, we contrast the electric field of a normal pair of charges, in flat space, with the imaginary part of the electric field for two charges in AdS. As the total energy grows with separation, the electric field approaches a constant between the charges. Notice that in the presence of two opposite Abelian charges, $\mathrm{Im}(E)$ is always negative, as should be the case for the energy of an unstable state. Back in Minkowski space, this corresponds to a roughly constant density of radiation between the two charges. The third panel of Figure 3.5, shows this behavior in a Monte Carlo simulation [22]. To generate this distribution, a 200 GeV dijet event produced at 7 TeV center of mass energy at the LHC was simulated. The figure shows the accumulated energy distribution. Note that the radiation is concentrated between the two charges, and suppressed away from the dipole axis, just as the energy distribution is in AdS.

Linear growth of energy with separation is normally an indication of confining behavior. In this case, since the energy is imaginary, it is not confinement in the usual sense, but can still be interpreted as a type of confinement. In a sense, this linear growth of the (imaginary) energy with separation is related to the fact that high energy quarks always appear with an accompanying jet, whose dynamics are described with Sudakov factors. Although this "Sudakov confinement" of quarks inside jets has little in common with confinement in QCD, it is not an unreasonable phrase for the linearly growing energy in AdS.

To be specific, consider the case of one incoming and one outgoing Wilson line, as in deep-inelastic scattering (DIS). In DIS, an electron is scattered off of a proton, with Bjorken x defined in terms of the momentum transfer q^μ and the proton momentum P^μ as $x = -q^2/2P \cdot q$. In the $x \to 1$ limit of DIS at large $Q^2 = -q^2$, the outgoing radiation becomes jet-like, with its mass $m_J^2 = Q^2(1-x)/x$ getting small. In this limit, the Wilson line description applies and important physics is encoded in the anomalous dimension. We saw that when Wilson lines becomes lightlike, the cusp angle $\gamma_{12} \to \infty$ and the energy in AdS becomes

$$E_{\mathrm{tot}} \to i\frac{\alpha_s}{\pi}\gamma_{12} \tag{3.40}$$

which is an imaginary energy.

An imaginary energy is indicative of non-unitary time evolution. Since time in AdS is scale

in Minkowski space, this is non-unitary evolution as the scale is changed. One way to think of the violation of unitary is going from a simple state, with say a single quark, to a state with a quark and a gluon. The probability for this to happen is given by the Alterelli-Parisi splitting kernels. The quark-gluon splitting kernel is

$$P_{q\to qg}(z, p_T) = \frac{\alpha_s}{\pi}\frac{1+z^2}{1-z}\frac{1}{p_T} \tag{3.41}$$

where z is the fraction of energy in the quark, which must be close to 1 (the Wilson line picture only applies in the $x \to 1$ limit) and p_T is the transverse momentum of the gluon with respect to the quark direction. The integral over this splitting function is infrared divergent. Typically, one imagines the quark starts off at a scale $\mu \sim Q$ characteristic of the hard scattering; then it evolves down to a scale $\mu \sim p_T$ [34, 35]. The probability of not having emitted a gluon between these scales is

$$\Sigma(Q, p_T) = \exp\left(-\int_{p_T}^{Q} \mathrm{d}\mu \int_{Q/\mu}^{1} \mathrm{d}z\ P(1-z,\mu)\right) = \exp\left(-\frac{\alpha_s}{\pi}\ln^2\frac{Q}{p_T} + \ldots\right). \tag{3.42}$$

This quantity is known as a Sudakov factor. It is a no-branching probability, and used as a classical probability in Monte Carlo event generators, which treat the parton as showering off gluons through a Markov process, see for example [22]. The rate of emission is exactly proportional to the coefficient of linear growth of the energy in AdS, a quantity known as the *cusp anomalous dimension*.

So we see that the non-unitary evolution corresponds to the probability that an off-shell quark decays into a gluon and a slightly less off-shell quark. The constant energy density in AdS at large cusp angle corresponds to a constant probability for emission per unit scale. If we evaluate the Sudakov factor at $p_T = 0$, we see that there is zero probability for a quark to evolve forever without emitting a gluon. In physical situations, there is always a finite IR cutoff, such as the hadronization scale Λ_{QCD} or a resolution scale for the jet. Nevertheless, at late times in AdS, or small momentum scales in Minkowski space, the original state approaches zero amplitude. Thus, there is no probability that we will find a free quark at asymptotically late times when produced at a finite scale Q. In other words, there are no free quarks which are not confined within jets. In fact, the characteristic size of jet is precisely determined by the

cusp anomalous dimension in the Sudakov factor.

It would be interesting to further explore the analogy between confinement and the linear growth of (imaginary) energy with distance. For example, one might argue that the energy can grow at most linearly with separation [142], as expected from the string flux tube picture. The analogy would connect this directly to Sudakov confinement and the linear dependence of the anomalous dimensions on $\log \mu$ for various fields in scattering processes. Then, perhaps, by reversing the logic, the Sudakov factors could give insight to confining gauge theories from the study of jets.

3.5 Conformal gauges

We have seen that radial quantization is a useful picture for understanding the one-loop cusp anomalous dimension. In $\mathbb{R} \times \text{AdS}$, a cusp maps to a collection of charges, and $\Gamma_{\text{cusp}}^{1-\text{loop}}$ has an interpretation in terms of static potentials. It makes sense that for higher-loop computations, we should keep the separation between the τ direction and the AdS directions manifest. However, this is not done in typical calculations. The reason is that although the action S_{YM} is conformally invariant, the *gauge-fixing terms* are not. For example, in Feynman gauge, we have

$$\begin{aligned} S =& S_{\text{YM}} + S_{\text{g.f.}}, \\ S_{\text{g.f.}} =& \int \mathrm{d}^4x \sqrt{-g} \frac{1}{2} (\nabla^\mu A_\mu)^2 + S_{\text{ghost}}. \end{aligned} \tag{3.43}$$

Under a conformal rescaling $g_{\mu\nu} = e^{2\omega} g'_{\mu\nu}$, the covariant derivative transforms nontrivially,

$$\sqrt{-g} (\nabla^\mu A_\mu)^2 = \sqrt{-g'} (\nabla'^\mu A_\mu + 2\partial^\mu \omega A_\mu)^2. \tag{3.44}$$

Consequently, a gauge that appears natural in one conformal frame may look somewhat unnatural in another. For instance, a useful feature of Feynman gauge in flat Minkowski space is that the propagator does not mix different polarizations between different points: $\varepsilon^\mu \Pi_{\mu\nu} \propto \varepsilon_\nu$. However from the point of view of radial coordinates $(\tau, \beta, \theta, \phi)$, the Feynman gauge propagator transports polarizations from one point to another in a nontrivial way. More precisely, transport via the propagator is not proportional to parallel transport in the $\mathbb{R} \times \text{AdS}$ metric. This is clear

from the transformation law (3.44): plugging in $g_{\mathbb{R}^{1,3}} = e^{2\tau} g_{\mathbb{R}\times \mathrm{AdS}}$, we see that $S_{\text{g.f.}}$ includes kinetic mixing between A_τ and the spatial components A_i. Throughout this section, we will use $i = 1, 2, 3$ to denote the directions in AdS.

It is informative to look at the explicit form of the mixing. To decompose the propagator, first observe that the τ component of the propagator comes from projections onto $\frac{\partial x^\mu}{\partial \tau} = x^\mu$. So that $D_{\tau\nu} = x^\mu D_{\mu\nu}$. Thus we can decompose the polarization $g^{\mu\nu}$ in the numerator of the Feynman propagator as

$$\begin{aligned} g^{\mu\nu} =& \left[g^{\mu\nu} - \hat{x}^\mu \hat{x}^\nu - \hat{y}^\mu \hat{y}^\nu + (\hat{x}\cdot\hat{y})\hat{x}^\mu \hat{y}^\nu\right] + \left[(\hat{x}\cdot\hat{y})\hat{x}^\mu \hat{y}^\nu\right] \\ &+ \left[\hat{x}^\mu \hat{x}^\nu + \hat{y}^\mu \hat{y}^\nu - 2(\hat{x}\cdot\hat{y})\hat{x}^\mu \hat{y}^\nu\right], \end{aligned} \tag{3.45}$$

where $\hat{x} = x^\mu/|x|$ and $\hat{y} = y^\mu/|y|$. The first term in brackets vanishes when contracted with x^μ or y^ν, so it represents the spatial components of the Feynman gauge propagator from the point of view of AdS, i.e. D_{ij}. This can also be seen by writing it as

$$g^{\mu\nu} - \hat{x}^\mu \hat{x}^\nu - \hat{y}^\mu \hat{y}^\nu + (\hat{x}\cdot\hat{y})\hat{x}^\mu \hat{y}^\nu = |x||y| \frac{\partial}{\partial x_\mu} \frac{\partial}{\partial y_\nu} \left(\frac{x\cdot y}{|x||y|}\right), \tag{3.46}$$

which vanishes when contracted with x_μ or y_ν since the dilation operator $\mathcal{D} = x^\mu \partial_\mu$ automatically annihilates any scale-invariant function. The second term in Eq. (3.45) is $D_{\tau\tau}$, as in Eq. (3.36). The third term represents the nonzero $D_{\tau i}$ and $D_{i\tau}$ mixing present in Feynman gauge.

Since the Wilson lines only source A_τ, at one-loop only the $D_{\tau\tau}$ component of the propagator contributes. If we try to use the same propagator in higher-loop computations, even though the Wilson lines only source A_τ, due to the $D_{\tau i}$ mixing terms, there will be interactions involving $(A_i)^3$ vertices which make the calculations complicated. However, we have seen that anomalous dimensions of Wilson lines are most naturally thought about from the point of view of $\mathbb{R}\times\mathrm{AdS}$. In a gauge more suited to this space there should be no mixing, and A_τ can be treated as a charged scalar. Since there is no scalar cubic or quartic vertex $(A_\tau)^{3,4}$ in Yang-Mills theory, the calculation will be significantly simpler. Vertices $(A_i)^2 A_\tau$ remain active when we consider Wilson line operators in this gauge and enter for the leading vacuum polarization effects.

We will refer to gauges with the property that A_τ and A_i do not mix as *conformal gauges*, to

emphasize the fact that they are most natural in a different conformal frame from the usual one. This non-mixing is not an overly restrictive condition and there are many gauges that satisfy it (for example, the condition remains true after any τ-independent gauge transformation). Perhaps the simplest example of a conformal gauge is temporal gauge in $\mathbb{R}\times\mathrm{AdS}$, or equivalently "radial gauge" in $\mathbb{R}^{1,3}$, in which $A_\tau = x^\mu A_\mu = 0$ and radial Wilson lines are actually trivial. We will briefly discuss this gauge in Section 3.5.2. In Sec. 3.5.1 we will focus on a less singular example of conformal gauge, which corresponds to a quantum average over different gauge-conditions, as in R_ξ gauges.

3.5.1 Derivation of Conformal Gauge in d-dimensions.

To arrive at a conformal gauge, perhaps the most familiar strategy would be to study gauge-fixing terms in $\mathbb{R}\times\mathrm{AdS}$, and then invert the kinetic terms to form the corresponding propagators. This might be an interesting exercise, but it would be needlessly complicated for our purposes. Instead, we will adopt the more pragmatic procedure of directly gauge-transforming the Feynman-gauge propagator and solving for the transformation function that gives the desired properties. This then implicitly specifies BRST exact gauge-fixing terms, including a ghost action.

Our goal is to derive a gauge that has no τ-i mixing in d-dimensions that is suitable for use in dimensional regularization. Our procedure is simple, and powerful enough to handle this even though Yang-Mills theory is only classically conformally invariant when $d = 4$. Instead of sorting out details of conformal anomalies at order ε, we will keep the d-dimensional Minkowski metric and flat coordinates x_μ, and simply search for a gauge that respects the foliation of $\mathbb{R}^{1,d-1}$ into $\mathbb{R}\times\mathrm{AdS}_{d-1}$. Precisely when $d = 4$, our propagator will have an interpretation as the propagator in a gauge theory on $\mathbb{R}\times\mathrm{AdS}_3$. However when ε is nonzero, it will simply be a useful tool that enables computations to be performed without encountering mixing terms $D_{\tau i}$ or $D_{i\tau}$ in d-dimensions.

We begin with the position-space Feynman propagator in d dimensions

$$D^F_{\mu\nu}(x,y) = -g_{\mu\nu}\,\frac{\kappa_d}{[-(x-y)^2+i\epsilon]^{d/2-1}} \tag{3.47}$$

where $\kappa_d = \frac{\Gamma(d/2-1)}{4\pi^{d/2}}$ is a constant. Since the propagator depends only on quadratic terms in the action, it is sufficient for our discussion here to consider an Abelian theory. In a non-Abelian theory, the propagator should also include a factor of the identity δ^{ab} in color space, and we have the additional Feynman rules involving ghosts which we discuss in Appendix B.2.

We will consider a class of propagators given by

$$D_{\mu\nu}(x,y) = D^F_{\mu\nu}(x,y) + \frac{\partial}{\partial y^\nu}\Lambda_\mu(y,x) + \frac{\partial}{\partial x^\mu}\Lambda_\nu(x,y), \tag{3.48}$$

where $\Lambda_\mu(y,x)$ is a one-form at x, depending on both x and y. Notice that $D_{\mu\nu}$ is still an inverse for the kinetic term in the space of gauge equivalence-classes, though it differs from $D^F_{\mu\nu}$ along gauge-orbits. Indeed, suppose J^μ is a conserved current, and consider the associated vector potential

$$\begin{aligned} A_\mu(x) &\equiv -i\int \mathrm{d}y\, D_{\mu\nu}(x,y)J^\nu(y) \\ &= -i\int \mathrm{d}y\, D^F_{\mu\nu}(x,y)J^\nu(y) + \frac{\partial}{\partial x^\mu} \leftrightarrow (-i\int \mathrm{d}y\, \Lambda_\nu(x,y)J^\nu(y)) \\ &= A^F_\mu(x) + \partial_\mu \leftrightarrow (-i\int \mathrm{d}y\, \Lambda_\nu(x,y)J^\nu(y))\,, \end{aligned} \tag{3.49}$$

where we have integrated by parts and used current conservation. Since A_μ differs from A^F_μ only by a gauge transformation, it still solves Maxwell's equation $\partial_\mu F^{\mu\nu} = J^\nu$.

We would like $D_{\tau i}$ to vanish, so that the propagator does not mix time and space directions in $\mathbb{R}\times\mathrm{AdS}$. Recalling that τ is the generator of scale transformations, $\partial_\tau = x^\mu\partial_\mu$, a vector field $A_\mu(y)$ will have no τ component if $y^\mu A_\mu(y) = 0$. Thus our condition is

$$x^\mu D_{\mu\nu}(x,y)A^\nu(y) = 0 \qquad \text{whenever} \qquad y_\nu A^\nu(y) = 0. \tag{3.50}$$

Likewise, for $D_{i\tau}$ to vanish we have the condition $A^\mu(x)D_{\mu\nu}(x,y)y^\nu = 0$ whenever $x_\mu A^\mu(x) = 0$. Note that Eq. (3.50) is not translation invariant, it treats the origin as a special point and yields propagators that are not simply functions of $x-y$.[4] The general class of conformal gauges which

[4] In our setup the origin is special since it is the location of our hard interaction and the place where cusps occur between Wilson lines. This explains why it is useful to consider non-translationally invariant gauges, even though the final physical results are gauge independent and translationally invariant.

satisfy these no-mixing conditions is derived in Appendix B.1. Here let us consider the ansatz

$$\Lambda_\mu(y,x) = \kappa_d \frac{x_\mu}{|x|^{d-2}}\, g(\mathcal{A},\beta), \qquad \text{where} \quad \mathcal{A} \equiv \frac{x\cdot y}{|x||y|},\ \beta \equiv \frac{|y|}{|x|}, \tag{3.51}$$

and $g(\mathcal{A},\beta)$ is some function to be determined. Equation (3.50) implies

$$\begin{aligned} \frac{\partial}{\partial \mathcal{A}} g(\mathcal{A},\beta) &= \beta(2\mathcal{A}\beta - \beta^2 - 1)^{1-d/2} \\ g(\mathcal{A},\beta) &= \frac{1}{4-d}\Big[(2\mathcal{A}\beta-\beta^2-1)^{2-d/2} - f(\beta)^{2-d/2}\Big], \end{aligned} \tag{3.52}$$

where $f(\beta)$ is arbitrary and its $2-d/2$ power produces the correct $d\to 4$ solution. Our ansatz becomes

$$\Lambda_\mu(y,x) = \frac{\kappa_d}{4-d}\,\frac{x_\mu}{x^2}\Big\{[-(x-y)^2]^{2-d/2} - |x|^{4-d} f(\beta)^{2-d/2}\Big\}. \tag{3.53}$$

The conformal gauge propagator is then

$$\begin{aligned} D_{\mu\nu}(x,y) = &-\frac{\kappa_d}{[-(x-y)^2]^{d/2-1}}\Big(g_{\mu\nu} - \frac{x_\mu x_\nu}{x^2} - \frac{y_\mu y_\nu}{y^2} + \frac{2x_\mu (x\cdot y) y_\nu}{x^2 y^2}\Big) \\ &+ \kappa_d \frac{x_\mu y_\nu}{x^2 y^2}\Big\{[-(x-y)^2]^{2-d/2} - \chi\big(|x|,|y|\big)^{4-d}\Big\} \end{aligned} \tag{3.54}$$

where $\chi(|x|,|y|)$ is any symmetric function of $|x|$ and $|y|$ with dimensions of length. (χ has a a simple but unenlightening relation to $f(\beta)$). Separating out the τ and spatial components, as in Eq. (3.45), this can be written

$$\begin{aligned} D_{\mu\nu}(x,y) = &-\frac{\kappa_d}{[-(x-y)^2]^{d/2-1}}|x||y|\partial^x_\mu \partial^y_\nu \leftrightarrow \big(\frac{x\cdot y}{|x||y|}\big) \\ &- \kappa_d \frac{x_\mu y_\nu}{x^2 y^2} \leftrightarrow \big(\frac{x\cdot y}{[-(x-y)^2]^{d/2-1}} - [-(x-y)^2]^{2-d/2} + \chi\big(|x|,|y|\big)^{4-d}\big). \end{aligned} \tag{3.55}$$

Here the first term is manifestly "angular", involving derivatives acting on a scaleless quantity which vanish when contracted with x^μ or y^ν, as in Eq. (3.46). The second term is "radial", involving projection onto the τ-direction with x_μ and y_ν. The mixing terms have been gauged away, as desired.

A natural choice is to take χ to be d-independent. Then when $d=4$ the last two terms of Eq. (3.55) cancel, χ drops out, and we have a unique 4D propagator. In fact, this propagator is

identical to the Feynman propagator in 4D, Eq. (3.36), without the mixing terms. In particular, the calculation of the Coulomb potential from a static charge in AdS, and hence the one-loop anomalous dimension of the Wilson line, is identical in Feynman gauge and in conformal gauge. We see that the entire content of this gauge fixing is to move the mixing terms in Feynman gauge into non-mixing terms starting at order ε.

Equation (3.55) is convenient for computations involving non-light-like Wilson lines in d-dimensions or with dimensional regularization. To consider propagation between points on two light-like Wilson lines we take $x^\mu = \lambda_1 n_1^\mu$ and $y^\mu = \lambda_2 n_2^\mu$, and take the limit $n_1^2 \to 0$ and $n_2^2 \to 0$. Here $n_1^\mu n_2^\nu D_{\mu\nu}(x, y)$ reduces to the same result as Feynman gauge in 4D. In d-dimensions the result in Eq. (3.55) is not convenient because the χ term does not scale in the same manner as the other terms in the radial part of the propagator. We derive an alternative conformal gauge with a good scaling limit for light-like Wilson lines in d-dimensions in Appendix B.1.

3.5.2 Comparison to radial gauge

In conformal gauge, the scalar modes in AdS, A_τ which are produced from the Wilson lines, have no mixing with the vector modes. This simplifies some loop calculations, as we will demonstrate in the next section. However, it is natural to ask why we cannot simplify things even further by choosing temporal gauge $A_\tau = 0$ in AdS. This condition becomes $x_\mu A^\mu(x) = 0$ in Minkowski space, and gauges satisfying it are called radial (or Fock-Schwinger) gauges. The origin is again a special point for these gauges and the gauge boson propagator is not translation invariant.

In radial gauge, our N-jet Wilson lines become trivial, and loop corrections to the expectation value $\langle \mathcal{W} \rangle$, and corresponding anomalous dimension, seem naïvely to vanish. Of course this is too simplistic to be correct. The problem is that an N-jet Wilson line operator $\mathcal{W}$ as defined in Eq. (3.3) is only invariant by itself under gauge transformations which vanish at infinity. However, the transformation from, say, Feynman gauge to radial gauge is nontrivial at infinity, so the expectation value $\langle \mathcal{W} \rangle$ can change. Indeed, in Ref. [143] it was shown that the radial gauge propagator $D_{\mu\nu}$ itself carries ultraviolet divergences.

To correctly compute the cusp anomalous dimension, we must either restrict ourselves to gauges with appropriate behavior at spatial infinity, or "close off" our Wilson loop in a gauge-invariant way at some large finite distance from the origin, without introducing additional cusps.

(Or with additional cusps whose contribution we then subtract away.) In the latter case, the cusp divergences are generated by a different part of the calculation. For example, using a conventional definition of radial gauge, Ref. [143] explicitly demonstrates that the classic one-loop $x = 0$ cusp anomalous dimension is correctly reproduced by the (smooth) "closed off" part of the Wilson loop. The fact that the radial gauge propagator itself is ultraviolet divergent plays a crucial role in this computation, since otherwise the closed off part of the loop would not contribute to the anomalous dimension.

To avoid having these complications, we will focus on conformal gauges that do not have ultraviolet divergences in $D_{\mu\nu}$. This was true of our construction in Sec. 3.5.1, where $D_{\mu\nu}$ in Eq. (3.55) is finite as $d \to 4$, and divergences occur only when interaction points approach each other. In the limit $(x-y)^2 \to 0$, with both $x^2, y^2 \neq 0$, $D_{\mu\nu}$ approaches the usual Feynman propagator at leading order. Consequently, power counting shows that divergences originating near points away from the light-cone are identical in Feynman gauge and in our conformal gauge. (It would be useful to fully characterize the divergence and subdivergence structure of multi-loop diagrams in conformal gauge.) In these cases, the cusp anomalous dimension can be computed by considering only a neighborhood of the cusp.

3.6 Three Wilson Lines at Two-Loops

As a concrete application of using our conformal gauge, let us compute the two-loop contribution to the anomalous dimension of a multi-Wilson line operator Eq. (3.3) that involves all three lines. The absence of τ-i mixing makes this computation extremely simple, and elucidates the origin of the previously mysterious pairwise structure of the result, discussed as **feature 6**.

When the number N of jet directions is three or more, the anomalous dimension $\Gamma_{\text{cusp}}(n_i)$ can in principle depend on arbitrary combinations of the cusp angles γ_{ij}. Nontrivial combinations involving three γ_{ij}'s can appear first at two loops in the coefficient F of the "maximally non-Abelian" color structure $f^{abc}\boldsymbol{T}_i^a\boldsymbol{T}_j^b\boldsymbol{T}_k^c$,

$$\Gamma_{\text{cusp}}^{2-\text{loops}}(n_i) = \leftrightarrow \left(\frac{\alpha_s}{\pi}\right)^2 \leftrightarrow \left(\sum_{i<j} \boldsymbol{T}_i^a\boldsymbol{T}_j^a\, f(\gamma_{ij}) + \sum_{i<j<k} i f^{abc}\boldsymbol{T}_i^a\boldsymbol{T}_j^b\boldsymbol{T}_k^c\, F(\gamma_{ij},\gamma_{jk},\gamma_{ki})\right), \tag{3.56}$$

due to the presence of diagrams depicted in Figure (3.6). In particular the non-planar dia-

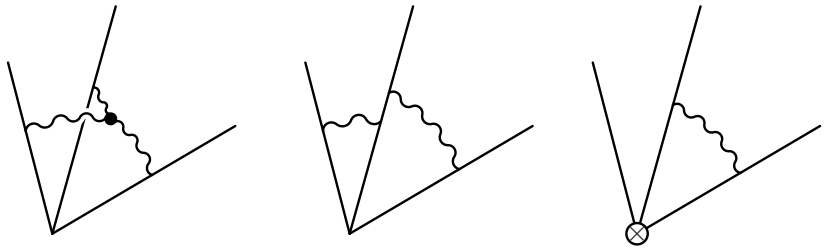

(a) nonplanar (b) planar (c) counterterm

Figure 3.6: 2-loop graphs contributing to the coefficient $F(\gamma_{ij}, \gamma_{jk}, \gamma_{ki})$ of the antisymmetric color structure in $\Gamma_{\text{cusp}}(v_i)$ (Eq. 3.56).

gram 3.6(a) could naïvely contribute a complicated function of all three cusp angles. The expression for this graph in Feynman gauge was discussed in the lightlike limit in [116] and [144], and analyzed numerically in [145]. It was finally computed for general cusp-angles in [146] in a somewhat technical computation using Mellin-Barnes representations. After all this, the final result turns out to be remarkably simple,

$$F^{(\text{a})}_{\text{Feyn.}} = -\frac{1}{2}(\gamma_{ij}\coth\gamma_{ij})\gamma_{jk}^2 + \text{antisym.} \tag{3.57}$$

where "antisym." stands for signed permutations of i, j, k. This is a sum of terms each of which only depends on two of the cusp angles.

It is less surprising that the planar and counterterm graphs also have a pairwise form. For the antisymmetric color structure, the result is [146]

$$\begin{aligned} F^{(b)}_{\text{Feyn.}} + F^{(c)}_{\text{Feyn.}} = \frac{1}{2}(\gamma_{ij}\coth\gamma_{ij}) \times \coth\gamma_{jk} \leftrightarrow (\gamma_{jk}^2 + 2\gamma_{jk}\log(1-e^{-2\gamma_{jk}}) - \text{Li}_2(e^{-2\gamma_{jk}}) + \frac{\pi^2}{6}) \\ + \text{antisym.}, \end{aligned} \tag{3.58}$$

When all the Wilson lines are lightlike, the sum of graphs actually vanishes in Feynman gauge, a result which is not immediately obvious. At large γ, the $-\frac{1}{2}\gamma_{ij}\gamma_{jk}^2$ asymptotic behavior of the non-planar amplitude in Eq. (3.57) is exactly canceled by contributions from Eq. (3.58).

Returning to the difficult non-planar graph, the simplicity of the final result $F^{(a)}_{\text{Feyn}}$ is easily understood from the AdS picture. In $\mathbb{R} \times \text{AdS}$, each Wilson line points in the time direction, and thus sources only the τ component of the gauge field. In conformal gauge A_τ does not mix with A_i, then the interaction vertex in 3.6(a) involves three τ-polarized gauge fields, and thus

vanishes identically. In this gauge, only the planar and counterterm diagrams contribute, and F naturally has a pairwise-factorized form. Note that one of the factors $(\gamma_{ji} \coth \gamma_{ij})$ looks just like $\Gamma_{\text{cusp}}^{1-\text{loop}}$. This is suggestive that the contribution of $F_{\text{Feyn}}^{(a)}$ should come from the counterterm graph in conformal gauge. We will shortly show that this is indeed the case.

Let us rephrase the above argument in a way that emphasizes the analogy with our one-loop computation in Section 3.2. Notice that each line in 3.6(a), thought of as a static charge in AdS, couples only to the τ-independent modes of the gauge field in $\mathbb{R} \times \text{AdS}$.[5] Thus, the computation of this graph "dimensionally reduces" from $\mathbb{R} \times \text{AdS}$ to AdS, with one overall τ-integral contributing a logarithmic divergence multiplying the anomalous dimension. The theory on AdS contains a scalar (coming from A_τ), and a three-dimensional gauge field. Each Wilson line sources the scalar, so diagram 3.6(a) becomes a three-point function of scalars in AdS. Finally, since there is no three-scalar interaction in the dimensional reduction of Yang-Mills theory, this correlator vanishes at leading order. The utility of conformal gauge is that it makes dimensional reduction in the τ-direction much simpler than it would be in Feynman gauge.

Having understood why $F(\gamma_{ij}, \gamma_{jk}, \gamma_{ki})$ should have a simple form, let us proceed to compute it using conformal gauge. Diagram 3.6(a) now vanishes, and the entire contribution comes from the planar and counterterm graphs. All Wilson lines point in the τ-direction, so we need only the radial part of the gauge-boson propagator which from Eq. (3.55) is:

$$D_{\mu\nu}^{(\tau\tau)}(x,y) = -\kappa_d \frac{x_\mu y_\nu}{x^2 y^2} \leftrightarrow \left(\frac{x \cdot y}{[-(x-y)^2]^{d/2-1}} - [-(x-y)^2]^{2-d/2} + \chi\big(|x|,|y|\big)^{4-d}\right). \tag{3.59}$$

The first term in parentheses is the same as $D_{\tau\tau}^F$ in Feynman gauge. The second and third terms are new.

Since we seek the coefficient of the antisymmetric color structure $f^{abc} T_i^a T_j^b T_k^c$, which does not arise at one-loop, the anomalous dimension is simply the coefficient of the $1/\varepsilon$ pole in the sum of diagrams 3.6(b) and 3.6(c). To separate UV and IR divergences, we must in general regulate the IR with something other than dimensional regularization. However, here we can safely ignore this subtlety since the entire divergence structure comes from a single scaleless integral, and it will be simple to isolate the associated UV divergence. We have checked that a

[5] This is not the case for diagrams involving more than one gluon emission from a single Wilson line.

more careful treatment of the infrared, for instance giving the Wilson lines some finite length, yields the same results.

To evaluate 3.6(b), let us first perform the integrals along the lines with only a single gluon emission. This gives the Coulomb potential from a single Wilson line, which we now need up to order ε. We have, with the normalization $n_1^2 = n_2^2 = 1$,

$$\begin{aligned}\int_0^\infty ds\, n_i^\mu n_j^\nu D_{\mu\nu}(sn_i, tn_j) &= \kappa_d(-1)^\epsilon \int_0^\infty \mathrm{d}s \left(\frac{-n_i \cdot n_j}{(sn_i - tn_j)^{2-2\epsilon}} + \frac{\chi(s,t)^{2\epsilon} - (sn_i - tn_j)^{2\epsilon}}{st} \right) \\ &= \kappa_d \frac{(-1)^\epsilon}{t^{1-2\epsilon}} \leftrightarrow (E_F^{(0)}(\gamma_{ij}) + \varepsilon E_F^{(1)}(\gamma_{ij}) + \varepsilon E_C^{(1)}(\gamma_{ij})) \end{aligned} \tag{3.60}$$

Here $E_F^{(0)} = A_\tau(\gamma_{ij})$ from Eq. (3.37) is just the scalar potential from a Wilson line in 4 dimensions:

$$E_F^{(0)}(\gamma) = \gamma \coth \gamma \tag{3.61}$$

$E_F^{(1)}$ is the next term in the ε expansion of this potential in Feynman gauge, also coming from the first term in the integral. It is

$$E_F^{(1)}(\gamma) = \coth \gamma \leftrightarrow (\gamma^2 + 2\gamma \log(1 - e^{-2\gamma}) - \mathrm{Li}_2(e^{-2\gamma}) + \frac{\pi^2}{6}) \tag{3.62}$$

Finally, $E_C^{(1)}$ is the new piece present in conformal gauge and not in Feynman gauge, from the second term in the integral in Eq. (3.60). It gives

$$\begin{aligned} E_C^{(1)}(\gamma_{ij}) &= \int_0^\infty \frac{\mathrm{d}s}{s} \log \frac{\chi(s,1)^2}{(n_i s - n_j)^2} \\ &= \int_{-\infty}^\infty \mathrm{d}\tau \log \left(\frac{\cosh \tau}{\cosh \tau + \cosh \gamma_{ij}} \right) + \int_0^\infty \frac{\mathrm{d}s}{s} \log \frac{\chi(s,1)^2}{1+s^2} \\ &= -\gamma_{ij}^2 - \frac{\pi^2}{4} + c_\chi \,. \end{aligned} \tag{3.63}$$

The constant c_χ is a gauge-dependent but γ-independent number which will cancel from the final result (and is exactly zero for $\chi(|x|,|y|) = \sqrt{x^2+y^2}$). Note that the asymptotic expansion of $E_C^{(1)}$ at large γ is $-\gamma^2$, which cancels the asymptotic expansion of $E_F^{(1)}$, leaving zero contribution to the antisymmetric color structure in the anomalous dimension for the light-like limit. Two loop graphs involving only two lines do contribute in the light-like limit, and give an energy

which grows linearly with the cusp angle.

With $\mathcal{O}(\varepsilon)$ parts of the scalar potential calculated, it is now easy to extract the antisymmetric part of the two-loop anomalous dimension. The counterterm and planar graphs can be combined into

$$\begin{aligned} I^{(b)} + I^{(c)} = \int_0^\infty \frac{\mathrm{d}t_1}{t_1^{1-2\varepsilon}} \Big[E_F^{(0)}(\gamma_{ij}) + \varepsilon E_F^{(1)}(\gamma_{ij}) + \varepsilon E_C^{(1)}(\gamma_{ij}) \Big] \\ \times \left\{ -\frac{1}{\varepsilon} E_F^{(0)}(\gamma_{jk}) + \int_0^{t_1} \frac{\mathrm{d}t_2}{t_2^{1-2\varepsilon}} \Big[E_F^{(0)}(\gamma_{jk}) + \varepsilon E_F^{(1)}(\gamma_{jk}) + \varepsilon E_C^{(1)}(\gamma_{jk}) \Big] \right\} + \text{antisym.} \end{aligned} \tag{3.64}$$

After antisymmetrizing, everything vanishes except for the cross term between the counterterm and the ε terms on the first line. Replacing the scaleless t_1 integral on the first line with $\frac{1}{2\varepsilon}$ as before, we see that these graphs sum to produce a contribution to the anomalous dimension of the form

$$\begin{aligned} F^{(b)} + F^{(c)} &= \frac{1}{2} E_F^{(0)}(\gamma_{ij}) \Big(E_F^{(1)}(\gamma_{jk}) + E_C^{(1)}(\gamma_{jk}) \Big) + \text{antisym.}, \\ &= \frac{1}{2} \gamma_{ij} \coth\gamma_{ij} \coth\gamma_{jk} \left(\gamma_{jk}^2 + 2\gamma_{jk} \log(1 - e^{-2\gamma_{jk}}) - \mathrm{Li}_2(e^{-2\gamma_{jk}}) + \frac{\pi^2}{6} \right) \\ &\qquad - \frac{1}{2} \gamma_{ij} \coth\gamma_{ij} \gamma_{jk}^2 + \text{antisym.} \end{aligned} \tag{3.65}$$

which precisely matches $F^{(a)} + F^{(b)} + F^{(c)}$ in Feynman gauge. The difficult non-planar graph was reproduced with a far simpler calculation involving the $\mathcal{O}(\varepsilon)$ parts of the conformal gauge propagator. Note that the gauge-dependent constant c_χ drops out due to the antisymmetrization.

For three light-like Wilson lines the calculation of the diagrams in Figure 3.6 can also be considered directly using a conformal gauge. To do this we should use the conformal gauge from Eq. (B.8), rather than the one in Eq. (3.55). This conformal gauge has no $D_{\tau i}$ or $D_{i\tau}$ mixing terms and is identical to Feynman gauge for $D_{\tau\tau}$ in d-dimensions. The lack of mixing terms immediately implies that Figure 3.6a is zero, a result that is only seen in Feynman gauge by direct computation [116]. For the remaining diagrams, Figure 3.6b and Figure 3.6c, the calculation is identical to the one in Feynman gauge, so the sum of these diagrams is zero just as it is there [116, 144].

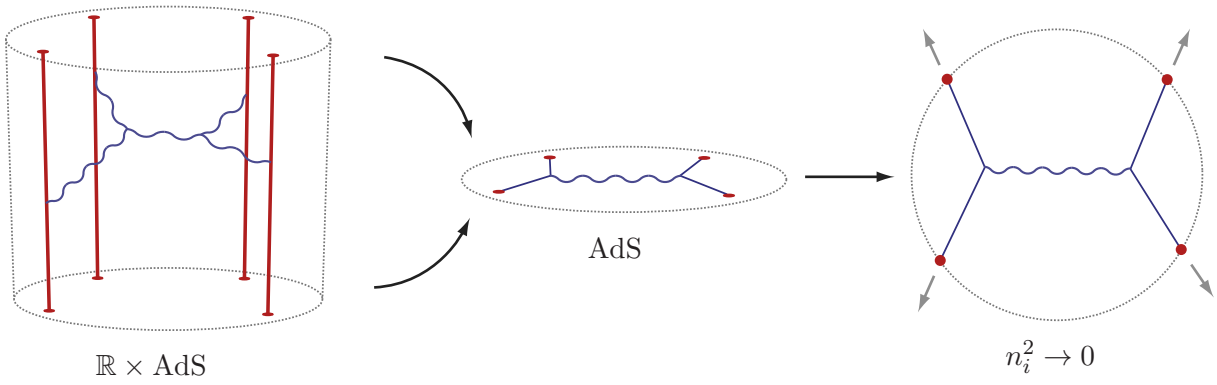

Figure 3.7: After doing all the τ-integrals, the computation of certain diagrams dimensionally reduces from $\mathbb{R} \times$ AdS to AdS. In the limit where the charges approach the boundary $n_i^2 \to 0$, we obtain a Witten diagram.

3.7 Relation to Witten Diagrams in the Lightlike Limit

Finally, let us comment on an interesting formal similarity between the perturbation expansion for $\Gamma_{\text{cusp}}(n_i)$ in the lightlike limit and the Witten diagram expansion for AdS scattering amplitudes, which has been well studied in the AdS/CFT literature [147–152]. Recall from the previous section that diagrams with at most one gluon attached to each line involve only τ-independent modes of the gauge field. After performing integrals in the τ-direction, they become AdS scattering amplitudes in a gauge theory containing an adjoint scalar, which is sourced by each charge. As the parton directions become lightlike $n_i^2 \to 0$, the corresponding charges move off to the boundary of AdS. We are left, at least formally, with a boundary-to-boundary scattering amplitude — a Witten diagram (Figure 3.7).

We could have anticipated some relation to Witten diagrams simply from the geometry. Our realization of AdS_3 as a hyperboloid inside $\mathbb{R}^{1,3}$ is known in the AdS/CFT literature as the *embedding space* (or sometimes *covering space*) formalism [153–158]. Its utility is that the isometries of AdS (and conformal transformations of its boundary) become linearly-realized Lorentz transformations of the embedding space, an observation that dates back to Dirac [153]. Here, we arrived at this formalism from the other direction, beginning in Minkowski space, and finding that AdS geometry appears naturally.

A possible correspondence between Feynman diagrams for $\Gamma_{\text{cusp}}(n_i)$ and Witten diagrams is complicated by several issues. Firstly, as we argued extensively in Section 3.2, choosing proper

boundary conditions in AdS is crucial for capturing the correct physics. For example, our scalar bulk-to-bulk propagator is the potential we computed in Eq. (3.26),

$$D_{BB}(n_1, n_2) = \frac{1}{4\pi^2} \leftrightarrow (\pi + i\beta_{12}) \coth \beta_{12}. \tag{3.66}$$

Recall that this solves Laplace's equation in the presence of a constant charge density, so does not correspond to the usual bulk-to-bulk scalar propagator, which solves the homogeneous Laplace's equation in AdS. In the limit that one of the directions n_1 becomes lightlike, we also obtain an unorthodox boundary-to-bulk propagator,

$$D_{\partial B}(n_1, n_2) = \lim_{|n_1|\to 0} D_{BB}(n_1, n_2) = \lim_{|n_1|\to 0} \frac{i}{4\pi^2} \leftrightarrow (-\log|n_1| + \log\frac{n_1 \cdot n_2}{|n_2|}) \tag{3.67}$$

This is divergent as $|n_1| \to 0$, a reflection of the collinear singularities that arise in this limit.[6]

Contributions to Γ also differ from traditional Witten diagrams in their contours of integration. For Witten diagrams, one performs bulk integrals over AdS, whereas Feynman integrals involve all of Minkowski space, so should incorporate both copies of AdS and dS as well (Figure 3.3).

To use Witten diagrams for computing Γ, one must account for all of the above issues. Nevertheless, the possible applicability of AdS amplitude technology is encouraging. Witten diagrams have been well-studied, and recently new techniques involving Mellin representations have substantially improved efficiency of computation [159–163].

As an example, the gauge-boson exchange diagram depicted in Figure 3.7 was first computed with traditional boundary conditions over a decade ago [150–152]. The answer is a nontrivial sum of so-called D-functions $D_{\Delta_1,\Delta_2,\Delta_3,\Delta_4}(u, v)$, where u and v are conformal cross-ratios. Formally, this diagram contributes to the regular anomalous dimension $\gamma(\mathcal{A}_s, \{n_i \cdot n_j\})$ in Eq. (3.12) at three-loops, with a color structure $f^{abe}f^{cde}\boldsymbol{T}_i^a\boldsymbol{T}_j^b\boldsymbol{T}_k^c\boldsymbol{T}_l^d$. While we have understood using conformal gauge why $\Gamma_{\text{cusp}}(n_i)$ should have a pairwise structure up to two-loops, we see no a

[6] Its form is perhaps reminiscent of the traditional boundary-to-bulk propagator for a scalar with an infinitesimal mass

$$D_{\partial B}(n_1, n_2) \overset{?}{\sim} \lim_{\Delta\to 0} \frac{i}{4\pi^2}\frac{1}{\Delta} \leftrightarrow (\frac{n_1 \cdot n_2}{|n_2|})^{\Delta} \tag{3.68}$$

where the mass is related to Δ via the usual AdS/CFT dictionary, $m^2 R_{\text{AdS}}^2 = \Delta(\Delta - 2)$. One might speculate that in a calculation where the $-\log|n_i|$ singularities are regulated and cancel appropriately, Eq. (3.68) might be an acceptable form for the boundary-to-bulk propagator.

priori reason that this structure should persist to higher orders. We interpret the fact that the diagram in Figure 3.7 is nonzero as an indication that $\gamma(\mathcal{A}_s, \{n_i \cdot n_j\})$ might very well have nontrivial conformal cross-ratio dependence. Very recently, two papers have appeared [121, 122] which propose that additional constraints on the conformal cross ratio dependence of the soft anomalous dimension follow from consideration of the Regge limit. Perhaps by using tools developed for Witten diagrams, the 3-loop anomalous dimension can be calculated exactly, hopefully resolving the controversy in **feature** 6.

3.8 Conclusions

In this paper we have discussed how properties of operators $\mathcal{W}$ built from N Wilson lines can be understood in radial coordinates. These operators appear in high energy collisions that produce jets, where the lines extend out from the location of the hard interaction, taken to be the origin. In radial coordinates, $\mathbb{R} \times$ AdS, the direction of the Wilson lines are specified by points in Euclidean AdS_3 and motion along any of the Wilson lines corresponds to time-translations of $\tau \text{in} \mathbb{R}$.

We have demonstrated that many of the key properties of anomalous dimensions of these operators have an intuitive and simple description in terms of these static charges in AdS. In particular: the dependence on cusp angles β_{ij} just corresponds to the geometric distance between the lines in AdS; the one-loop anomalous dimension of $\mathcal{W}$ is given by a classical energy computation on AdS (with special care given to boundary conditions).

There is an intuitive physical picture associated to the real and imaginary parts of the anomalous dimension. This picture leads to an intriguing analogy between the at most linear growth of imaginary energy with separation in AdS, guaranteed by the at most linear growth of the anomalous dimensions with cusp angles, and the linear dependence of energy on separation for charges in gauge theories, which is associated with the flux-tube picture of confinement.

To fully exploit the physical picture arising in $\mathbb{R} \times$ AdS we introduced a class of gauges, referred to as conformal gauges. In these gauges, there is no kinetic mixing between temporal components of the gauge field, A_τ, and spatial components, A_i. Conformal gauges are formulated in position space in d-dimensions, so that they are suitable for calculations using dimensional regularization. Conformal gauges in $\mathbb{R} \times$ AdS are effectively the analog of Feynman gauge in flat

space, and simplify some perturbative computations involving Wilson lines. Since all Wilson lines are only sources for A_τ, the absence of mixing directly implies that one only has to consider scalar exchange at leading orders in perturbation theory. In particular graphs involving three gluon or four gluon vertices may vanish simply from the absence of $(A_\tau)^3$ and $(A_\tau)^4$ interactions in QCD. We have demonstrated this explicitly by considering a two-loop computation involving three time-like Wilson lines, and showing that it reduces to a one-loop computation with counterterm insertions. For three light-like Wilson lines we have also shown that a suitable conformal gauge simplifies this calculation by making it explicit that the most complicated diagram involving the three-gluon vertex vanishes.

Many avenues remain open to future exploration, and we have only briefly touched on a few of them. In the limit where one or more Wilson lines become light-like, extra ultraviolet and infrared divergences appear, and new features emerge in the anomalous dimension of $\mathcal{W}$, such as dependence on the renormalization group scale μ. While we have formulated a suitable conformal gauge for use with light-like lines, we have not explored in detail many interesting computations, such as the two-loop anomalous dimension from two light-like lines, or graphs occurring in soft functions that have real radiation. Many interesting questions only appear for $\mathcal{W}$ with four lines taken at three loops and beyond, such as possible dependence of the anomalous dimension on conformal cross-ratios. We anticipate that the use of conformal gauges will be a powerful technique for analyses which seek to definitively answer questions which appear at this order.

We have also observed a relationship between diagrams with multiple Wilson lines and Witten diagrams, which have been studied extensively in the context of the AdS/CFT correspondence. There is hope that technology developed for computing these Witten diagrams can be used directly for calculations about Wilson lines, with direct application to jet physics, and possibly also to improved understanding of the structure of amplitudes in gauge theories.

Y: Guess what, I get a 40% improvement!

D: (give-me-five gesture)

when telescoping jets worked

4

Telescoping Jets: Multiple Event Interpretations with Multiple R's

4.1 Jet Clustering Algorithms

Jets are manifestations of the underlying colored partons in hard scattering processes. In order to reconstruct hard processes and uncover physics at high energy, jets are key objects to identify in high energy collider experiments. The conventional way to identify jets is to use clustering algorithms [164–168],

where a parameter R sets an *artificial* jet size. The constituents of each reconstructed jet are those particles within an angular scale R away from the jet direction. This is particularly true for the anti-k_T algorithm because it gives almost perfect cone jets in the calorimeter pseudorapidity-azimuthal angle (η-ϕ) plane. On the other hand, a jet is a distinct structure in its own right with many collinear particles. The width of the localized energy distribution of the jet in the

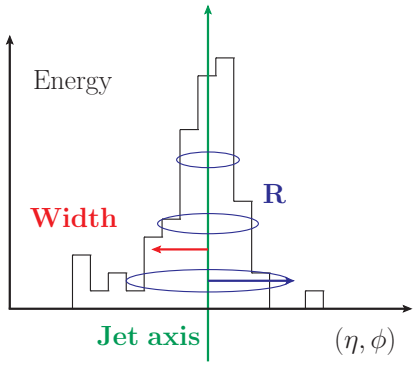

Figure 4.1: A cartoon calorimeter plot distinguishing the width of the localized energy distribution of a jet (red) from the parameter R (blue) in the anti-k_T algorithm. R is an artificial distance scale introduced to define the calorimeter region we want to look at. The jet axis points in the direction of the dominant energy flow, and the precise direction is not essential here.

η-ϕ plane is an independent quantity and should be distinguished from the parameter R (FIG. 4.1).

Because the formation of jets is quantum mechanical and probabilistic, the widths of jets are always different (FIG. 4.2). To reconstruct partonic kinematics we should pick a large enough R so that most of the radiation emitted by the partons is enclosed. However, with a large R more radiation contamination will be included. We can manage to use jet grooming techniques [39, 41, 43, 169] to get rid of contamination. Algorithms with a large R may also fail to resolve jets in some events. Multiple partons may be in a fat jet which potentially has substructure. Without looking into jet substructure we may incorrectly include irrelevant jets in event reconstruction. In the end an R is chosen for all events to optimize an analysis (see [170]

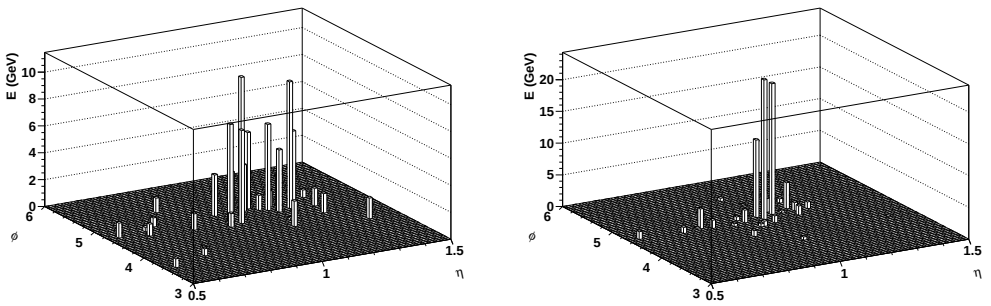

Figure 4.2: Two b jets with the same partonic kinematics but different widths, wider (top) and narrower (bottom).

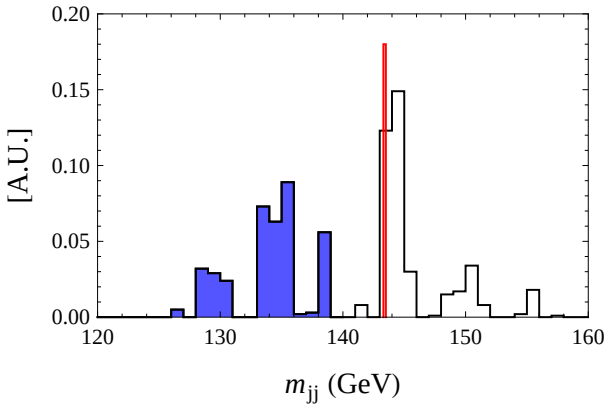

Figure 4.3: The invariant mass distribution of the two b jets for a ZH event with multiple interpretations using the telescoping jet algorithms (black). Using the anti-k_T algorithm with R=0.7, m_{jj}=143.4 GeV (red) which is outside the mass window of 110 GeV $< m_{jj} <$ 140 GeV in a conventional analysis. Using multiple interpretations reveals the ambiguity of this event and 37% of the interpretations pass the cuts (blue).

for jets with variable R). A fixed R defines a single set of constituents for each jet and a single *interpretation* for each event. There is no choice of R in conventional clustering algorithms which can resolve jets and get most of the relevant radiation for all events.

Multiple event interpretations can provide extra information and help increase the statistical power of an analysis. The recently proposed Qjet algorithms [50] give multiple event interpretations using nondeterministic jet clustering. Unlike conventional clustering algorithms, Qjets merge pairs of particles probabilistically according to an exponential weight, resulting in different clustering histories. An event may have a wide range of interpretations, and the probabilistic nature of Qjets allows the correct event structure to emerge. It was shown that jet sampling with Qjets [171] can help improve considerably in the statistical significance $S/\delta B$ –the expected size of the signal divided by the background uncertainty– in many classes of analyses, and it is interesting to understand the essence of Qjets.

4.2 Jet Algorithms with Multiple R's

In this paper we propose a simple way to define an event interpretation: each choice of R in jet algorithms gives a distinct event interpretation. The idea of probing jets with multiple R's is referred to as **telescoping jets**. As a first step we can apply conventional clustering algorithms on each event multiple times with different R's. Note that, with a too-small R we may resolve

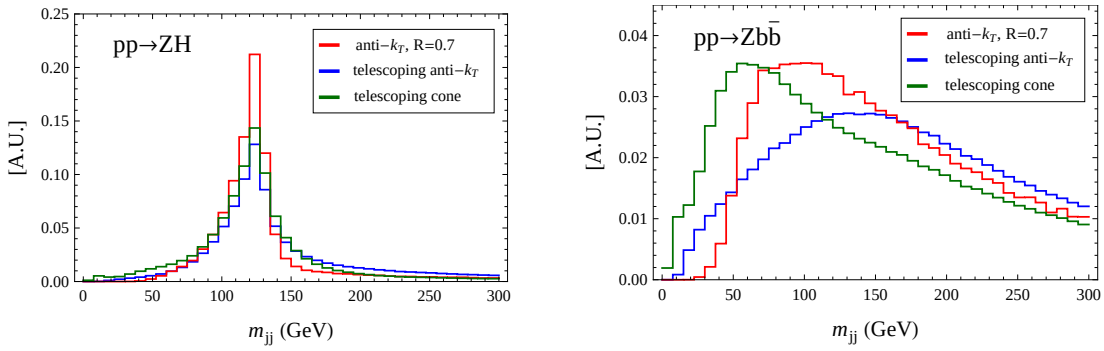

Figure 4.4: The signal (top) and background (bottom) m_{jj} distributions reconstructed using the anti-k_T algorithm with R=0.7 (red), as well as the telescoping anti-k_T (blue) and cone (green) algorithms. Using multiple event interpretations gives a wider signal Higgs mass peak, but it reduces the statistical fluctuations of the m_{jj} distributions.

an event in too much detail that miss its overall jet structure: in the $R \to 0$ limit particles are all jets. On the other hand, with a too-large R we may fail to resolve close jets. To deal with these issues, we improve the algorithm by first using the anti-k_T algorithm with a suitable R to reliably reveal the jet structure of an event and determine the jet axes from the reconstructed jet "cores". These axes point in the directions of the dominant energy flow in an event, and the precise directions are not essential. We can also use the axes determined through a jet shape minimization procedure and bypass using clustering algorithms. Then we define jet constituents by the particles within a distance R away from the predetermined jet axes in the η-ϕ plane. So different interpretations correspond to different jet constituents without the tree structure.

However, another way of thinking about the above telescoping cone algorithm is that, we essentially move *down* the clustering sequence in the anti-k_T algorithm to build up jets after identifying the branch structure. This is complimentary to moving *up* the reclustered tree and looking for mass drops to identify the branches [39,40]. Using different R's allows us to probe the energy distribution within each jet and give multiple event interpretations, and every observable of each event turns from a single number to a distribution (FIG. 4.3).

In the following we present the detailed procedure of the algorithm and apply it in a search for associated production of a Higgs and a Z where the Higgs decays to two b jets and the Z decays to $\nu\overline{\nu}$ ($ZH \to \nu\overline{\nu}b\overline{b}$). The background is Z+$b\overline{b}$ from $g \to b\overline{b}$. We require the events to pass a $\not{E}_T > 120$ GeV cut for the experimentally available triggers. The $b\overline{b}$ system is slightly boosted so that the two b jets are closer to each other and more difficult to resolve. We define the signal

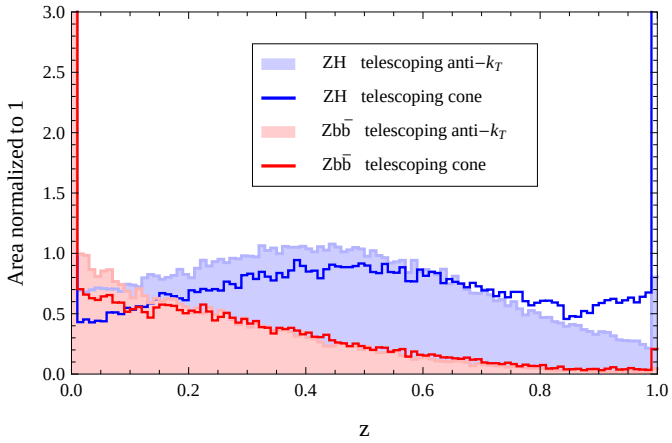

Figure 4.5: The signal and background z distributions $\rho_S(z)$ and $\rho_B(z)$ using the telescoping anti-k_T and cone algorithms. z is the fraction of interpretations of an event passing the experimental cuts. A large fraction of both signal and background events can be interpreted differently.

window (specified later) by imposing cuts on the invariant mass of the two b jets m_{jj} (FIG. 4.4) and the transverse momentum of each b-jet in our analysis. With multiple interpretations, each event is counted by the fraction of interpretations passing the cuts, instead of 0 or 1 in a conventional analysis. As we will see, this increases the statistical stability of observables so that background fluctuations shrink considerably, which is the key for $S/\delta B$ improvement.

4.3 Algorithm and Analysis

In the context of Higgs search in the $ZH \to \nu\overline{\nu}b\overline{b}$ channel, we first use the telescoping anti-k_T algorithm to reconstruct the two hardest jets with N different Rs, giving N interpretations for each event. The scaled-up computation time is tiny compared to using nondeterministic clustering algorithms [171]. Here we take N=100. The value of R ranges from 0.2 to 1.5 with an increment $\frac{1.3}{N}$. The range of R is chosen because with the $\not{E}_T > 120$ GeV cut the angular separation between the two b jets will be roughly $\lesssim 2$. Here each interpretation is weighted uniformly for simplicity.

The telescoping cone algorithm which captures the jet structure more correctly goes as follows:

- Use the anti-k_T algorithm with R=0.4 to reconstruct the cores of the two hardest jets and determine the jet axes n_1 and n_2.

- Define the i-th jet to be the particles within a distance R away from n_i in the η-ϕ plane:

$$\text{jet}_R^i = \{\ p \mid (\eta_p - \eta_{n_i})^2 + (\phi_p - \phi_{n_i})^2 < R^2\}. \tag{4.1}$$

- In the case of overlapping jets, assign particles to the jet with the closer jet axis. This step is to avoid ambiguity and is not crucial when reconstructing the invariant mass of the two hardest jets m_{jj}.

Here we use the same R for both b jets in an event. However, for generic beyond the standard model physics searches with both quark and gluon jets in the final state, one can exploit the full idea of using different R's for different jets. We will leave these for future studies.

Our signal and background events were generated at the parton level using Madgraph 5 [172] and then showered with Pythia 6.4 [22] for the 8 TeV LHC. We impose the $\not{E}_T > 120$ GeV cut at the Madgraph level and the following cuts in the analysis to define the signal window:

- 110 GeV $< m_{jj} <$ 140 GeV
- Both p_Ts of the two hardest jets > 25 GeV.

We use the anti-k_T algorithm implemented in Fastjet v3.0.0 [173, 174], and we perform the analysis with R at the optimized value of R=0.7. We then study how the statistical significance of the Higgs search changes using multiple event interpretations. With N event interpretations m_{jj} turns from a single number to a distribution for each event. We define z to be the fraction of event interpretations passing the above cuts. FIG. 4.5 shows the z distributions $\rho_S(z)$ and $\rho_B(z)$ for signal and background. This is in contrast to the conventional analysis in which an event either passes the cuts or does not. With multiple event interpretations we can gain more information about the degree of certainty of an event being signal-like. Weighting each event by z in the counting experiment helps improve the significance of the analysis.

Let ϵ and σ^2 be the mean and variance of the z distribution, and N_S and N_B be the expected numbers of signal and background events produced at the 8 TeV LHC. Then the significance is equal to

$$\frac{S}{\delta B} = \frac{N_S\ \epsilon_S}{\sqrt{N_B(\epsilon_B^2 + \sigma_B^2)}}. \tag{4.2}$$

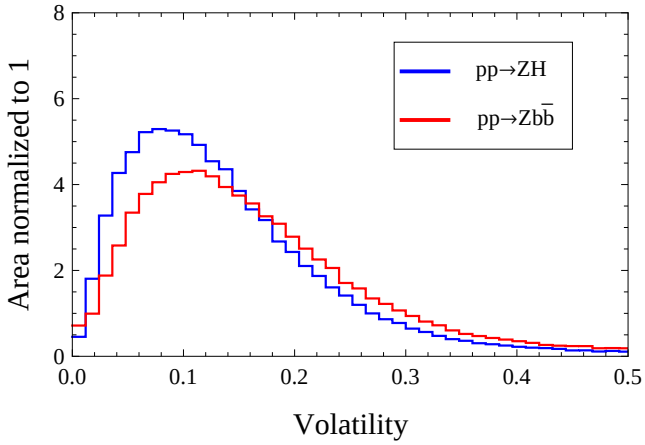

Figure 4.6: The signal (blue) and background (red) volatility distributions using the telescoping cone algorithm.

Table 4.1: $S/\delta B$ improvements using telescoping jets with different ranges of R, numbers of interpretations N, jet algorithms and weights in the counting experiment.

R range	N	algorithm	weight	$S/\delta B \uparrow$
0.4 and 1.0	2	cone	z	14%
0.4 to 1.0	7	cone	z	20%
0.4 to 1.5	12	cone	z	26%
0.2 to 1.5	100	anti-k_T	z	20%
0.2 to 1.5	100	cone	z	**28%**
0.4 to 1.5	12	cone	ρ_S/ρ_B	38%
0.2 to 1.5	100	cone	ρ_S/ρ_B	**46%**

A more detailed discussion about statistics can be found in [171, 175]. The *volatility* (FIG. 4.6) of each event is defined by $\mathcal{V}=\Gamma/\langle m\rangle$, where Γ and $\langle m\rangle$ are the standard deviation and mean of the m_{jj} distribution of each event with multiple interpretations. Volatility is useful in distinguishing boosted W jets from their QCD background [50], and we will leave exploiting volatility in Higgs searches for future studies.

4.4 Results

The performances of the algorithms are summarized in TABLE 4.1. The key for the $S/\delta B$ improvement is the shrink of background fluctuations, which comes from the rapid decrease of σ_B. For experimental studies with jet energy calibration depending on the parameter R, we try different ranges of R's and fewer interpretations using the telescoping cone algorithm. Note that

we can get half the improvement by using just two R's, and using 12 R's between 0.4 and 1.5 performs almost as good as using 100 R's between 0.2 and 1.5.

With $\rho_S(z)$ and $\rho_B(z)$ we can get an even larger improvement with the optimized weight $\frac{\rho_S(z)}{\rho_B(z)}$ [171] in the counting experiment. Then the significance is equal to

$$\frac{S}{\delta B} = \frac{N_S}{\sqrt{N_B}} \sqrt{\int_0^1 \frac{\rho_S^2(z)}{\rho_B(z)} dz} \quad , \tag{4.3}$$

and we get a 46% improvement compared to the conventional analysis. For R=0.4 to 1.5 with increment 0.1 we can get a 38% improvement with just 12 R's.

To conclude, the width of the localized energy distribution of a jet may not match well with the parameter R in jet algorithms. The situation is even more complicated for events with close jets because resolving jets becomes an issue when the parameter R and the distance between jets confront with each other. We explore a simple and promising way of giving multiple interpretations for each event by changing the parameter R in jet algorithms. The approach increases the statistical stabilities of observables which leads to remarkable improvement in the significance of a refined counting experiment. Telescoping jets open up the possibility of refining and improving jet physics analysis in high energy experiments.

Also, we only look at the transverse momenta and invariant mass of the two b jets, which are observables at high energy scales. It would be interesting to see how much more we can improve the significance of Higgs searches in hadronic channels by combining the analysis with other jet substructure [45,54,176] and color flow [46,177] observables, which probe softer sectors of QCD and color connections in an event. The approach of using multiple event interpretations could potentially be combined with likelihood ratio test and multivariate analysis, and in the presence of pile up our method will have to combine with jet grooming techniques. Applications of telescoping jets beyond physics searches, for example observable measurements, are also worth investigating. Probing jets with multiple Rs may also allow us to construct jet observables more reliably.

A

heavy jet mass

A.1 Soft function

To evaluate the heavy jet mass distribution with NNLO precision, we need the soft function at the scale μ_s evaluated to order α_s^3. The Laplace transformed soft function can be written as

$$\widetilde{s}(L_1, L_2) = \widetilde{s}_\mu(L_1, \mu)\widetilde{s}_\mu(L_2, \mu)\widetilde{s}_f(L_1 - L_2)\,, \tag{A.1}$$

where $L_1 = \ln(\mu\nu_L e^{\gamma_E})$ and $L_2 = \ln(\mu\nu_R e^{\gamma_E})$, with ν_L and ν_R the Laplace conjugate variables to the soft momenta k_L and k_R. The μ-dependence is determined by the function we call $\widetilde{s}_\mu(L, \mu)$. This is equivalent to the function $U_s(x, \mu, (ixe^{\gamma_E})^{-1})$ in [21], and we have already given its expansion to order α_s^3 in Eq. (2.14). The function $\widetilde{s}_f(L)$ is μ-independent with α_s evaluated at the scale $(\nu_L\nu_R)^{-1/2}$. It is more useful to be able to use α_s evaluated at the scale μ, which we

can do with the replacement

$$\left(\frac{\alpha_s}{4\pi}\right) \to \left(\frac{\alpha_s(\mu)}{4\pi}\right) + \left(\frac{\alpha_s(\mu)}{4\pi}\right)^2 [-\beta_0(L_1+L_2)] + \left(\frac{\alpha_s(\mu)}{4\pi}\right)^3 \left[\beta_0^2(L_1+L_2)^2 - \beta_1(L_1+L_2)\right] . \tag{A.2}$$

Then truncating the soft function to finite order will induce some residual μ-dependence.

For the finite part $\widetilde{s}_f(L)$, we use for numerical studies the form in Eq. (2.30):

$$\widetilde{s}_f(L) = 1 + \left(\frac{\alpha_s}{4\pi}\right) c_1^S + \left(\frac{\alpha_s}{4\pi}\right)^2 \left[c_2^S + c_{2L}^S L^2\right] + \cdots , \tag{A.3}$$

with

$$c_1^S = -C_F \pi^2 \tag{A.4}$$

and

$$c_2^S = \frac{\pi^4}{2} C_F^2 + (-57.8) C_F C_A + (43.4) C_F T_F n_f \tag{A.5}$$

$$c_{2L}^S = (0) C_F^2 + (-7.5) C_F C_A + (-2.1) C_F T_F n_f \tag{A.6}$$

which have been extracted using SCET from the exact NLO thrust and heavy jet mass distributions. (Note: these numbers are updated to Eq. (2.53). The main text and fits use the earlier values in Eq. (2.33).)

More generally, for NLO-matching, all that is relevant is a single projection of the order α^2 soft function

$$c_{2\rho}^S = \frac{1}{\pi} \int_0^\pi \widetilde{s}_{f2}(iL)\, \mathrm{d}L = c_2^S - \frac{\pi^2}{3} c_{2L}^S . \tag{A.7}$$

For NNLO matching, another projection is necessary, of the form in Eq. (2.27). For the form in Eq. (A.3), this projection is

$$c_{2\zeta}^S = \frac{2}{\pi} \int_0^\pi \widetilde{s}_{f2}(iL) \ln\left[2\cos(\frac{L}{2})\right] \mathrm{d}L = 4\zeta_3 c_{2L}^S . \tag{A.8}$$

These are then expanded as

$$c_2^S = C_F^2 c_{2C_F}^S + C_F C_A c_{2C_A}^S + C_F n_F T_F c_{2n_f}^S . \tag{A.9}$$

We will use these expressions for the singular heavy jet mass expansion and the G_{ij} coefficients below. We also use anomalous dimensions and β-function coefficients which can be found in [11].

A.2 Expanded soft function

Putting the pieces together, the soft function expanded to order α_s^3 with $\alpha_s = \alpha_s(\mu)$ is

$$
\begin{aligned}
\widetilde{s}(L_1, L_2, \mu) = 1 &+ \left(\frac{\alpha_s}{4\pi}\right)\Big[-({L_1}^2 + {L_2}^2)\Gamma_0 + (L_1 + L_2)\gamma_0^S + c_1^S\Big] \\
&+ \left(\frac{\alpha_s}{4\pi}\right)^2\Big[\frac{1}{2}({L_1}^4 + {L_2}^4)\Gamma_0^2 + L_1L_2(L_1\Gamma_0 - \gamma_0^S)(L_2\Gamma_0 - \gamma_0^S) + ({L_1}^3 + {L_2}^3)\left(\frac{2}{3}\beta_0\Gamma_0 - \Gamma_0\gamma_0^S\right) \\
&+ ({L_1}^2 + {L_2}^2)\left(-\Gamma_1 - \beta_0\gamma_0^S + \frac{1}{2}(\gamma_0^S)^2 - c_1^S\Gamma_0\right) + (L_1 + L_2)(\gamma_1^S - c_1^S\beta_0 + c_1^S\gamma_0^S) \\
&+ c_2^S + (L_1 - L_2)^2 c_{2L}^S\Big] \\
&+ \left(\frac{\alpha_s}{4\pi}\right)^3\Big[-\frac{1}{6}\Gamma_0^3({L_1}^6 + {L_2}^6 + 3{L_1}^2{L_2}^4 + 3{L_2}^2{L_1}^4) + \Big(-\frac{2}{3}\beta_0\Gamma_0^2 + \frac{1}{2}\gamma_0^S\Gamma_0^2\Big)({L_1}^5 + {L_2}^5) \\
&+ \frac{1}{2}\gamma_0^S\Gamma_0^2({L_1}^4L_2 + {L_2}^4L_1) + \Big(-\frac{2}{3}\beta_0\Gamma_0^2 + \gamma_0^S\Gamma_0^2\Big)({L_1}^3{L_2}^2 + {L_2}^3{L_1}^2) \\
&+ \Big(-\frac{1}{2}(\gamma_0^S)^2\Gamma_0 + \frac{5}{3}\gamma_0^S\beta_0\Gamma_0 - \frac{2}{3}\beta_0^2\Gamma_0 + \Gamma_0\Gamma_1\Big)({L_1}^4 + {L_2}^4) \\
&+ \Big(-(\gamma_0^S)^2\Gamma_0 + \frac{2}{3}\gamma_0^S\beta_0\Gamma_0\Big)({L_1}^3L_2 + {L_2}^3L_1) + \Big(-(\gamma_0^S)^2\Gamma_0 + 2\gamma_0^S\beta_0\Gamma_0 + 2\Gamma_0\Gamma_1\Big){L_1}^2{L_2}^2 \\
&+ \Big(\frac{1}{6}(\gamma_0^S)^3 - (\gamma_0^S)^2\beta_0 + \frac{4}{3}\gamma_0^S\beta_0^2 - \gamma_1^S\Gamma_0 + \frac{2}{3}\beta_1\Gamma_0 - \gamma_0^S\Gamma_1 + \frac{4}{3}\beta_0\Gamma_1\Big)({L_1}^3 + {L_2}^3) \\
&+ \Big(+\frac{1}{2}(\gamma_0^S)^3 - (\gamma_0^S)^2\beta_0 - \gamma_1^S\Gamma_0 - \gamma_0^S\Gamma_1\Big)({L_1}^2L_2 + {L_2}^2L_1) \\
&+ \Big(\gamma_0^S\gamma_1^S - 2\gamma_1^S\beta_0 - \gamma_0^S\beta_1 - \Gamma_2\Big)({L_1}^2 + {L_2}^2) + 2\gamma_0^S\gamma_1^SL_1L_2 + \gamma_2^S(L_1 + L_2) \\
&+ c_1^S\Big\{\frac{1}{2}\Gamma_0^2({L_1}^4 + 2{L_1}^2{L_2}^2 + {L_2}^4) + \Big(-\gamma_0^S\Gamma_0 + \frac{5}{3}\beta_0\Gamma_0\Big)({L_1}^3 + {L_2}^3) \\
&+ \Big(-\gamma_0^S\Gamma_0 + \beta_0\Gamma_0\Big)({L_1}^2L_2 + {L_2}^2L_1) + \Big(\frac{1}{2}(\gamma_0^S)^2 - 2\gamma_0^S\beta_0 + 2\beta_0^2 - \Gamma_1\Big)({L_1}^2 + {L_2}^2) \\
&+ \Big((\gamma_0^S)^2 - 2\gamma_0^S\beta_0\Big)L_1L_2 + \Big(-\beta_1 + \gamma_1^S\Big)(L_1 + L_2)\Big\} \\
&+ \Big(c_2^S + c_{2L}^S(L_1 - L_2)^2\Big)\Big\{(-2\beta_0 + \gamma_0^S)(L_1 + L_2) - \Gamma_0({L_1}^2 + {L_2}^2)\Big\}\Big] \,. \qquad \text{(A.10)}
\end{aligned}
$$

A.3 Singular terms in the heavy jet mass distribution

The singular part of the heavy jet mass distribution is calculable in SCET. Writing it in the form

$$D(\rho) = \delta(\rho) D_\delta + \left(\frac{\alpha_s}{2\pi}\right)[D_A(\rho)]_+ + \left(\frac{\alpha_s}{2\pi}\right)^2 [D_B(\rho)]_+ + \left(\frac{\alpha_s}{2\pi}\right)^3 [D_C(\rho)]_+ + \dots \,, \tag{A.11}$$

the result is

$$\begin{aligned} D_\delta = 1 &+ \left(\frac{\alpha_s}{4\pi}\right)\left[C_F\left(-2+\frac{2\pi^2}{3}\right)\right] \\ &+ \left(\frac{\alpha_s}{4\pi}\right)^2\left[C_F^2\left(4+\frac{\pi^4}{10}-48\zeta_3\right) + C_A C_F\left(\frac{493}{81}+\frac{85\pi^2}{6}-\frac{73\pi^4}{90}+\frac{566\zeta_3}{9}\right)\right. \\ &\left. + C_F T_F n_f\left(\frac{28}{81}-\frac{14\pi^2}{3}-\frac{88\zeta_3}{9}\right) + c^S_{2\rho}\right] , \end{aligned} \tag{A.12}$$

and

$$\begin{aligned} D_A(\rho) &= \frac{1}{\rho}\Big\{C_F\Big[-4\ln\rho-3\Big]\Big\} , \\ D_B(\rho) &= \frac{1}{\rho}\Big\{C_F^2\Big[8\ln^3\rho+18\ln^2\rho+(13-\frac{8\pi^2}{3})\ln\rho+\frac{9}{4}-\pi^2-4\zeta_3\Big] \\ &\quad + C_F T_F n_f\Big[-4\ln^2\rho+\frac{22}{9}\ln\rho+5\Big] \\ &\quad + C_F C_A\Big[11\ln^2\rho+(-\frac{169}{18}+\frac{2\pi^2}{3})\ln\rho-\frac{57}{4}+6\zeta_3\Big]\Big\} , \\ D_C(\rho) &= \frac{1}{\rho}\Big\{C_F^3\Big[-8\ln^5\rho-30\ln^4\rho+\ln^3\rho\Big(-44+8\pi^2\Big)+\ln^2\rho\Big(8\zeta_3+12\pi^2-27\Big) \\ &\quad + \ln\rho\Big(-c^S_{2\rho C_F}+48\zeta_3-\frac{41\pi^4}{90}+\frac{13\pi^2}{3}-\frac{17}{2}\Big) \\ &\quad + \frac{4\pi^2}{3}\zeta_3+14\zeta_3+12\zeta_5-\frac{3\pi^4}{40}-\frac{5\pi^2}{4}-\frac{47}{8}-\frac{3}{4}c^S_{2\rho C_F}-\frac{1}{2}c^S_{2\zeta C_F}\Big] \\ &\quad + C_F^2 n_f T_F\Big[\frac{40\ln^4\rho}{3}+\frac{56\ln^3\rho}{9}+\ln^2\rho\Big(-43-\frac{16\pi^2}{3}\Big)+\ln\rho\Big(\frac{232\zeta_3}{9}+\frac{58\pi^2}{9}-\frac{1495}{81}-c^S_{2\rho n_f}\Big) \\ &\quad + \frac{254\zeta_3}{9}-\frac{7\pi^4}{15}+\frac{71\pi^2}{18}+\frac{1511}{108}+\frac{2}{3}c^S_{2\rho C_F}-\frac{3}{4}c^S_{2\rho n_f}-\frac{1}{2}c^S_{2\zeta n_f}\Big] \\ &\quad + C_F n_f^2 T_F^2\Big[-\frac{112\ln^3\rho}{27}+\frac{68\ln^2\rho}{9}+\ln\rho\Big(\frac{140}{81}+\frac{16\pi^2}{27}\Big)-\frac{176\zeta_3}{27}-\frac{64\pi^2}{81}-\frac{3598}{243}+\frac{2}{3}c^S_{2\rho n_f}\Big] \\ &\quad + C_F C_A^2\Big[-\frac{847\ln^3\rho}{27}+\ln^2\rho\Big(\frac{3197}{36}-\frac{11\pi^2}{3}\Big)+\ln\rho\Big(22\zeta_3-\frac{11\pi^4}{45}+\frac{85\pi^2}{9}-\frac{11323}{324}\Big) \\ &\quad - 10\zeta_5+\frac{361\zeta_3}{27}+\frac{541\pi^4}{540}-\frac{739\pi^2}{81}-\frac{77099}{486}-\frac{11}{6}c^S_{2\rho C_A}\Big] \end{aligned}$$

$$
\begin{aligned}
&+ C_F^2 C_A \Big[-\frac{110\ln^4\rho}{3} + \ln^3\rho\Big(-\frac{58}{9}-\frac{8\pi^2}{3}\Big) \\
&+ \ln^2\rho\Big(-36\zeta_3+\frac{35\pi^2}{3}+\frac{467}{4}\Big) + \ln\rho\Big(-\frac{1682\zeta_3}{9}+\frac{133\pi^4}{90}-\frac{403\pi^2}{18}+\frac{29663}{324}-c^S_{2\rho C_A}\Big) \\
&- 30\zeta_5 - \frac{1943\zeta_3}{18}+\frac{2\pi^2\zeta_3}{3}+\frac{77\pi^4}{40}-\frac{757\pi^2}{72}-\frac{49}{27}-\frac{11}{6}c^S_{2\rho C_F}-\frac{3}{4}c^S_{2\rho C_A}-\frac{1}{2}c^S_{2\zeta C_A}\Big] \\
&+ C_A C_F n_f T_F \Big[\frac{616}{27}\ln^3\rho + \ln^2\rho\Big(\frac{4\pi^2}{3}-\frac{512}{9}\Big) + \ln\rho\Big(8\zeta_3-\frac{128\pi^2}{27}+\frac{673}{81}\Big) \\
&+ \frac{608\zeta_3}{27}-\frac{10\pi^4}{27}+\frac{430\pi^2}{81}+\frac{24844}{243}-\frac{11}{6}c^S_{2\rho n_f}+\frac{2}{3}c^S_{2\rho C_A}\Big]\Big\} \,. \qquad \text{(A.13)}
\end{aligned}
$$

A.4 G_{ij} expansion

Occasionally it is helpful to write an event shape distribution as

$$
R(x) = \left(1+\sum_{m=1}^{\infty} C_m \left(\frac{\alpha}{2\pi}\right)^m\right) \exp\left(\sum_{i=1}^{\infty}\sum_{j=1}^{i+1} G_{i\,j}\left(\frac{\alpha}{2\pi}\right)^i \ln^j\frac{1}{x}\right) + \sum_{n=0}^{\infty}\alpha^n f_n(x)\,. \qquad \text{(A.14)}
$$

The G_{ij} and C_m are calculable in SCET for exponentiation up to N^{3}LL accuracy.

The results are

$$
\begin{aligned}
C_1 &= C_F\Big(-\frac{5}{2}+\frac{\pi^2}{3}\Big)\,, \\
C_2 &= C_F^2\Big(\frac{41}{8}+\frac{\pi^4}{40}-\frac{\pi^2}{2}-12\zeta_3+\frac{1}{4}c^S_{2\rho C_F}\Big) + C_F n_f T_F\Big(\frac{905}{162}-\frac{58}{9}\zeta_3-\frac{7\pi^2}{6}+\frac{1}{4}c^S_{2\rho n_f}\Big) \\
&\quad + C_A C_F\Big(-\frac{8977}{648}-\frac{73\pi^4}{360}+\frac{85\pi^2}{24}+\frac{481}{18}\zeta_3+\frac{1}{4}c^S_{2\rho C_A}\Big)\,, \qquad \text{(A.15)}
\end{aligned}
$$

and

$$
\begin{aligned}
G_{12} &= -2C_F\,, \\
G_{11} &= 3C_F\,, \\
G_{23} &= C_F\Big[n_f T_F\frac{4}{3}-C_A\frac{11}{3}\Big]\,, \\
G_{22} &= C_F\Big[-C_F\frac{2\pi^2}{3}+n_f T_F\frac{11}{9}+C_A\Big(-\frac{169}{36}+\frac{\pi^2}{3}\Big)\Big]\,, \\
G_{21} &= C_F\Big[C_F\Big(4\zeta_3+\frac{3}{4}\Big)-5n_f T_F+C_A\Big(\frac{57}{4}-6\zeta_3\Big)\Big]\,, \\
G_{34} &= C_F\Big[-C_A^2\frac{847}{108}+C_A n_f T_F\frac{154}{27}-n_f^2T_F^2\frac{28}{27}\Big]\,, \\
G_{33} &= C_F\Big[C_A^2\Big(-\frac{3197}{108}+\frac{11\pi^2}{9}\Big)+n_f T_F C_A\Big(\frac{512}{27}-\frac{4\pi^2}{9}\Big)-n_f^2T_F^2\frac{68}{27}+
\end{aligned}
$$

$$
\begin{aligned}
&C_F n_f T_F\Big(2+\frac{4\pi^2}{3}\Big) - C_F C_A \frac{11\pi^2}{3} + C_F^2 \frac{16}{3}\zeta_3\Big]\,,\\
G_{32} = C_F\Big[&C_A^2\Big(11\zeta_3 - \frac{11\pi^4}{90} + \frac{85\pi^2}{18} - \frac{11323}{648}\Big) + C_A n_f T_F\Big(4\zeta_3 - \frac{64\pi^2}{27} + \frac{673}{162}\Big)\\
&+ n_f^2 T_F^2\Big(\frac{70}{81} + \frac{8\pi^2}{27}\Big) + C_F^2\Big(\frac{2\pi^4}{45} - 12\zeta_3\Big) + C_F C_A\Big(-44\zeta_3 + \frac{2\pi^4}{9} - \frac{239\pi^2}{108} + \frac{11}{8}\Big)\\
&+ C_F n_f T_F\Big(8\zeta_3 + \frac{13\pi^2}{27} + \frac{43}{6}\Big)\Big]\,,\\
G_{31} = C_F\Big[&C_F^2\Big(\frac{29}{8} + \pi^2 - \frac{8}{3}\pi^2\zeta_3 + 26\zeta_3 - 12\zeta_5 + \frac{1}{2}c^S_{2\zeta C_F}\Big)\\
&+ C_F n_f T_F\Big(-\frac{77}{4} + \frac{7\pi^4}{15} + \frac{11\pi^2}{9} - \frac{188}{9}\zeta_3 - \frac{2}{3}c^S_{2\rho C_F} + \frac{1}{2}c^S_{2\zeta n_f}\Big)\\
&+ C_F C_A\Big(\frac{23}{2} - \frac{79\pi^4}{60} - \frac{175\pi^2}{36} + \frac{4\pi^2}{3}\zeta_3 + \frac{493}{9}\zeta_3 + 30\zeta_5 + \frac{11}{6}c^S_{2\rho C_F} + \frac{1}{2}c^S_{2\zeta C_F}\Big)\\
&+ C_A^2\Big(\frac{77099}{486} - \frac{541\pi^4}{540} + \frac{739\pi^2}{81} - \frac{361}{27}\zeta_3 + 10\zeta_5 + \frac{11}{6}c^S_{2\rho C_A}\Big)\\
&+ C_A n_f T_F\Big(-\frac{24844}{243} + \frac{10\pi^4}{27} - \frac{430\pi^2}{81} - \frac{608}{27}\zeta_3 - \frac{2}{3}c^S_{2\rho C_A} + \frac{11}{6}c^S_{2\rho n_f}\Big)\\
&+ n_f^2 T_F^2\Big(\frac{3598}{243} + \frac{64\pi^2}{81} + \frac{176}{27}\zeta_3 - \frac{2}{3}c^S_{2\rho n_f}\Big)\Big]\,.
\end{aligned}
\tag{A.16}
$$

B

conformal gauge

B.1 General Class of Conformal Gauges

The most general possible form of the gauge transformation one-form is[1]

$$\Lambda_\mu(y,x) = \frac{\kappa_d}{(|x||y|)^{d/2-1}}\big[x_\mu g_1(\mathcal{A},\beta) + y_\mu g_2(\mathcal{A},\beta)\big], \qquad \text{where} \quad \mathcal{A} \equiv \frac{x\cdot y}{|x||y|},\ \beta \equiv \frac{|y|}{|x|}, \tag{B.1}$$

and $g_{1,2}(\mathcal{A},\beta)$ are functions to be specified. Eq. (3.48) yields the propagator

$$D_{\mu\nu}(x,y) = \frac{\kappa_d}{(|x||y|)^{d/2-1}}\Big[g_{\mu\nu}A + \frac{x_\mu x_\nu}{x^2}B + \frac{y_\mu y_\nu}{y^2}C + \frac{x_\mu y_\nu}{|x||y|}E + \frac{y_\mu x_\nu}{x\cdot y}Z\Big], \tag{B.2}$$

[1] More general forms are possible if we introduce one or more additional fixed vectors in the gauge transformation, such as a v^μ where $v^2 = 1$.

where we have

$$
\begin{aligned}
A &= -[2\mathcal{A} - \beta - \beta^{-1}]^{1-d/2} + g_2 + \overline{g}_2\,, \\
B &= \beta^{-1} g_1^{(1,0)} + (1-d/2)\,\overline{g}_2 - \mathcal{A}\,\overline{g}_2^{(1,0)} + \beta^{-1}\,\overline{g}_2^{(0,1)}\,, \\
C &= \beta\,\overline{g}_1^{(1,0)} + (1-d/2)\,g_2 - \mathcal{A}\,g_2^{(1,0)} + \beta\,g_2^{(0,1)}\,, \\
E &= g_1^{(0,1)} + \overline{g}_1^{(0,1)} + (1-d/2)(\beta^{-1} g_1 + \beta\,\overline{g}_1) - \mathcal{A}\big(\beta^{-1} g_1^{(1,0)} + \beta\,\overline{g}_1^{(1,0)}\big)\,, \\
Z &= \mathcal{A} g_2^{(1,0)} + \mathcal{A}\overline{g}_2^{(1,0)}\,,
\end{aligned}
\tag{B.3}
$$

with the definitions $\overline{g}_i(\mathcal{A},\beta) = g_i(\mathcal{A},\beta^{-1})$, $g_i^{(1,0)} = \partial g_i(\mathcal{A},\beta)/\partial\mathcal{A}$, $g_i^{(0,1)} = \partial g_i(\mathcal{A},\beta)/\partial\beta$, $\overline{g}_i^{(0,1)} = \partial g_i(\mathcal{A},\beta^{-1})/\partial\beta^{-1}$, etc. The conformal gauge conditions, which ensure there is no mixing between time and spatial directions in $\mathbb{R}\times\text{AdS}$, are $x^\mu D_{\mu\nu}(x,y)A^\nu(y) = 0$ when $y_\nu A^\nu(y) = 0$, and $A^\mu(x)D_{\mu\nu}(x,y)y^\nu = 0$ when $x_\mu A^\mu(x) = 0$. These require

$$
A + B + Z = 0\,, \qquad B = C\,,
\tag{B.4}
$$

which are two differential equations for the functions g_1 and g_2. Substituting Eq. (B.4) into Eq. (B.2) yields the general result for the conformal gauge propagator

$$
\begin{aligned}
\tilde{D}_{\mu\nu}(x,y) = \frac{\kappa_d}{(|x||y|)^{d/2-1}}\Bigg[&\Big(g_{\mu\nu} - \frac{x_\mu x_\nu}{x^2} - \frac{y_\mu y_\nu}{y^2} + \frac{x\cdot y\, x_\mu y_\nu}{x^2 y^2}\Big)A \\
&+ \Big(\frac{y_\mu x_\nu}{x\cdot y} - \frac{x_\mu x_\nu}{x^2} - \frac{y_\mu y_\nu}{y^2} + \frac{x\cdot y\, x_\mu y_\nu}{x^2 y^2}\Big)Z + \frac{x\cdot y\, x_\mu y_\nu}{x^2 y^2}\Big(\frac{E}{\mathcal{A}} - A - Z\Big)\Bigg]\,.
\end{aligned}
\tag{B.5}
$$

The first two tensor structures are spatial (angular), while the latter is temporal (radial). Using Eq. (B.4) and Eq. (B.3) we can write

$$
\begin{aligned}
\frac{E}{\alpha} - A - Z = &-(2\mathcal{A} - \beta - \beta^{-1})^{1-d/2} + \Big[(2-d/2)(g_2 + \overline{g}_2) + \beta\,g_2^{(0,1)} + \beta^{-1}\overline{g}_2^{(0,1)}\Big] \\
&+ \mathcal{A}^{-1}\Big[(1-d/2)(\beta^{-1} g_1 + \beta\,\overline{g}_1) + g_1^{(0,1)} + \overline{g}_1^{(0,1)}\Big]\,,
\end{aligned}
\tag{B.6}
$$

where the first term is the result from Feynman gauge and the last two terms are induced by the gauge transformation.

To consider the light-like limit for x and y we take $x^\mu = \lambda_1 n_1^\mu$ and $y^\mu = \lambda_2 n_2^\mu$, where without

loss of generality we take $\lambda_i > 0$ and send $n_1^2 = n_2^2 \to 0$. This leaves $\beta = \lambda_2/\lambda_1$ fixed and sends $\alpha \to \infty$. For the propagator between points on two light-like Wilson lines only the last term in Eq. (B.5) contributes,

$$n_1^\mu n_2^\nu \tilde{D}_{\mu\nu}(x,y) = \kappa_d \, n_1 \cdot n_2 \lim_{n_i^2 \to \infty} (\lambda_1^2 \lambda_2^2 n_1^2 n_2^2)^{1/2-d/4} \left[\frac{E}{\alpha} - A - Z \right]. \tag{B.7}$$

To ensure this gives the same result as Feynman gauge we can choose a conformal gauge where

$$g_1(\mathcal{A}, \beta) = -\mathcal{A}\beta \, g_2(\mathcal{A}, \beta) \,, \tag{B.8}$$

which makes $E/\mathcal{A} - A - Z = -(2\mathcal{A} - \beta - \beta^{-1})^{1-d/2}$. Equation (B.7) then becomes

$$n_1^\mu n_2^\nu \tilde{D}_{\mu\nu}(x,y) = -\kappa_d \, n_1 \cdot n_2 (2 n_1 \cdot n_2 \lambda_1 \lambda_2)^{1-d/2} \,, \tag{B.9}$$

which is the same as the Feynman gauge result. The $A + B + Z = 0$ and $B = C$ no mixing conditions for this case becomes

$$\beta \, g_2^{(0,1)} + (2 - d/2) g_2 = (2\mathcal{A} - \beta - \beta^{-1})^{1-d/2} \,, \tag{B.10}$$

which implies

$$g_2(\mathcal{A}, \beta) = \beta^{d/2-2} (\mathcal{A}^2 - 1)^{1-d/2} \, (\beta - \mathcal{A}) \, {}_2F_1\Big(\frac{1}{2}, \frac{d}{2} - 1, \frac{3}{2}, \frac{(\mathcal{A} - \beta)^2}{\mathcal{A}^2 - 1}\Big) + \beta^{d/2-2} h(\alpha) \,, \tag{B.11}$$

with an arbitrary function $h(\alpha)$ that still must be fixed to fully specify the gauge. Using Eq. (B.3), Eqs. (B.8) and (B.11) determine the spatial terms in the conformal gauge boson propagator in Eq. (B.5). It is straightforward to verify that the propagator is non-singular in the limit $d \to 4$.

B.2 Ghosts in Conformal Gauge

In position space the Feynman rules for ghosts are more easily represented with a "ghost field" G_μ^{abc} which is the product of a ghost propagator and ghost-gluon vertex. For the gauge trans-

formation in Eq. (3.48) the appropriate ghost field is [178]

$$G^{abc}_{\mu}(y,x) = -igf^{abc}\left[\partial^{\nu}_{y} D^{F}_{\mu\nu}(x,y) + (\partial^{x}_{\mu}\partial^{x}_{\nu} - g_{\mu\nu}\Box_{x})\Lambda^{\nu}(y,x)\right], \tag{B.12}$$

where $D^{F}_{\mu\nu}$ is the Feynman gauge gluon propagator from Eq. (3.47) and $\Lambda^{\nu}(y,x)$ is the one-form appearing in the gauge transformed gluon propagator $D_{\mu\nu}$. This result can be used for any member of the general class of conformal gauges discussed in App. B.1.

References

[1] A. Gehrmann-De Ridder, T. Gehrmann, and E.W. Nigel Glover. Antenna subtraction at NNLO. *JHEP*, 0509:056, 2005, hep-ph/0505111.

[2] A. Gehrmann-De Ridder, T. Gehrmann, E. W. N. Glover, and G. Heinrich. Second-order QCD corrections to the thrust distribution. *Phys. Rev. Lett.*, 99:132002, 2007, 0707.1285.

[3] A. Gehrmann-De Ridder, T. Gehrmann, E.W.N. Glover, and G. Heinrich. NNLO corrections to event shapes in e+ e- annihilation. *JHEP*, 0712:094, 2007, 0711.4711.

[4] Stefan Weinzierl. NNLO corrections to 3-jet observables in electron-positron annihilation. *Phys.Rev.Lett.*, 101:162001, 2008, 0807.3241.

[5] Sean Fleming, Andre H. Hoang, Sonny Mantry, and Iain W. Stewart. Jets from massive unstable particles: Top-mass determination. *Phys.Rev.*, D77:074010, 2008, hep-ph/0703207.

[6] Matthew D. Schwartz. Resummation and NLO matching of event shapes with effective field theory. *Phys.Rev.*, D77:014026, 2008, 0709.2709.

[7] Thomas Becher and Matthias Neubert. Toward a NNLO calculation of the anti-B $\to$ X(s) gamma decay rate with a cut on photon energy. II. Two-loop result for the jet function. *Phys.Lett.*, B637:251–259, 2006, hep-ph/0603140.

[8] Christian W. Bauer, Sean Fleming, Dan Pirjol, and Iain W. Stewart. An Effective field theory for collinear and soft gluons: Heavy to light decays. *Phys.Rev.*, D63:114020, 2001, hep-ph/0011336.

[9] Christian W. Bauer, Dan Pirjol, and Iain W. Stewart. Soft collinear factorization in effective field theory. *Phys.Rev.*, D65:054022, 2002, hep-ph/0109045.

[10] M. Beneke, A.P. Chapovsky, M. Diehl, and T. Feldmann. Soft collinear effective theory and heavy to light currents beyond leading power. *Nucl.Phys.*, B643:431–476, 2002, hep-ph/0206152.

[11] Thomas Becher and Matthew D. Schwartz. A Precise determination of α_s from LEP thrust data using effective field theory. *JHEP*, 0807:034, 2008, 0803.0342.

[12] R. Keith Ellis, D.A. Ross, and A.E. Terrano. The Perturbative Calculation of Jet Structure in e+ e- Annihilation. *Nucl.Phys.*, B178:421, 1981.

[13] S. Catani, L. Trentadue, G. Turnock, and B.R. Webber. Resummation of large logarithms in e+ e- event shape distributions. *Nucl.Phys.*, B407:3–42, 1993.

[14] Riccardo Abbate, Michael Fickinger, Andre Hoang, Vicent Mateu, and Iain W. Stewart. Global Fit of $alpha_s(m_Z)$ to Thrust at NNNLL Order with Power Corrections. *PoS*, RADCOR2009:040, 2010, 1004.4894.

[15] W.M. Yao et al. Review of Particle Physics. *J.Phys.*, G33:1–1232, 2006.

[16] Siegfried Bethke. The 2009 World Average of alpha(s). *Eur.Phys.J.*, C64:689–703, 2009, 0908.1135.

[17] G. Dissertori, A. Gehrmann-De Ridder, T. Gehrmann, E.W.N. Glover, G. Heinrich, et al. Determination of the strong coupling constant using matched NNLO+NLLA predictions for hadronic event shapes in e+e- annihilations. *JHEP*, 0908:036, 2009, 0906.3436.

[18] Thomas Becher and Matthew D. Schwartz. Direct photon production with effective field theory. *JHEP*, 1002:040, 2010, 0911.0681.

[19] John Ellis and Nick E. Mavromatos. On the Interpretation of Gravitational Corrections to Gauge Couplings. *Phys.Lett.*, B711:139–142, 2012, 1012.4353.

[20] Christian W. Bauer, Nicholas Daniel Dunn, and Andrew Hornig. Factorization of Boosted Multijet Processes for Threshold Resummation. *Phys.Rev.*, D82:054012, 2010, 1002.1307.

[21] Andre H. Hoang and Stefan Kluth. Hemisphere Soft Function at O(alpha(s)**2) for Dijet Production in e+ e- Annihilation. 2008, 0806.3852.

[22] Torbjorn Sjostrand, Stephen Mrenna, and Peter Z. Skands. PYTHIA 6.4 Physics and Manual. *JHEP*, 0605:026, 2006, hep-ph/0603175.

[23] A. Heister et al. Studies of QCD at e+ e- centre-of-mass energies between 91-GeV and 209-GeV. *Eur.Phys.J.*, C35:457–486, 2004.

[24] David E. Kaplan and Matthew D. Schwartz. Constraining Light Colored Particles with Event Shapes. *Phys.Rev.Lett.*, 101:022002, 2008, 0804.2477.

[25] Thomas Becher, Matthias Neubert, and Ben D. Pecjak. Factorization and Momentum-Space Resummation in Deep-Inelastic Scattering. *JHEP*, 0701:076, 2007, hep-ph/0607228.

[26] Sean Fleming, Andre H. Hoang, Sonny Mantry, and Iain W. Stewart. Top Jets in the Peak Region: Factorization Analysis with NLL Resummation. *Phys.Rev.*, D77:114003, 2008, 0711.2079.

[27] S. Catani and M.H. Seymour. The Dipole formalism for the calculation of QCD jet cross-sections at next-to-leading order. *Phys.Lett.*, B378:287–301, 1996, hep-ph/9602277.

[28] A. Gehrmann-De Ridder, T. Gehrmann, E.W.N. Glover, and G. Heinrich. Infrared structure of e+ e- $\to$ 3 jets at NNLO. *JHEP*, 0711:058, 2007, 0710.0346.

[29] M. Dasgupta and G.P. Salam. Resummation of nonglobal QCD observables. *Phys.Lett.*, B512:323–330, 2001, hep-ph/0104277.

[30] G. Dissertori, A. Gehrmann-De Ridder, T. Gehrmann, E.W.N. Glover, G. Heinrich, et al. First determination of the strong coupling constant using NNLO predictions for hadronic event shapes in e+ e- annihilations. *JHEP*, 0802:040, 2008, 0712.0327.

[31] Roger W.L. Jones, Matthew Ford, Gavin P. Salam, Hasko Stenzel, and Daniel Wicke. Theoretical uncertainties on alpha(s) from event shape variables in e+ e- annihilations. *JHEP*, 0312:007, 2003, hep-ph/0312016.

[32] Leif Lonnblad. ARIADNE version 4: A Program for simulation of QCD cascades implementing the color dipole model. *Comput.Phys.Commun.*, 71:15–31, 1992.

[33] Andre H. Hoang and Iain W. Stewart. Designing gapped soft functions for jet production. *Phys.Lett.*, B660:483–493, 2008, 0709.3519.

[34] Christian W. Bauer and Matthew D. Schwartz. Event Generation from Effective Field Theory. *Phys.Rev.*, D76:074004, 2007, hep-ph/0607296.

[35] Christian W. Bauer and Matthew D. Schwartz. Improving jet distributions with effective field theory. *Phys.Rev.Lett.*, 97:142001, 2006, hep-ph/0604065.

[36] T. Gehrmann, M. Jaquier, and G. Luisoni. Hadronization effects in event shape moments. *Eur.Phys.J.*, C67:57–72, 2010, 0911.2422.

[37] G.P. Salam and D. Wicke. Hadron masses and power corrections to event shapes. *JHEP*, 0105:061, 2001, hep-ph/0102343.

[38] J.M. Butterworth, B.E. Cox, and Jeffrey R. Forshaw. WW scattering at the CERN LHC. *Phys.Rev.*, D65:096014, 2002, hep-ph/0201098.

[39] Jonathan M. Butterworth, Adam R. Davison, Mathieu Rubin, and Gavin P. Salam. Jet substructure as a new Higgs search channel at the LHC. *Phys.Rev.Lett.*, 100:242001, 2008, 0802.2470.

[40] David E. Kaplan, Keith Rehermann, Matthew D. Schwartz, and Brock Tweedie. Top Tagging: A Method for Identifying Boosted Hadronically Decaying Top Quarks. *Phys.Rev.Lett.*, 101:142001, 2008, 0806.0848.

[41] Stephen D. Ellis, Christopher K. Vermilion, and Jonathan R. Walsh. Recombination Algorithms and Jet Substructure: Pruning as a Tool for Heavy Particle Searches. *Phys.Rev.*, D81:094023, 2010, 0912.0033.

[42] Jesse Thaler and Lian-Tao Wang. Strategies to Identify Boosted Tops. *JHEP*, 0807:092, 2008, 0806.0023.

[43] David Krohn, Jesse Thaler, and Lian-Tao Wang. Jet Trimming. *JHEP*, 1002:084, 2010, 0912.1342.

[44] Jason Gallicchio, John Huth, Michael Kagan, Matthew D. Schwartz, Kevin Black, et al. Multivariate discrimination and the Higgs + W/Z search. *JHEP*, 1104:069, 2011, 1010.3698.

[45] Jesse Thaler and Ken Van Tilburg. Identifying Boosted Objects with N-subjettiness. *JHEP*, 1103:015, 2011, 1011.2268.

[46] Jason Gallicchio and Matthew D. Schwartz. Seeing in Color: Jet Superstructure. *Phys.Rev.Lett.*, 105:022001, 2010, 1001.5027.

[47] Yanou Cui, Zhenyu Han, and Matthew D. Schwartz. W-jet Tagging: Optimizing the Identification of Boosted Hadronically-Decaying W Bosons. *Phys.Rev.*, D83:074023, 2011, 1012.2077.

[48] Jason Gallicchio and Matthew D. Schwartz. Quark and Gluon Tagging at the LHC. *Phys.Rev.Lett.*, 107:172001, 2011, 1106.3076.

[49] A. Altheimer, S. Arora, L. Asquith, G. Brooijmans, J. Butterworth, et al. Jet Substructure at the Tevatron and LHC: New results, new tools, new benchmarks. *J.Phys.G*, G39:063001, 2012, 1201.0008.

[50] Stephen D. Ellis, Andrew Hornig, Tuhin S. Roy, David Krohn, and Matthew D. Schwartz. Qjets: A Non-Deterministic Approach to Tree-Based Jet Substructure. *Phys.Rev.Lett.*, 108:182003, 2012, 1201.1914.

[51] William Man-Yin Cheung, Michael Luke, and Saba Zuberi. Phase Space and Jet Definitions in SCET. *Phys. Rev.*, D80:114021, 2009, 0910.2479.

[52] Stephen D. Ellis, Andrew Hornig, Christopher Lee, Christopher K. Vermilion, and Jonathan R. Walsh. Consistent Factorization of Jet Observables in Exclusive Multijet Cross-Sections. *Phys. Lett.*, B689:82–89, 2010, 0912.0262.

[53] Teppo T. Jouttenus. Jet Function with a Jet Algorithm in SCET. *Phys. Rev.*, D81:094017, 2010, 0912.5509.

[54] Stephen D. Ellis, Christopher K. Vermilion, Jonathan R. Walsh, Andrew Hornig, and Christopher Lee. Jet Shapes and Jet Algorithms in SCET. *JHEP*, 1011:101, 2010, 1001.0014.

[55] Andrea Banfi, Mrinal Dasgupta, Kamel Khelifa-Kerfa, and Simone Marzani. Non-global logarithms and jet algorithms in high-p_T jet shapes. *JHEP*, 08:064, 2010, 1004.3483.

[56] Yang-Ting Chien and Matthew D. Schwartz. Resummation of heavy jet mass and comparison to LEP data. *JHEP*, 08:058, 2010, 1005.1644.

[57] Randall Kelley, Matthew D. Schwartz, and Hua Xing Zhu. Resummation of jet mass with and without a jet veto. 2011, 1102.0561.

[58] Teppo T. Jouttenus, Iain W. Stewart, Frank J. Tackmann, and Wouter J. Waalewijn. The Soft Function for Exclusive N-Jet Production at Hadron Colliders. *Phys.Rev.*, D83:114030, 2011, 1102.4344.

[59] Hsiang-nan Li, Zhao Li, and C. P. Yuan. QCD resummation for jet substructures. *Phys. Rev. Lett.*, 107:152001, 2011, 1107.4535.

[60] Kamel Khelifa-Kerfa. Non-global logs and clustering impact on jet mass with a jet veto distribution. *JHEP*, 1202:072, 2012, 1111.2016.

[61] Randall Kelley, Matthew D. Schwartz, Robert M. Schabinger, and Hua Xing Zhu. Jet mass with a jet veto at two loops and the universality of non-global structure. 2011, 1112.3343.

[62] Hsiang-nan Li, Zhao Li, and C.-P. Yuan. QCD resummation for light-particle jets. 2012, 1206.1344.

[63] David Appell, George F. Sterman, and Paul B. Mackenzie. SOFT GLUONS AND THE NORMALIZATION OF THE DRELL-YAN CROSS-SECTION. *Nucl.Phys.*, B309:259, 1988.

[64] Stefano Catani, Michelangelo L. Mangano, and Paolo Nason. Sudakov resummation for prompt photon production in hadron collisions. *JHEP*, 9807:024, 1998, hep-ph/9806484.

[65] Thomas Becher, Matthias Neubert, and Gang Xu. Dynamical Threshold Enhancement and Resummation in Drell-Yan Production. *JHEP*, 0807:030, 2008, 0710.0680.

[66] Leandro G. Almeida, Seung J. Lee, Gilad Perez, Ilmo Sung, and Joseph Virzi. Top Jets at the LHC. *Phys.Rev.*, D79:074012, 2009, 0810.0934.

[67] Report. CDF-PUB-JET-PUBLIC-10119. *2011*, 2011.

[68] Mrinal Dasgupta and Gavin P. Salam. Accounting for coherence in interjet E_T flow: A case study. *JHEP*, 03:017, 2002, hep-ph/0203009.

[69] A. Banfi, G. Marchesini, and G. Smye. Away-from-jet energy flow. *JHEP*, 08:006, 2002, hep-ph/0206076.

[70] R. B. Appleby and M. H. Seymour. Non-global logarithms in inter-jet energy flow with k_T clustering requirement. *JHEP*, 12:063, 2002, hep-ph/0211426.

[71] Thomas Becher, Christian Lorentzen, and Matthew D. Schwartz. Resummation for W and Z production at large pT. *Phys.Rev.Lett.*, 108:012001, 2012, 1106.4310.

[72] Thomas Becher, Christian Lorentzen, and Matthew D. Schwartz. 2012, 1206.6115.

[73] Torbjorn Sjostrand, Stephen Mrenna, and Peter Z. Skands. A Brief Introduction to PYTHIA 8.1. *Comput.Phys.Commun.*, 178:852–867, 2008, 0710.3820.

[74] A. Banfi and M. Dasgupta. Problems in resumming interjet energy flows with k_T clustering. *Phys. Lett.*, B628:49–56, 2005, hep-ph/0508159.

[75] Yazid Delenda, Robert Appleby, Mrinal Dasgupta, and Andrea Banfi. On QCD resummation with k(t) clustering. *JHEP*, 0612:044, 2006, hep-ph/0610242.

[76] Randall Kelley, Jonathan R. Walsh, and Saba Zuberi. Abelian Non-Global Logarithms from Soft Gluon Clustering. 2012, 1202.2361.

[77] Randall Kelley, Jonathan R. Walsh, and Saba Zuberi. Disentangling Clustering Effects in Jet Algorithms. 2012, 1203.2923.

[78] Christian W. Bauer, Sean Fleming, and Michael E. Luke. Summing Sudakov logarithms in B $\to$ X(s gamma) in effective field theory. *Phys.Rev.*, D63:014006, 2000, hep-ph/0005275.

[79] Christian W. Bauer and Iain W. Stewart. Invariant operators in collinear effective theory. *Phys.Lett.*, B516:134–142, 2001, hep-ph/0107001.

[80] Randall Kelley, Matthew D. Schwartz, Robert M. Schabinger, and Hua Xing Zhu. The two-loop hemisphere soft function. *Phys. Rev.*, D84:045022, 2011, 1105.3676.

[81] Nikolaos Kidonakis, Gianluca Oderda, and George F. Sterman. Evolution of color exchange in QCD hard scattering. *Nucl.Phys.*, B531:365–402, 1998, hep-ph/9803241.

[82] Carola F. Berger, Tibor Kucs, and George F. Sterman. Event shape / energy flow correlations. *Phys.Rev.*, D68:014012, 2003, hep-ph/0303051.

[83] George F. Sterman. Partons, factorization and resummation, TASI 95. 1995, hep-ph/9606312.

[84] John C. Collins, Davison E. Soper, and George F. Sterman. Factorization of Hard Processes in QCD. *Adv.Ser.Direct.High Energy Phys.*, 5:1–91, 1988, hep-ph/0409313.

[85] Nikolaos Kidonakis, Gianluca Oderda, and George F. Sterman. Threshold resummation for dijet cross-sections. *Nucl.Phys.*, B525:299–332, 1998, hep-ph/9801268.

[86] Nikolaos Kidonakis and George F. Sterman. Resummation for QCD hard scattering. *Nucl.Phys.*, B505:321–348, 1997, hep-ph/9705234.

[87] Andrew Hornig, Christopher Lee, Iain W. Stewart, Jonathan R. Walsh, and Saba Zuberi. Non-global Structure of the $\mathcal{O}(\alpha_s^2)$ Dijet Soft Function. *JHEP*, 08:054, 2011, 1105.4628.

[88] Mrinal Dasgupta, Kamel Khelifa-Kerfa, Simone Marzani, and Michael Spannowsky. On jet mass distributions in Z+jet and dijet processes at the LHC. 2012, 1207.1640.

[89] Aneesh V. Manohar and Iain W. Stewart. The Zero-Bin and Mode Factorization in Quantum Field Theory. *Phys.Rev.*, D76:074002, 2007, hep-ph/0605001.

[90] A.D. Martin, W.J. Stirling, R.S. Thorne, and G. Watt. Parton distributions for the LHC. *Eur.Phys.J.*, C63:189–285, 2009, 0901.0002.

[91] John M. Campbell and R.K. Ellis. MCFM for the Tevatron and the LHC. *Nucl.Phys.Proc.Suppl.*, 205-206:10–15, 2010, 1007.3492.

[92] Measurement of jet mass and substructure for inclusive jets in s = 7 tev pp collisions with the atlas experiment. Technical Report ATLAS-CONF-2011-073, CERN, Geneva, May 2011.

[93] Randall Kelley and Matthew D. Schwartz. 1-loop matching and NNLL resummation for all partonic 2 to 2 processes in QCD. *Phys.Rev.*, D83:045022, 2011, 1008.2759.

[94] Christian W. Bauer, Sean Fleming, Dan Pirjol, Ira Z. Rothstein, and Iain W. Stewart. Hard scattering factorization from effective field theory. *Phys. Rev.*, D66:014017, 2002, hep-ph/0202088.

[95] Luis F. Alday and Juan Martin Maldacena. Gluon scattering amplitudes at strong coupling. *JHEP*, 0706:064, 2007, 0705.0303.

[96] G.P. Korchemsky, J.M. Drummond, and E. Sokatchev. Conformal properties of four-gluon planar amplitudes and Wilson loops. *Nucl.Phys.*, B795:385–408, 2008, 0707.0243.

[97] Andreas Brandhuber, Paul Heslop, and Gabriele Travaglini. MHV Amplitudes in N=4 Super Yang-Mills and Wilson Loops. *Nucl. Phys.*, B794:231–243, 2008, 0707.1153.

[98] J.M. Drummond, J. Henn, G.P. Korchemsky, and E. Sokatchev. On planar gluon amplitudes/Wilson loops duality. *Nucl.Phys.*, B795:52–68, 2008, 0709.2368.

[99] J.M. Drummond, J. Henn, G.P. Korchemsky, and E. Sokatchev. The hexagon Wilson loop and the BDS ansatz for the six-gluon amplitude. *Phys.Lett.*, B662:456–460, 2008, 0712.4138.

[100] Z. Bern, L.J. Dixon, D.A. Kosower, R. Roiban, M. Spradlin, et al. The Two-Loop Six-Gluon MHV Amplitude in Maximally Supersymmetric Yang-Mills Theory. *Phys.Rev.*, D78:045007, 2008, 0803.1465.

[101] J.M. Drummond, J. Henn, G.P. Korchemsky, and E. Sokatchev. Hexagon Wilson loop = six-gluon MHV amplitude. *Nucl.Phys.*, B815:142–173, 2009, 0803.1466.

[102] Nathan Berkovits and Juan Maldacena. Fermionic T-Duality, Dual Superconformal Symmetry, and the Amplitude/Wilson Loop Connection. *JHEP*, 0809:062, 2008, 0807.3196.

[103] Aneesh V. Manohar. Deep inelastic scattering as x $\to$ 1 using soft collinear effective theory. *Phys.Rev.*, D68:114019, 2003, hep-ph/0309176.

[104] Gregory P. Korchemsky, Gianluca Oderda, and George Sterman. Power corrections and nonlocal operators. 1997, hep-ph/9708346.

[105] Christian W. Bauer, Sean Fleming, Christopher Lee, and George Sterman. Factorization of e^+e^- event shape distributions with hadronic final states in Soft Collinear Effective Theory. *Phys. Rev.*, D78:034027, 2008, 0801.4569.

[106] Thomas Becher and Matthias Neubert. On the Structure of Infrared Singularities of Gauge-Theory Amplitudes. *JHEP*, 06:081, 2009, 0903.1126.

[107] Randall Kelley and Matthew D. Schwartz. Threshold Hadronic Event Shapes with Effective Field Theory. *Phys. Rev.*, D83:033001, 2011, 1008.4355.

[108] Richard A. Brandt, Filippo Neri, and Masa-aki Sato. Renormalization of Loop Functions for All Loops. *Phys.Rev.*, D24:879, 1981.

[109] Valentin Ahrens, Thomas Becher, Matthias Neubert, and Li Lin Yang. Origin of the Large Perturbative Corrections to Higgs Production at Hadron Colliders. *Phys. Rev.*, D79:033013, 2009, 0808.3008.

[110] G.P. Korchemsky and A.V. Radyushkin. Renormalization of the Wilson Loops Beyond the Leading Order. *Nucl.Phys.*, B283:342–364, 1987.

[111] Luis F. Alday and Juan Martin Maldacena. Comments on operators with large spin. *JHEP*, 11:019, 2007, 0708.0672.

[112] A. Vogt, S. Moch, and J.A.M. Vermaseren. The Three-loop splitting functions in QCD: The Singlet case. *Nucl.Phys.*, B691:129–181, 2004, hep-ph/0404111.

[113] Christian W. Bauer and Aneesh V. Manohar. Shape function effects in B $\to$ X(s) gamma and B $\to$ X(u) l anti-nu decays. *Phys.Rev.*, D70:034024, 2004, hep-ph/0312109.

[114] Jui-yu Chiu, Randall Kelley, and Aneesh V. Manohar. Electroweak Corrections using Effective Field Theory: Applications to the LHC. *Phys.Rev.*, D78:073006, 2008, 0806.1240.

[115] Jui-yu Chiu, Andreas Fuhrer, Randall Kelley, and Aneesh V. Manohar. Factorization Structure of Gauge Theory Amplitudes and Application to Hard Scattering Processes at the LHC. *Phys.Rev.*, D80:094013, 2009, 0909.0012.

[116] S.Mert Aybat, Lance J. Dixon, and George F. Sterman. The Two-loop anomalous dimension matrix for soft gluon exchange. *Phys.Rev.Lett.*, 97:072001, 2006, hep-ph/0606254.

[117] Thomas Becher and Matthias Neubert. Infrared singularities of scattering amplitudes in perturbative QCD. *Phys.Rev.Lett.*, 102:162001, 2009, 0901.0722.

[118] Einan Gardi and Lorenzo Magnea. Factorization constraints for soft anomalous dimensions in QCD scattering amplitudes. *JHEP*, 03:079, 2009, 0901.1091.

[119] Z. Bern, J.J.M. Carrasco, Lance J. Dixon, Henrik Johansson, and R. Roiban. Manifest Ultraviolet Behavior for the Three-Loop Four-Point Amplitude of N=8 Supergravity. *Phys.Rev.*, D78:105019, 2008, 0808.4112.

[120] Lance J. Dixon, Einan Gardi, and Lorenzo Magnea. All-order results for infrared and collinear singularities in massless gauge theories. *PoS*, RADCOR2009:007, 2010, 1001.4709.

[121] Vittorio Del Duca, Claude Duhr, Einan Gardi, Lorenzo Magnea, and Chris D. White. The infrared structure of gauge theory amplitudes in the high-energy limit. 2011, 1109.3581.

[122] Vittorio Del Duca, Claude Duhr, Einan Gardi, Lorenzo Magnea, and Chris D. White. An infrared approach to Reggeization. 2011, 1108.5947.

[123] Andrei V. Belitsky, A. S. Gorsky, and G. P. Korchemsky. Gauge / string duality for QCD conformal operators. *Nucl. Phys.*, B667:3–54, 2003, hep-th/0304028.

[124] V.M. Braun, G.P. Korchemsky, and Dieter Mueller. The Uses of conformal symmetry in QCD. *Prog.Part.Nucl.Phys.*, 51:311–398, 2003, hep-ph/0306057.

[125] L. N. Lipatov. High-energy asymptotics of multicolor QCD and exactly solvable lattice models. 1993, hep-th/9311037.

[126] L. D. Faddeev and G. P. Korchemsky. High-energy QCD as a completely integrable model. *Phys. Lett.*, B342:311–322, 1995, hep-th/9404173.

[127] G. P. Korchemsky. Bethe ansatz for QCD pomeron. *Nucl. Phys.*, B443:255–304, 1995, hep-ph/9501232.

[128] Aneesh V. Manohar and Mark B. Wise. Heavy quark physics. *Camb.Monogr.Part.Phys.Nucl.Phys.Cosmol.*, 10:1–191, 2000.

[129] P. Di Francesco, P. Mathieu, and D. Senechal. Conformal field theory. 1997. New York, USA: Springer (1997) 890 p.

[130] G. Parisi. Summing Large Perturbative Corrections in QCD. *Phys. Lett. B*, 90:295, 1980.

[131] George Sterman. Summation of Large Corrections to Short Distance Hadronic Cross-Sections. *Nucl. Phys. B*, 281:310, 1987.

[132] Lorenzo Magnea and George Sterman. Analytic continuation of the Sudakov form-factor in QCD. *Phys. Rev. D*, 42:4222–4227, 1990.

[133] Tim Oliver Eynck, Eric Laenen, and Lorenzo Magnea. Exponentiation of the Drell-Yan cross section near partonic threshold in the DIS and $\overline{\rm MS}$ schemes. *JHEP*, 06:057, 2003, hep-ph/0305179.

[134] D.R. Yennie, Steven C. Frautschi, and H. Suura. The infrared divergence phenomena and high-energy processes. *Annals Phys.*, 13:379–452, 1961.

[135] J. G. M. Gatheral. Exponentiation of Eikonal Cross-Sections in Non-Abelian Gauge Theories. *Phys. Lett.*, B133:90, 1983.

[136] J. Frenkel and J. C. Taylor. Non-Abelian Eikonal Exponentiation. *Nucl. Phys.*, B246:231, 1984.

[137] Einan Gardi, Eric Laenen, Gerben Stavenga, and Chris D. White. Webs in multiparton scattering using the replica trick. *JHEP*, 1011:155, 2010, 1008.0098.

[138] Alexander Mitov, George Sterman, and Ilmo Sung. Diagrammatic Exponentiation for Products of Wilson Lines. *Phys. Rev.*, D82:096010, 2010, 1008.0099.

[139] Chris D. White. Factorization Properties of Soft Graviton Amplitudes. *JHEP*, 1105:060, 2011, 1103.2981.

[140] Ratindranath Akhoury, Ryo Saotome, and George Sterman. Collinear and Soft Divergences in Perturbative Quantum Gravity. 2011, 1109.0270.

[141] Stephen G. Naculich and Howard J. Schnitzer. Eikonal methods applied to gravitational scattering amplitudes. *JHEP*, 1105:087, 2011, 1101.1524. * Temporary entry *.

[142] Raman Sundrum. Hadronic string from confinement. 1997, hep-ph/9702306.

[143] Stefan Leupold and Heribert Weigert. Radial propagators and Wilson loops. *Phys. Rev.*, D54:7695–7709, 1996, hep-th/9604015.

[144] S. Mert Aybat, Lance J. Dixon, and George F. Sterman. The two-loop soft anomalous dimension matrix and resummation at next-to-next-to leading pole. *Phys. Rev.*, D74:074004, 2006, hep-ph/0607309.

[145] Alexander Mitov, George F. Sterman, and Ilmo Sung. The Massive Soft Anomalous Dimension Matrix at Two Loops. *Phys. Rev.*, D79:094015, 2009, 0903.3241.

[146] Andrea Ferroglia, Matthias Neubert, Ben D. Pecjak, and Li Lin Yang. Two-loop divergences of massive scattering amplitudes in non-abelian gauge theories. *JHEP*, 11:062, 2009, 0908.3676.

[147] Edward Witten. Anti-de Sitter space and holography. *Adv.Theor.Math.Phys.*, 2:253–291, 1998, hep-th/9802150.

[148] Daniel Z. Freedman, Samir D. Mathur, Alec Matusis, and Leonardo Rastelli. Correlation functions in the CFT(d) / AdS(d+1) correspondence. *Nucl.Phys.*, B546:96–118, 1999, hep-th/9804058.

[149] Daniel Z. Freedman, Samir D. Mathur, Alec Matusis, and Leonardo Rastelli. Comments on 4 point functions in the CFT / AdS correspondence. *Phys.Lett.*, B452:61–68, 1999, hep-th/9808006.

[150] Eric D'Hoker and Daniel Z. Freedman. Gauge boson exchange in AdS(d+1). *Nucl.Phys.*, B544:612–632, 1999, hep-th/9809179.

[151] Eric D'Hoker, Daniel Z. Freedman, Samir D. Mathur, Alec Matusis, and Leonardo Rastelli. Graviton and gauge boson propagators in AdS(d+1). *Nucl.Phys.*, B562:330–352, 1999, hep-th/9902042.

[152] Eric D'Hoker, Daniel Z. Freedman, and Leonardo Rastelli. AdS / CFT four point functions: How to succeed at z integrals without really trying. *Nucl.Phys.*, B562:395–411, 1999, hep-th/9905049.

[153] Paul A.M. Dirac. Wave equations in conformal space. *Annals Math.*, 37:429–442, 1936.

[154] G. Mack and Abdus Salam. Finite-component field representations of the conformal group. *Annals of Physics*, 53(1):174 – 202, 1969.

[155] D.G. Boulware, L.S. Brown, and R.D. Peccei. Deep-inelastic electroproduction and conformal symmetry. *Phys.Rev.*, D2:293–298, 1970.

[156] S. Ferrara, A.F. Grillo, and R. Gatto. Tensor representations of conformal algebra and conformally covariant operator product expansion. *Annals Phys.*, 76:161–188, 1973.

[157] Steven Weinberg. Six-dimensional Methods for Four-dimensional Conformal Field Theories. *Phys.Rev.*, D82:045031, 2010, 1006.3480.

[158] Miguel S. Costa, Joao Penedones, David Poland, and Slava Rychkov. Spinning Conformal Correlators. 2011, 1107.3554.

[159] Gerhard Mack. D-independent representation of Conformal Field Theories in D dimensions via transformation to auxiliary Dual Resonance Models. Scalar amplitudes. 2009, 0907.2407.

[160] Gerhard Mack. D-dimensional Conformal Field Theories with anomalous dimensions as Dual Resonance Models. 2009, 0909.1024. dedicated to professor Ivan Todorov on the occasion of his 75th anniversary.

[161] Joao Penedones. Writing CFT correlation functions as AdS scattering amplitudes. *JHEP*, 1103:025, 2011, 1011.1485.

[162] Miguel F. Paulos. Towards Feynman rules for Mellin amplitudes in AdS/CFT. 2011, 1107.1504.

[163] A.Liam Fitzpatrick, Jared Kaplan, Joao Penedones, Suvrat Raju, and Balt C. van Rees. A Natural Language for AdS/CFT Correlators. 2011, 1107.1499.

[164] Matteo Cacciari, Gavin P. Salam, and Gregory Soyez. The Anti-k(t) jet clustering algorithm. *JHEP*, 0804:063, 2008, 0802.1189.

[165] Yuri L. Dokshitzer, G.D. Leder, S. Moretti, and B.R. Webber. Better jet clustering algorithms. *JHEP*, 9708:001, 1997, hep-ph/9707323.

[166] M. Wobisch and T. Wengler. Hadronization corrections to jet cross-sections in deep inelastic scattering. 1998, hep-ph/9907280.

[167] S. Catani, Yuri L. Dokshitzer, M.H. Seymour, and B.R. Webber. Longitudinally invariant K_t clustering algorithms for hadron hadron collisions. *Nucl.Phys.*, B406:187–224, 1993.

[168] Stephen D. Ellis and Davison E. Soper. Successive combination jet algorithm for hadron collisions. *Phys.Rev.*, D48:3160–3166, 1993, hep-ph/9305266.

[169] Stephen D. Ellis, Christopher K. Vermilion, and Jonathan R. Walsh. Techniques for improved heavy particle searches with jet substructure. *Phys.Rev.*, D80:051501, 2009, 0903.5081.

[170] David Krohn, Jesse Thaler, and Lian-Tao Wang. Jets with Variable R. *JHEP*, 0906:059, 2009, 0903.0392.

[171] Dilani Kahawala, David Krohn, and Matthew D. Schwartz. Jet Sampling: Improving Event Reconstruction through Multiple Interpretations. 2013, 1304.2394.

[172] Johan Alwall, Michel Herquet, Fabio Maltoni, Olivier Mattelaer, and Tim Stelzer. MadGraph 5 : Going Beyond. *JHEP*, 1106:128, 2011, 1106.0522.

[173] Matteo Cacciari, Gavin P. Salam, and Gregory Soyez. FastJet User Manual. *Eur.Phys.J.*, C72:1896, 2012, 1111.6097.

[174] Matteo Cacciari, Gavin P. Salam, and Gregory Soyez. http://fastjet.fr/.

[175] Stephen D. Ellis, Andrew Hornig, Tuhin S. Roy, David Krohn, and Matthew D. Schwartz. In preparation.

[176] Iain W. Stewart, Frank J. Tackmann, and Wouter J. Waalewijn. N-Jettiness: An Inclusive Event Shape to Veto Jets. *Phys.Rev.Lett.*, 105:092002, 2010, 1004.2489.

[177] Anson Hook, Martin Jankowiak, and Jay G. Wacker. Jet Dipolarity: Top Tagging with Color Flow. *JHEP*, 1204:007, 2012, 1102.1012.

[178] Hung Cheng and Er-Cheng Tsai. Gauge Invariance of the Quantum Wilson Loop. *Phys.Rev.*, D36:3196, 1987.